Summer 2011

Theoretical studies on the structure and dynamics of room-temperature ionic liquids

Harsha Vardhan Reddy Annapureddy
University of Iowa

THEORETICAL STUDIES ON THE STRUCTURE AND DYNAMICS OF ROOM-TEMPERATURE IONIC LIQUIDS

by

Harsha Vardhan Reddy Annapureddy

An Abstract

Of a thesis submitted in partial fulfillment of the
requirements for the Doctor of Philosophy
degree in Chemistry
in the Graduate College of
The University of Iowa

July 2011

Thesis Supervisor: Associate Professor Claudio J. Margulis

ABSTRACT

In this thesis, we present our studies on the structure and dynamics of novel Room-Temperature Ionic Liquids. Through our computer simulations we demonstrate that the kinetics of photo induced electron transfer reaction between S_1 and S_2 states of Crystal Violet Lactone in N-propyl-N-methylpyrrolidiniumbis(trifluoromethylsulfonyl)imide($[Pr_{31}^{+}][NTf_2{}^{-}]$) room temperature ionic liquid is local solvent environment dependent, because emission time scales are smaller than solvent relaxation time scales. This behavior is characteristic of ionic liquids but uncommon in conventional solvents. Therefore ionic liquids open a window of opportunity for manipulating the outcome of chemical reactions simply by tuning the initial excitation wavelength.

We performed Molecular dynamics simulations of mixtures of 1-hexyl-3-methyl imidazoliumhexafluorophosphate ($[C_6MIM^{+}][PF_6^{-}]$) and water in order to investigate how small amounts of water affect the translational and rotational dynamics of ionic liquids. We find that water is closely associated with the anions and that its presence enhances both the translational and rotational dynamics of the ionic liquid. In agreement with experiments, we find that the fluorescence spectra of Coumarin-153 is red-shifted because of the presence of water. Small amounts of water enhance the speed of relaxation of the solvent surrounding the solute probe after photo-excitation, but only at a local environment level. Interconversion between environments still occurs on a long time scale compared with the fluorescence lifetime of the probe.

To interpret the features of x-ray scattering structure factor of room temper-

ature ionic liquids we introduce a set of general theoretical partitions of real and reciprocal space correlations that allow for unambiguous analysis of all intra- and inter-ionic contributions to the structure function and coherent scattering intensity. Through our simulations we could explain the origin of various peaks in the x-ray structure function of methyltributylammonium bis(trifluoromethylsulfonyl)amide.

In order understand the origin of the first sharp diffraction peak in the x ray structure factor of Imidazolium based ionic liquids, we use several different computational techniques to thoroughly dissect the atomistic components giving rise to the low frequency first sharp diffraction peak as well as other features in the structure function (S(q)). By understanding how S(q) changes as Imidazolium based ionic systems undergo solid-liquid phase transition, and by artificially perturbing the liquid structure in a way that directly couples to the intensity of the first sharp diffraction peak, we are able to identify in a rigorous way its geometric origin.

Abstract Approved: _____
Thesis Supervisor

_____
Title and Department

_____
Date

THEORETICAL STUDIES ON THE STRUCTURE AND DYNAMICS OF ROOM-TEMPERATURE IONIC LIQUIDS

by

Harsha Vardhan Reddy Annapureddy

A thesis submitted in partial fulfillment of the
requirements for the Doctor of Philosophy
degree in Chemistry
in the Graduate College of
The University of Iowa

July 2011

Thesis Supervisor: Associate Professor Claudio J. Margulis

Graduate College
The University of Iowa
Iowa City, Iowa

CERTIFICATE OF APPROVAL

PH.D. THESIS

This is to certify that the Ph.D. thesis of

Harsha Vardhan Reddy Annapureddy

has been approved by the Examining Committee for the thesis requirement for the Doctor of Philosophy degree in Chemistry at the July 2011 graduation.

Thesis Committee: _____
Claudio Margulis, Thesis Supervisor

_____
Christopher M. Cheatum

_____
Amnon Kohen

_____
Christopher Pigge

_____
Adrian Elcock

To my beloved family

ACKNOWLEDGMENTS

I consider this to be an important section of my dissertation. I attempt sincerely to express my gratitude to all those who have contributed professionally and personally to make my grad school experience wonderful.

First and foremost, I would like to express my sincere thanks to my advisor Prof. Claudio J. Margulis for his continuous support and encouragement during the course of doctoral degree. I appreciate his faith in me. He taught me how to appreciate science, perform research, communicate ideas, and have a vision. He was always welcome for scientific discussions and listening to my difficulties however trivial they were. The strong scientific foundation that he gave me will continue to inspire and guide me in my career. This dissertation would not have been possible without his mentoring and support.

I would like to express gratitude to all the members of my thesis committee. I appreciate their effort in reading my thesis and their insightful suggestions. I thank Dr. Dale Swenson for insightful discussions on crystallography. I should also thank department of chemistry IT staff David Sansbury, Jeffrey Miller and Chris Lawrence for their excellent computer technical support. I would also like to thank our collaborators at Rutgers Prof. Edward Castner and Dr. Cherry Santos.

I would like to thank all the past and present group members of Prof. Margulis lab for accommodating me and creating an excellent ambience for research and learning. Dr. Zhonghan Hu was a senior graduate student in the lab, when I joined.

He was very helpful and taught me many things during the first two formative years. Dr. Hemant Kashyap joined the lab as post doc during 2009. His presence during the past two years was very helpful for me in completing this dissertation. I thank Dr. Ying-hua Chung and Saikumar Ramadugu for their wonderful support and friendship during the past five years.

Special thanks to my friend Dr. Gopeekrishnan Sreenilayam for being a great roommate for five years. He was always there for me during the tough times. I am fortunate to have his friendship. I would also like to thank my friends Dr. Jigar Bandaria, Dr. Adil Mohammed and Dr. Ramsubramanian Kanthaswamy, Dr. Samrat Dutta. I greatly appreciate their help during my first year in Iowa city.

Life in Iowa city would not have been so joyful with out the friends like Ashish, Pradeep, Janardhan, Vasu, Praveen, Shyam, Ajit, Naveen, Sudharshan, Boddu, Deva, Gavurav, Sahaj, Prashant. I take this opportunity to thank all of them for making this journey very pleasant and enjoyable.

Of course, none of this would have been possible, or unimaginable without support from my parents, brother and sister. I am greatly indebted to all my family members. Their unconditional love, support and continuous encouragement gave me enough strength to overcome every obstacle that I came across during the course of this doctoral degree.

ABSTRACT

In this thesis, we present our studies on the structure and dynamics of novel Room-Temperature Ionic Liquids. Through our computer simulations we demonstrate that the kinetics of photo induced electron transfer reaction between S_1 and S_2 states of Crystal Violet Lactone in N-propyl-N-methylpyrrolidiniumbis(trifluoromethylsulfonyl)imide($[Pr^+_{31}][NTf_2{}^-]$) room temperature ionic liquid is local solvent environment dependent, because emission time scales are smaller than solvent relaxation time scales. This behavior is characteristic of ionic liquids but uncommon in conventional solvents. Therefore ionic liquids open a window of opportunity for manipulating the outcome of chemical reactions simply by tuning the initial excitation wavelength.

We performed Molecular dynamics simulations of mixtures of 1-hexyl-3-methyl imidazoliumhexafluorophosphate ($[C_6MIM^+][PF^-_6]$) and water in order to investigate how small amounts of water affect the translational and rotational dynamics of ionic liquids. We find that water is closely associated with the anions and that its presence enhances both the translational and rotational dynamics of the ionic liquid. In agreement with experiments, we find that the fluorescence spectra of Coumarin-153 is red-shifted because of the presence of water. Small amounts of water enhance the speed of relaxation of the solvent surrounding the solute probe after photo-excitation, but only at a local environment level. Interconversion between environments still occurs on a long time scale compared with the fluorescence lifetime of the probe.

To interpret the features of x-ray scattering structure factor of room temper-

ature ionic liquids we introduce a set of general theoretical partitions of real and reciprocal space correlations that allow for unambiguous analysis of all intra- and inter-ionic contributions to the structure function and coherent scattering intensity. Through our simulations we could explain the origin of various peaks in the x-ray structure function of methyltributylammonium bis(trifluoromethylsulfonyl)amide.

In order understand the origin of the first sharp diffraction peak in the x ray structure factor of Imidazolium based ionic liquids, we use several different computational techniques to thoroughly dissect the atomistic components giving rise to the low frequency first sharp diffraction peak as well as other features in the structure function (S(q)). By understanding how S(q) changes as Imidazolium based ionic systems undergo solid-liquid phase transition, and by artificially perturbing the liquid structure in a way that directly couples to the intensity of the first sharp diffraction peak, we are able to identify in a rigorous way its geometric origin.

TABLE OF CONTENTS

LIST OF TABLES

Table

LIST OF FIGURES

Figure

CHAPTER 1
INTRODUCTION

Room temperature Ionic liquids(RTILs) are salts that melt below 100°C, and often below room temperature. Ionic liquids have been known for about a century, with one of the earliest examples published being ethylammonium nitrate[135]. However since the past two decades research on RTILs is expanding rapidly[143, 142]. In recent few years ionic liquids have shifted from just being laboratory curiosity to important components to advanced processes and devices with various applications. Many ionic liquids have desirable properties for such uses, including low volatility, thermal stability up to high temperatures, good electrical and thermal conductivity, wide electrochemical windows, and the ability to solubilize a variety of materials including organic and inorganic compounds, polymers and biopolymers. As opposed to most other organic solvents, these liquids have the potential of being greener reaction media because they are non-volatile.

RTILs synthesized using various combinations of ions (see for example Fig. 1.1 and Fig. 1.2) are widely different in their thermodynamic, kinetic, chemical and solvation properties. Also by modifying the length, branching or the number of substituents in the cation, it is possible to generate an exponentially large number of RTILs. Because of this reason RTILs are often referred to as *tailor-made designer solvents*[2, 20, 85] . One has almost infinite flexibility in choosing cations and anions, but little is known about what the exact properties of the new compounds will turn out to be once they are made. Why is it that two very similar ionic liquids have

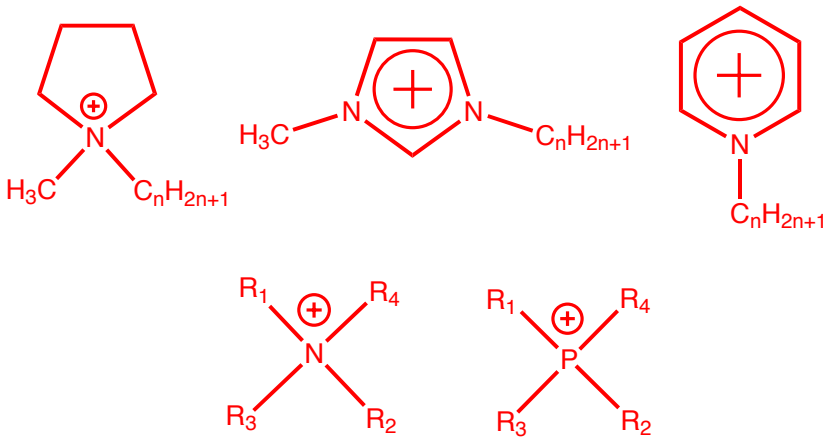

Figure 1.1: Common cations of RTILs

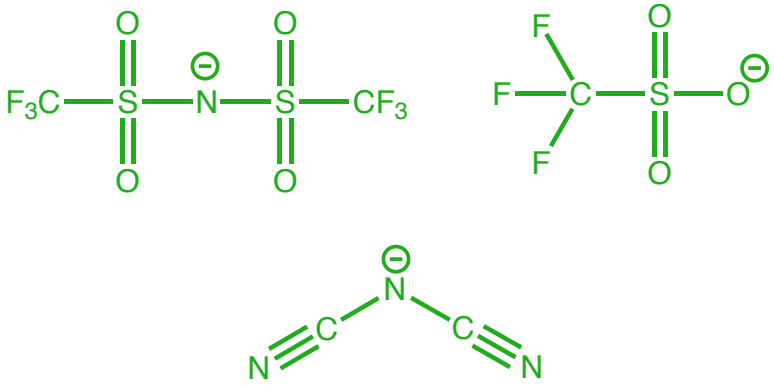

Cl^-, Br^-, I^-, NO_3^-, BF_4^-, PF_6^-, $CH_3CO_2^-$

Figure 1.2: Common anions of RTILs

significantly different physical properties? What are the chemical parameters that need to be adjusted to obtain the desired outcome in a chemical reaction? These are the questions that need to be addressed to harness the complete potential of RTILs. In order to answer these questions one must require a deep and expert level insight of the microscopic properties to be expected for existent and nonexistent RTILs and how these are linked to actual chemical reactivity. Using theory and computer simulations our research group is working towards gaining that expert level of understanding of RTILs at a molecular level.

The reason why RTILs are liquid at room temperature is still not fully understood. From the X-ray crystal structure studies, we know that some tend to crystallize into disordered solids[85] and, depending upon the rate of cooling, crystal polymorphism[58] can be observed. On the basis of these observations, it has been speculated that the gain in energy upon formation of the crystal is not as large as in traditional inorganic salts and is not enough to compensate for the loss in entropy that accompanies the formation of the crystal at room temperature[85]. Experiments show that several of these systems have a tendency toward glassy behavior[106, 141] and, depending upon the length of alkyl substituents in the cations, their properties range from those of normal liquids to glassy or even liquid crystals[59].

Previous work in our research group demonstrated that diffusive dynamics of these systems is slow and heterogenous. As a consequence, upon photoexcitation of an organic probe with an emission lifetime (on the order of several pico seconds) significantly shorter than the solvent reorganization timescales of RTILs(on the order

of several nanoseconds), the resulting emission spectrum is absorption wavelength dependent. Based on these results we predicted that if one performs a reaction which is faster than the solvent relaxation time scale of RTILs, then the outcome of such a chemical reaction should be local solvent environment dependent. In order to prove this hypothesis we performed simulations studies on the photo induced intramolecular electron transfer reaction of CVL in $[Pr_{31}^{+}][NTf_2^{-}]$RTIL. The results of our simulation studies that are presented in chapter 3 indicate that the electron transfer reaction kinetics is indeed local solvent environment dependent. Our simulation results are strongly supported by experiments and it appears that this phenomenon has now been observed to be relevant not only in fluorescence experiments but also in electron transfer reactions, proton transfer reactions and isomerization reactions [83, 113, 79, 80].

Water is a major unavoidable impurity in ionic liquids. Ionic liquids with anions such as halides, nitrate, methyl sulfonate or formate are hydrophilic, whereas anions such as hexafluorophosphate and bis(trifluoromethylsulfonyl)imide are more hydrophobic. The cation also contributes to the water solubility in RTILs: the elongation of the cation alkyl chain reduces water solubility, and also the introduction of some various functional groups such as hydroxyl, ethers, amines increases the solubility. However, independent of their miscibility with water, all ILs are hygroscopic to a certain extent and can absorb significant amounts of water from the atmosphere. Since contact with water is hard to avoid, it is the most common impurity in RTILs, which is able to affect significantly important physico-chemical properties such as

polarity, viscosity, conductivity. Water can also act as a co-solvent, to tune the solubility of various gases, polar and non polar compounds [118, 107, 37, 64]. There is high variability in the viscosity measurements obtained by different authors and water contamination could be one possible explanation for this high variability. Water absorption can also influence the chemical reactions and processes occurring in ILs. Such an impurity is difficult to remove from ionic liquids because of their high hygroscopic nature. This was motivation to our simulations studies on IL+water mixtures. We intended to understand how water affect the dynamics of ionic liquids. Through our simulations that are presented in chapter 4 we found that water screens the direct Coulombic interactions between cations and anions and hence enhances the rotational and translational diffusion. We also studied how water would affect the fluorescence spectra of coumarin in ionic liquid.

RTILs are made of cations which have both highly polar and non-polar components. This kind of amphiphilic nature of ions can give rise to structural organization on a few nanometer length scale. We were interested in understanding how the structure influences the dynamics and chemical reactivity in ionic liquids. The first step towards this investigation is to find what kind of structural correlations are possible in various ionic liquids.

In his thesis we present our structural studies on two different classes of ionic liquids. In chapter 5 we present the temperature dependent structure of methyltributylammonium bis(trifluoromethylsulfonyl)amide($N_{1444}{}^{+}/NTf_2{}^{-}$). This research work is a collaborative effort with Prof. Edward Castner's group at Rutgers. They

performed the SAXS and WAXS experimental studies and MD simulation studies are performed in our lab. In this chapter we also present a general theoretical partitioning scheme to understand the intra and interionic contributions to the x-ray structure function.

In chapter 6 we present our computational studies on the structure of imidazolium based ionic liquids. The observation of a first sharp diffraction peak (FSDP) or pre-peak at low frequency in the X-ray and neutron scattering spectra of different imidazolium based room-temperature ionic liquids has often been interpreted by experimentalists as indicative of mesoscopic organization leading to nanoscale segregation and the formation of domains of different morphologies. We used several different computational techniques to thoroughly dissect the atomistic components giving rise to the low-frequency FSDP as well as other features in the structure function (S(q)). By understanding how S(q) changes as imidazolium-based ionic systems undergo solid liquid phase transition, and by artificially perturbing the liquid structure in a way that directly couples to the intensity of the FSDP, we are able to identify in a rigorous way its geometric origin.

CHAPTER 2
MOLECULAR DYNAMICS SIMULATIONS

Theoretical studies on the structure and dynamics of ionic liquids that we present in this thesis are performed using Molecular Dynamics (MD) simulations. This chapter will provide a brief introduction to molecular dynamics simulations and the potential energy function that we used to study the RTIL systems. More elaborate explanation on the theory of molecular dynamics simulations are available in the literature[1, 35, 134].

Molecular dynamics has extensively enriched the understanding of the behavior of liquids since the middle of last century[1]. In simple terms, the procedure of classical simulation involves solving Newton's equations numerically. For our NVE production runs, Newton's equations of motion are:

$$\dot{\mathbf{R}}_j = \mathbf{v}_j$$

$$m_j \dot{\mathbf{v}}_j = \mathbf{a}_j$$

One of the most popular algorithm to numerically solve these Newtonian equations of motion is the Verlet algorithm.

Verlet Algorithm At time t, the system has a configuration $(\mathbf{R}^N(t), \mathbf{v}^N(t))$, the force is determined by the derivative of the potential:

$$\mathbf{a}_j(t) = -\frac{1}{m_j}\nabla_j(U\mathbf{R}^N(t)) \tag{2.1}$$

Taylor expansions at $t = t + \Delta t$ and $t = t - \Delta t$ gives the coordinates of next frame

and previous frame respectively:

$$\mathbf{R}_j(t+\Delta t) = \mathbf{R}_j(t) + \mathbf{v}_j(t)\Delta t + \frac{1}{2}\mathbf{a}_j(t)\Delta t^2 + \frac{1}{6}\mathbf{b}(t)\Delta t^3 + \mathcal{O}(\Delta t^4)$$

$$\mathbf{R}_j(t-\Delta t) = \mathbf{R}_j(t) - \mathbf{v}_j(t)\Delta t + \frac{1}{2}\mathbf{a}_j(t)\Delta t^2 - \frac{1}{6}\mathbf{b}(t)\Delta t^3 + \mathcal{O}(\Delta t^4)$$

The Verlet algorithm calculates the configuration at the next frame $t = t+\Delta t$ through:

$$\mathbf{R}_j(t+\Delta t) = 2\mathbf{R}_j(t) - \mathbf{R}_j(t-\Delta t) + \mathbf{a}_j(t)\Delta t^2 + \mathcal{O}(\Delta t^4)$$

$$\mathbf{v}_j(t) = \frac{\mathbf{R}_j(t+\Delta t) - \mathbf{R}_j(t-\Delta t)}{2\Delta t} + \mathcal{O}(\Delta t^2)$$

Modifications to the above basic scheme have been proposed during the last thirty years[57, 102, 134]. The integration algorithm used in our simulations is the leap-frog scheme implemented in Gromacs software[86, 10, 134].

$$\mathbf{R}_j(t+\Delta t) = \mathbf{R}_j(t) + \Delta t\mathbf{v}(t+\frac{1}{2}\Delta t)$$

$$\mathbf{v}(t+\frac{1}{2}\Delta t) = \mathbf{v}(t-\frac{1}{2}\Delta t) + \Delta t\mathbf{a}(t)$$

Periodic Boundary Condition (PBC) In order to minimize the edge effects involved in a finite system, we employ periodic boundary conditions. This simply means surrounding the simulation box with replicas of itself. We can adopt the minimum image convention that each atom interacts with the nearest atom or image in the periodic array. During the course of the simulation, if an atom leaves the basic simulation box, attention can be switched to the incoming image. In order to properly account for the long range electrostatic interactions we use Particle Mesh Ewald(PME) algorithm.

Calculating the force The most time-consuming part of molecular dynamics simulation is calculation of force through Eq. (2.1) In our simulations of ionic liquids, we use a potential energy function of the form[96]

$$U = U_{stretch} + U_{bend} + U_{torsion} + U_{LJ} + U_{Coulomb} \tag{2.2}$$

$U_{stretch}$ is given by (Eq. 2.3) a harmonic potential representing the interaction between two atoms that are separated by one covalent bond. This is an approximation to the energy of a bond as a function of displacement from the equilibrium bond length, r_{eq}. The force constant, K_r, determines the strength of the bond. r_{eq} and K_r are specific for each pair of bound atoms.

$$U_{stretch} = \sum_{bonds} K_r(r - r_{eq})^2 \tag{2.3}$$

U_{bend} given by 2.4, is also a harmonic potential which is associated with alteration of bond angles θ from the equilibrium value θ_{eq}

$$U_{bend} = \sum_{angles} K_\theta(\theta - \theta_{eq})^2 \tag{2.4}$$

$U_{torsion}$ represents the torsional angle potential function given by Eq. 2.5 which models the presence of steric barriers between atoms separated by 3 covalent bonds.

$$U_{torsion} = \sum_{dihedrals} \sum_{n=0}^{5} C_n(\cos(\phi))^n) \tag{2.5}$$

U_{LJ} represents the van der Waals interactions given by Eq. 2.6 and $U_{Coulomb}$ represents the electrostatic Coulomb potential given by Eq. 2.7.

$$U_{LJ} = \sum_{i<j} 4\epsilon_{ij} \left[(\frac{\sigma_{ij}}{r_{ij}})^{12} - (\frac{\sigma_{ij}}{r_{ij}})^{6} \right] \tag{2.6}$$

$$U_{Coulomb} = \sum_{i<j} \frac{q_i q_j}{r_{ij}} \tag{2.7}$$

More specific details of various MD simulations are reported in the individual chapters.

CHAPTER 3
ELECTRON TRANSFER REACTIONS IN IONIC LIQUIDS

3.1 Introduction

In this chapter using computer simulations we demonstrate how one can take advantage of the slow and heterogeneous dynamics of room temperature ionic liquids to control the outcome of chemical reaction. Previous work in our research group established that due to the slow nature of ionic liquids distributed dynamics is possible[60, 62]. Hence solute molecules in ionic liquids are distributed in different solvent environments that can be experimentally identified and selected. The ability for spatial selection is not unique to ionic liquids; for example one can do a hole burning experiment in any liquid. Instead, it is the time scale during which these environments remain almost unchanged that is useful and unique to ionic liquids. Our main assertion is that in ionic liquids, selection of solvent environments is equivalent to chemical reactivity control. This option for control is absent in normal liquids where the solvent response is faster when compared to the time scale for transition state formation in ground state reactions or excited state lifetimes in excited state chemistry.

As has been previously shown[90, 89, 91, 123, 121, 120], Marcus theory can be applied in ionic liquids. In a set of very interesting articles Lynden-Bell and coworkers[90, 89, 91, 123] as well as Kim and coworkers[121, 120] have demonstrated that reaction free energies for electron transfer processes in ionic liquids are Marcus-

like and that their functional form is quadratic. As we will show in subsequent sections of this chapter that we also find this to be true. Local environments may favor different products both because barriers to interconversion (and therefore rate constants) are locally different and also because free energy differences (and therefore thermodynamic constants) are also locally different. This leads to ranges of local free energy differences and local rate constants.

Samanta and co-workers[93, 94, 100, 112] found that under certain circumstances, the fluorescence response of probes in room temperature ionic liquids can be dependent on the excitation wavelength, a phenomenon known as red-edge effect (REE). This phenomenon is observable only when excited state lifetimes are short when compared with solvent relaxation time scales. Previous work from our group[61, 60] has attempted to explain in atomistic detail how this phenomenon occurs in room temperature ionic liquids. This chapter attempts to extend our understanding of distributed dynamics in ionic liquids beyond fluorescence and into the realm of chemical reactivity. It turns out that since we first published our work on absorption wavelength dependent electron transfer[4], this phenomenon has been demonstrated to be important in many different experiments in ionic liquids[83, 113, 79, 80, 111, 21].

As an example of the way in which distributed dynamics manifests itself in chemical reactivity, in this chapter we explore the excitation wavelength dependence of electron transfer between two polar excited states of crystal violet lactone(CVL) in N-propyl-N-methylpyrrolidinium bis(trifluromethylsulfonyl)imide ionic liquid $[Pr^{+}_{31}][NTf_2{}^{-}]$(see Figures 3.1 and 3.2). Initial results from the Maroncelli

group[70] indicated that the effect of distributed dynamics in this particular system were large, but later results[71] have claimed that this is less so.

CVL is a dual fluorescent molecule. Extensive studies by Karpiuk [75] had previously shown that the photoexcitation of CVL into the S_1 state with dipole moment of 11D is localized on the aminophthalide ring. Subsequent electron transfer from one of the dimethylaniline groups to the aminophthalide group results in the formation of the more polar S_2 state with a dipole moment of 25D. The emission spectra of CVL in different polar solvents show two peaks corresponding to electronic decay from S_1 and S_2 respectively. Maroncelli and coworkers found that upon photo excitation of CVL in $[Pr^+_{31}][NTf_2{}^-]$ at different wavelengths the emission intensities of these two peaks varied significantly. This dependence of the electron transfer product distribution on the excitation wavelength is absent in normal solvents.

3.2 Simulations and methods

We performed molecular dynamics simulation for the CVL in $[Pr^+_{31}][NTf_2{}^-]$ system. For comparison, we also performed molecular dynamics simulations of CVL in acetonitrile. All simulations were carried out using the AMBER 9 package[19].

All trajectories in the room temperature ionic liquid consisted of a single flexible CVL molecule solvated by 150 $[Pr^+_{31}][NTf_2{}^-]$ion pairs. Simulations in acetonitrile consisted of a single CVL molecule solvated by 424 acetonitrile molecules.

All systems were thoroughly equilibrated for several nanoseconds. For the case Ionic Liquids it is very difficult to obtain truly equilibrated initial conditions. In order

to make sure the systems were correctly equilibrated, we lowered and raised the total charge of the ions and we also performed runs at high temperature and later slowly annealed the system to match experimental conditions. These equilibration runs were performed in the NPT (constant number of particles, pressure, and temperature) ensemble using the Berendsen algorithm[9]. Final simulation box sizes were 40.5Å in the case of the room temperature ionic liquid and 34.3Å in the case of acetonitrile.

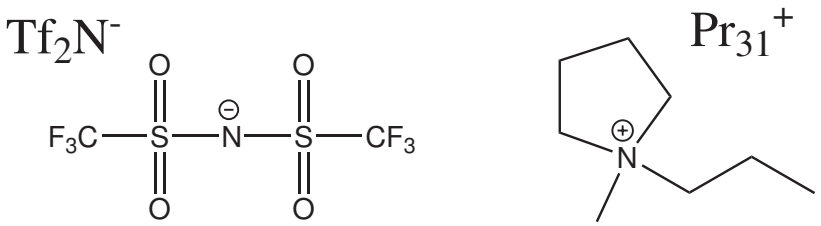

Note: *N*-propyl-*N*-methylpyrrolidinium bis(trifluromethylsulfonyl)imide ionic liquid.

Figure 3.1: Structure of $[Pr_{31}^{+}][NTf_2^{-}]$

Once systems were properly equilibrated at 300K, NVE (constant number of particles, volume and energy) production runs were launched. In order to compute emission spectra we first run an ensemble of equilibrated trajectories in the ground electronic state for one nanosecond and then simulate instantaneous vertical excitation by changing potential parameters to those of states S_1 and S_2. In the case of the free energy calculations we wait for 700 ps after photo-excitation for short time scale transients to disappear and then collect data from each trajectory for a period of 1.3 ns.

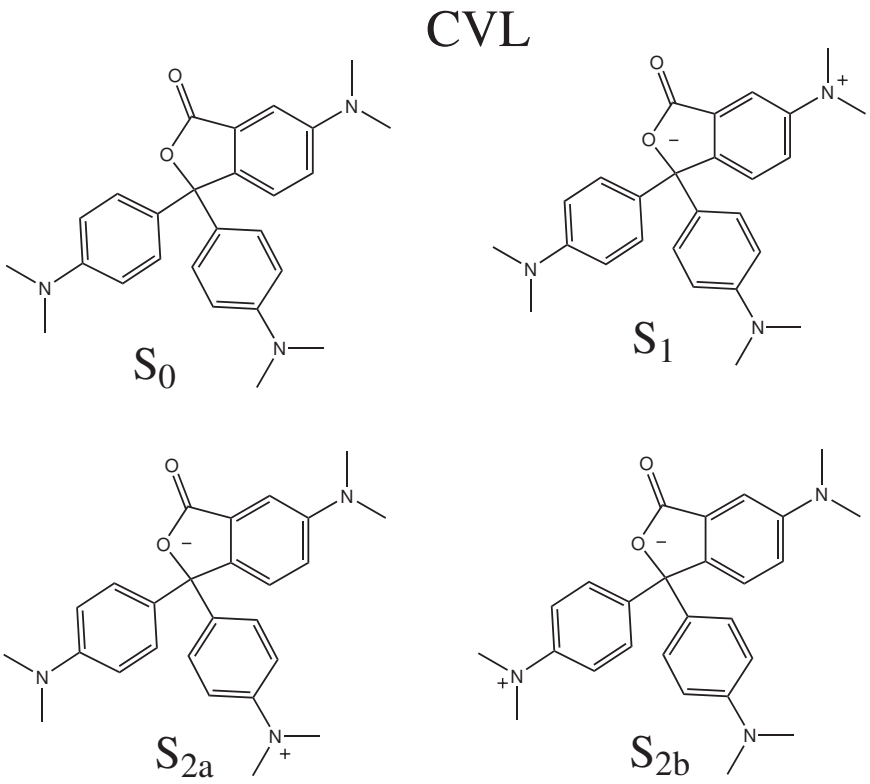

Figure 3.2: Electronic states of Crystal violet lactone

We used the 'Leap-frog' integration algorithm implemented in AMBER 9 for all our simulations. Cut-offs for both the Lennard-Jones and Coulombic interactions were set to 10Å. In order to deal with long-range electrostatic interactions, the PME algorithm was used. Identical schemes were used in simulations of CVL in acetonitrile.

Potential energy parameters for the [NTf_2^-]anion are taken from the work of Lopes and Pádua[88], while for the [Pr_{31}^+]cation charges are those in reference [17] while all other parameters are taken from the generalized AMBER force field[19].

Except for the charges, all parameters for CVL in the ground and excited states are taken to be identical and obtained from the generalized AMBER force field[19]. In all cases interactions are taken as in the AMBER force field convention in which intramolecular nonbonded energies are neglected for atoms that are less than three bonds apart and are reduced to 50% for the atoms separated exactly by three bonds. Parameters for acetonitrile are taken from literature[46].

3.2.1 Electronic states of CVL

Ground-state charges for CVL were obtained from an ab initio ESP-fit(Electro Static Potential) at the Hartree Fock (HF)/6-31G* theory level using the Gaussian program[36] and are provided in the Appendix A.

Generating a model for the excited states of CVL is complex. Electronically excited state calculations for this molecule yield a large number of states with similar energies and dipole moments. Our task was greatly facilitated by a very insightful article by Karpiuk[75] in which he demonstrates that the two states involved

in electron transfer are localized. Specifically the S_1 excitation is localized on the aminophthalide ring and emission from this state is almost identical to that of fragment 6-dimethylaminophtalide a much simpler molecule. A highly accurate Complete Active Space Self Consistent Field(CASSCF) electronic structure calculation for the S_1 state of 6-dimethylaminophtalide is available in the literature[76]. Minor modifications to the differences in partial charges between ground and excited states reported for 6-dimethylaminophtalide generate a model for the S_1 state of CVL with the correct dipole moment (11 D).

By studying malachite green lactone which is also a fragment of CVL, Karpiuk demonstrated that the electron transfer to generate S_2 comes from one of the dimethylaniline groups. In the gas phase since these two dimethylaniline groups are symmetrical, either of them can act as the electron donor. In a liquid the situation is different and the surrounding solvent will impose a bias. In order to model the two local diabatic states S_{2a} and S_{2b} shown in Fig. 3.2 that give rise to adiabatic state S_2 we use an empirical valence bond (EVB) approach[140, 12]. The charges for the diabatic representations of S_2 are obtained by applying the changes in partial charges obtained for S_1 at the location of the amino group in the aminophthalide fragment to the amino group of either dimethylaniline fragments. Small adjustments were made in order to match the dipole moment of S_2 (25 D). All charges for the ground and excited state models of CVL are reported in the appendix.

The reactive S_2 potential is defined over the lowest adiabatic surface obtained by diagonalization of the EVB Hamiltonian matrix in Eq. 3.1.

$$\mathbf{H} = \begin{bmatrix} H_{11} & H_{12} \\ H_{21} & H_{22} \end{bmatrix} \tag{3.1}$$

In Eq. 3.1 the matrix elements H_{11} and H_{22} are the diabatic energies of states S_{2a} and S_{2b} depicted in Fig. 3.2. Since the S_2 state is recognized to be highly localized, the coupling element H_{12} and H_{21} are assumed to be small. In our simulations these weak coupling elements were taken to be constant at a value of 1.0 kcal/mol.

As will be shown, though these models are not perfect, they are able to qualitatively capture the correct changes in energetics as polarity changes from that in the gas phase to that in polar solvents.

3.2.2 Calculation of fluorescence spectra from molecular dynamics simulations

The emission energy ΔE_{em} from S_1 to S_0 or from S_2 to S_0 can be expressed as in Eq. 3.2.

$$\Delta E_{em} = \Delta E(g) + \Delta E_{sol} \tag{3.2}$$

Here $\Delta E(g)$ denotes the gas-phase or intramolecular energy difference that is independent of the solvent. This value cannot be obtained from classical molecular dynamics simulations but is experimentally accessible and can be found in the literature both for the S_1 to S_0 (27,180cm^{-1}) and S_2 to S_0 (30,165cm^{-1}) transitions[75].

ΔE_{sol} is the solute-solvent interaction energy difference arising from the distinct charge distributions in the ground and excited electronic states.

In the gas phase $\Delta E_{em} = \Delta E(g)$ and $\Delta\Delta E = \Delta E_{emS_2} - \Delta E_{emS_1} = 2985 cm^{-1}$. Interestingly, in a polar solvent, the value of $\Delta\Delta E$ becomes negative. As an example, judging from Figure 3 in reference [75], in acetonitrile $\Delta\Delta E$ obtained as the difference in the frequencies between the maximum of emission of S_2 and S_1 is approximately $-6500 cm^{-1}$. Our parameterization of the excited state potentials in the presence of acetonitrile yields a value $\Delta\Delta E = -9000 cm^{-1}$ which while not perfect, correctly captures the change in sign and correspondingly the change in energy ordering of the two excited states.

$$I_{ab}(\Delta E_{ex}) = \sum_l I^l_{ab}(\Delta E_{ex}), \tag{3.3}$$

$$I^l_{em}(\Delta E_{em}) = \int_0^\infty \delta(\Delta E(t) - \Delta E_{em}) \times e^{-\frac{t}{\tau_f}} dt, \tag{3.4}$$

$$I_{em}(\Delta E_{ex}, \Delta E_{em}) = \sum_l I^l_{em}(\Delta E_{em}) I^l_{ab}(\Delta E_{ex}), \tag{3.5}$$

Excitation frequency dependent emission intensities are computed using Eq. 3.3 through Eq. 3.5. Here $I^l_{ab}(\Delta E_{ex})$ is the probability distribution of absorption energy gaps ΔE_{ex} in trajectory l. $I_{ab}(\Delta E_{ex})$ denotes the total probability distribution at vertical transition excitation energy ΔE_{ex} computed as a sum over all trajectories. $I^l_{em}(\Delta E_{em})$ is the corresponding steady-state probability distribution of emission energy gaps ΔE_{em} weighted by an exponential decay corresponding to the lifetime (τ_f) of the probe (here assumed to be 1 ns) for trajectory l. $I_{em}(\Delta E_{ex}, \Delta E_{em})$ denotes the intensity or joint probability distribution of emission energy ΔE_{em} when excitation energy is ΔE_{ex}. In the calculation of $I_{em}(\Delta E_{ex}, \Delta E_{em})$, excitation, ΔE_{ex} is to state S_1. All the spectra are reported as area normalized.

3.2.3 Marcus parabolas

In the canonical ensemble the Helmholtz free energy F is

$$F = -RT \times ln(Q) \tag{3.6}$$

where Q is the canonical partition function. The free energy as a function of a special coordinate is

$$\begin{aligned} F(x) &= -kT \times ln\left(Q(x)\right) \\ &= -kT \times ln\left(\int d\bar{r} e^{-\beta E(x,\bar{r})}\right) \\ &= -kT \times ln\left(\frac{\int d\bar{r} e^{-\beta E(x,\bar{r})}}{\int dx d\bar{r} e^{-\beta E(x,\bar{r})}} \times \int dx d\bar{r} e^{-\beta E(x,\bar{r})}\right) \\ &= -kT \times ln\left(P(x)\right) - kT \times ln(Q) \\ &= -kT \times ln\left(P(x)\right) + F \end{aligned} \tag{3.7}$$

where $P(x)$ is the probability distribution function for coordinate x.

Defining $F_{S_1}(x)$ and $F_{S_2}(x)$ as the corresponding free energy functions in two different electronic states S_1 and S_2 one has

$$\begin{aligned} F_{S_1}(x) - F_{S_2}(x) &= (F_{S_1} - F_{S_2}) - kT \times ln\left(\frac{P_{S_1}(x)}{P_{S_2}(x)}\right) \\ &= F_{S_1} - F_{S_2} - kT \times ln\left(\frac{\int d\bar{r} e^{-\beta E_{S_1}(x,\bar{r})}}{\int d\bar{r} e^{-\beta E_{S_2}(x,\bar{r})}} \times \frac{\int dx d\bar{r} e^{-\beta E_{S_2}(x,\bar{r})}}{\int dx d\bar{r} e^{-\beta E_{S_1}(x,\bar{r})}}\right) \\ &= -kT \times ln\left(\frac{\int d\bar{r} e^{-\beta E_{S_1}(x,\bar{r})}}{\int d\bar{r} e^{-\beta E_{S_2}(x,\bar{r})}}\right) \end{aligned} \tag{3.8}$$

If as in previous publications [139, 81, 124, 65, 125], the order parameter x used as a reaction coordinate for the calculation of free energies is defined as

$$x = \Delta E = E_{S_2} - E_{S_1} \tag{3.9}$$

then $E_{S_2} = E_{S_1} + x$ and

$$\begin{aligned} F_{S_1}(x) - F_{S_2}(x) &= -kT \times ln\left(\frac{\int d\bar{r} e^{-\beta E_{S_1}(x,\bar{r})}}{\int d\bar{r} e^{-\beta x} e^{-\beta E_{S_1}(x,\bar{r})}}\right) \\ &= -x \end{aligned} \tag{3.10}$$

then

$$\Delta F(\Delta E) = F_{S_2}(\Delta E) - F_{S_1}(\Delta E) = \Delta E \tag{3.11}$$

If Marcus theory is applicable then the two free energy curves should be parabolae of identical curvature (see Fig 3.3). A combination of Eq. 3.8 and Eq. 3.11 with the Marcus assumption is sufficient to algebraically define the curvature of $F_{S_1}(\Delta E)$ and $F_{S_2}(\Delta E)$ as well as the value of the Helmholtz free energy difference $\Delta F^\circ = F_{S_2} - F_{S_1}$.

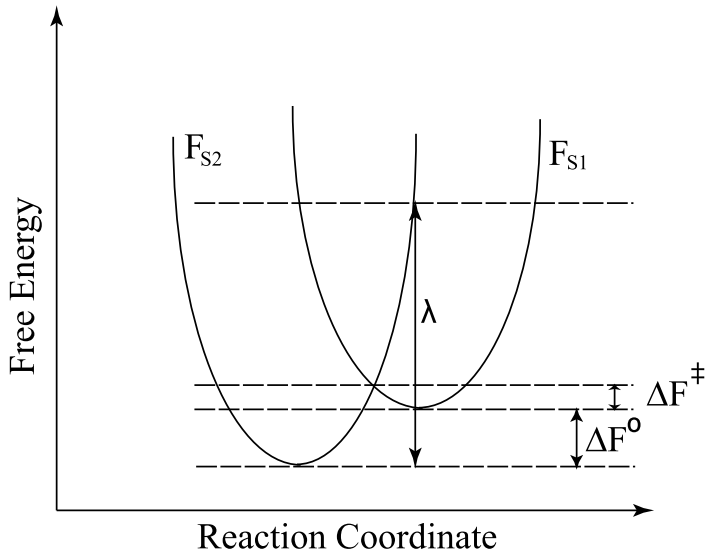

Figure 3.3: Cartoon defining various quantities of the Marcus parabolae

$$\begin{aligned}\Delta E &= \Delta F^{\circ} - kT \times ln\left(P_{S_2}(\Delta E)\right) + kT \times ln\left(P_{S_1}(\Delta E)\right) \\ &= \Delta F^{\circ} + \gamma(\Delta E - \Delta E_{S_2})^2 - \gamma(\Delta E - \Delta E_{S_1})^2\end{aligned}$$

which leads to the set of equations

$$\Delta F^{\circ} = \gamma(\Delta E_{S_1}^2 - \Delta E_{S_2}^2) \tag{3.12}$$

$$\Delta E_{S_1} - \Delta E_{S_2} = \frac{1}{2\gamma} \tag{3.13}$$

Here, ΔE_{S_1} and ΔE_{S_2} are the corresponding average values of the energy gap $E_{S_2} - E_{S_1}$ over two trajectories with identical initial conditions but with dynamics driven by states S_1 and state S_2 respectively such as shown in Fig. 3.4 for which statistics is always very good. Since only two numbers, namely ΔE_{S_1} and ΔE_{S_2}, are needed to establish the curvature of the free energies and ΔF°, one can use the rest of the data to verify whether the Marcus approximation is valid. Using an approach similar to that described by Tachiya [124], Eq. 3.11 can be used to extrapolate the free energy to regions that are not sampled during simulations. As an example, using data from two trajectories one run with potential corresponding to state S_1 and the other corresponding to state S_2, ΔE can be computed. With these data, probability distribution functions and $-kTln\left(P(\Delta E)\right)$ can be computed as in Fig. 3.5 and Fig. 3.6. For each electronic state, the functions displayed in Fig. 3.6 only sample regions around equilibrium. Using Eq. 3.11 and ΔF° as an adjustable constant, these functions can be extended without invoking the Marcus approximation. Color coded segments in Fig. 3.7 indicate how one can extend the Helmholtz free energy function for state S_1 by using data around the equilibrium configuration of state S_2 and vice

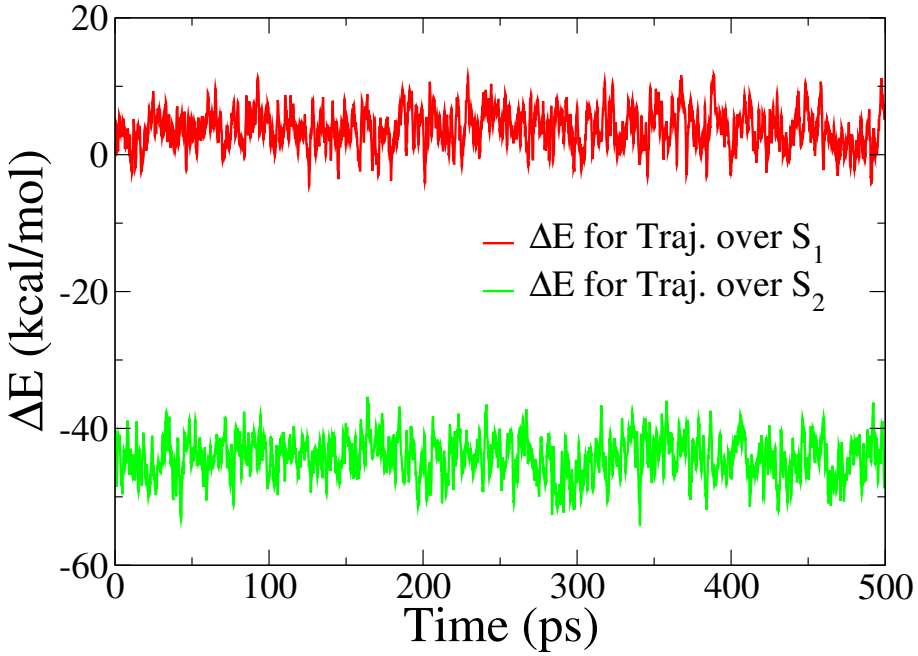

Note: ΔE (red) for trajectory in electronic state S_1 (green) for trajectory in electronic state S_2

Figure 3.4: Energy gaps as function of time.

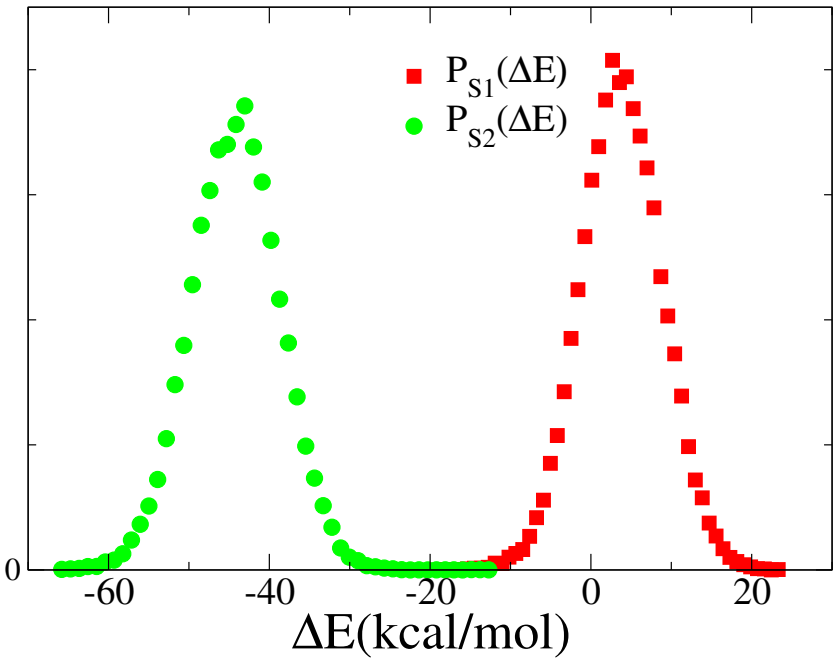

Figure 3.5: Probability distribution functions $P_{S_1}(\Delta E)$ and $P_{S_2}(\Delta E)$

versa. Region 1 (red ■) of S_1 is used to obtain Region 4 of S_2 while Region 3 (green •) of S_2 is used to obtain Region 2 of S_1.

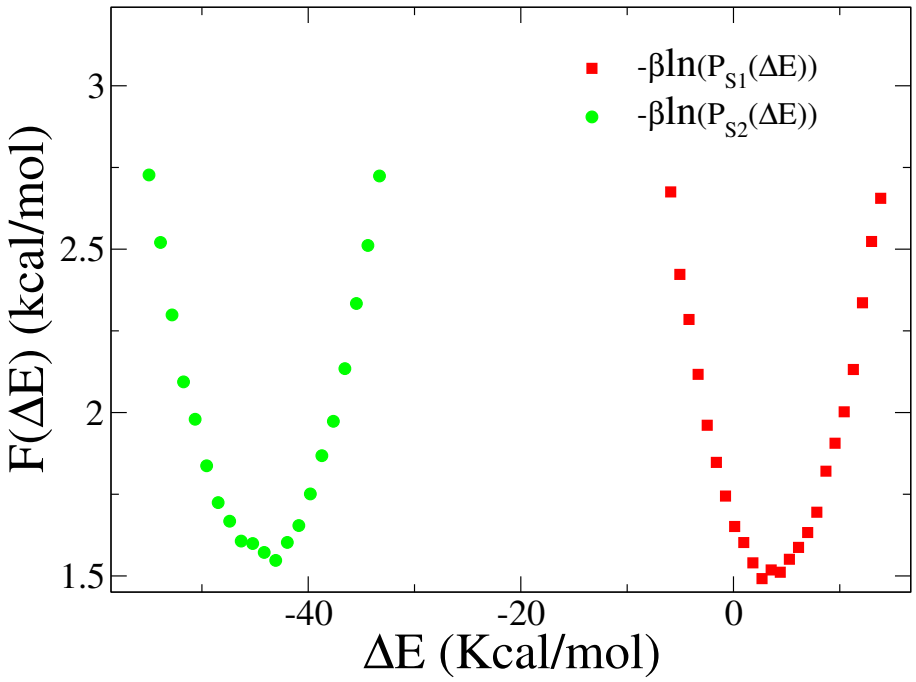

Note: $-kt \times ln\,(P_{S_1}(\Delta E))$ and $-kt \times ln\,(P_{S_2}(\Delta E))$

Figure 3.6: Free-energy curves

If the overall curves $F_{S_2}(\Delta E)$ and $F_{S_1}(\Delta E)$ can be made to overlap with the Marcus parabolae computed only from the values ΔE_{S_1} and ΔE_{S_2} then the approximation is verified.

It is important to emphasize that ΔE_{S_1} and ΔE_{S_2} energy differences such as those shown in Fig 3.4 are local in nature. By this we mean that because of the slow nature of the solvent on a time scale relevant to the electron transfer process ΔE_{S_1} and ΔE_{S_2} are not the same for all trajectories instead they are local solvent

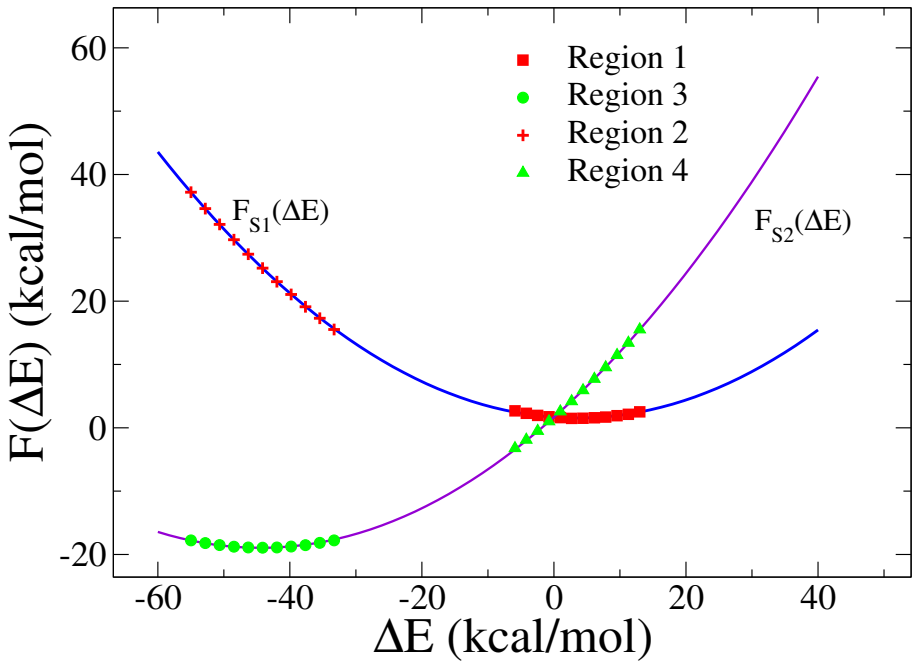

Note: Free energy curves obtained from simulation and by extrapolation as described in the text

Figure 3.7: Total Free-energy curves

environment dependent.

3.2.4 Excitation wavelength dependent Marcus parabolas

Similar to the way in which we compute absorption wavelength dependent emission spectra one can compute the joint probability $P_{S_1}(\Delta E_{ex}, \Delta E)$ of observing an energy gap between the two excited states $E_{S_2} - E_{S_1} = \Delta E$ during simulation, given that the dynamics is driven by state S_1 when CVL was originally photo-excited into state S_1 with the energy ΔE_{ex}.

$$P_{S_1}(\Delta E_{ex}, \Delta E) = \sum_l P^l_{S_1}(\Delta E) P^l_{ab}(\Delta E_{ex}) \tag{3.14}$$

$$P_{S_2}(\Delta E_{ex}, \Delta E) = \sum_l P^l_{S_2}(\Delta E) P^l_{ab}(\Delta E_{ex}) \tag{3.15}$$

Similarly $P_{S_2}(\Delta E_{ex}, \Delta E)$ is the joint probability distribution of ΔE with dynamics driven by S_2 when the excitation energy into S_1 is ΔE_{ex}. These two probability distributions are used to compute excitation frequency dependent free energy curves.

3.3 Results and Discussion

3.3.1 Emission spectra

Figure 3.8 shows computed emission spectra from CVL fluorescent states S_1 and S_2 for an ensemble of trajectories in acetonitrile. Consistent with Karpiuk's [75] experiments the fluorescence emission of state S_2 appears at lower energy. All independent NVE simulations result in almost identical spectra. Consistent with these results, free energies computed from our ensemble of independent calculations show almost identical Marcus parabolae shown in Fig. 3.12.

The case of CVL in room temperature ionic liquid is quite different. If we consider the emission from S_1 and S_2 states without allowing for electron transfer, one obtains the spectra in Fig. 3.9(a). The emission spectrum of each independent trajectory is significantly different. This is a phenomenon that has been previously explained through the earlier research work from our group [60, 62] and that is commonly experimentally observed in ionic liquids because of heterogeneity and slow dynamics. Key experimental articles describing this type of behavior are those by Samanta and coworkers [93, 94, 100, 112] and Sarkar and coworkers [26, 24, 23, 25].

Clearly, the differences in emission spectra are due to the fact that each independent trajectory has CVL in a different local environment and these environments

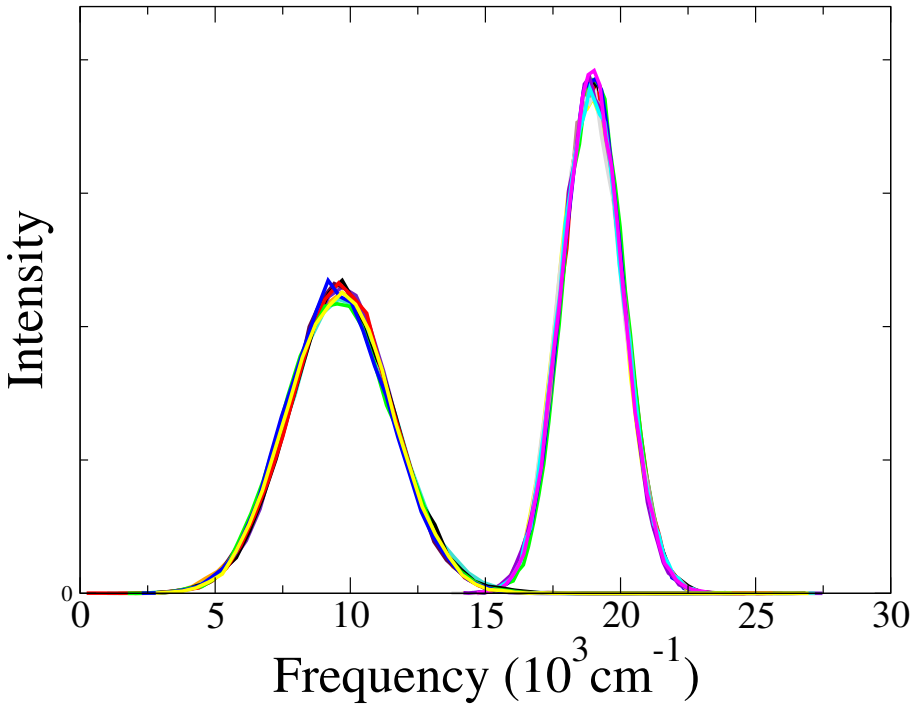

Note: Emission spectra of S_1 and S_2 states of CVL in acetonitrile. The set of curves on the right correspond to emission from state S_1 and the set of curves on the left correspond to emission from state S_2. Each line corresponds to a different molecular dynamics trajectory

Figure 3.8: Emission Spectra of CVL acetonitrile

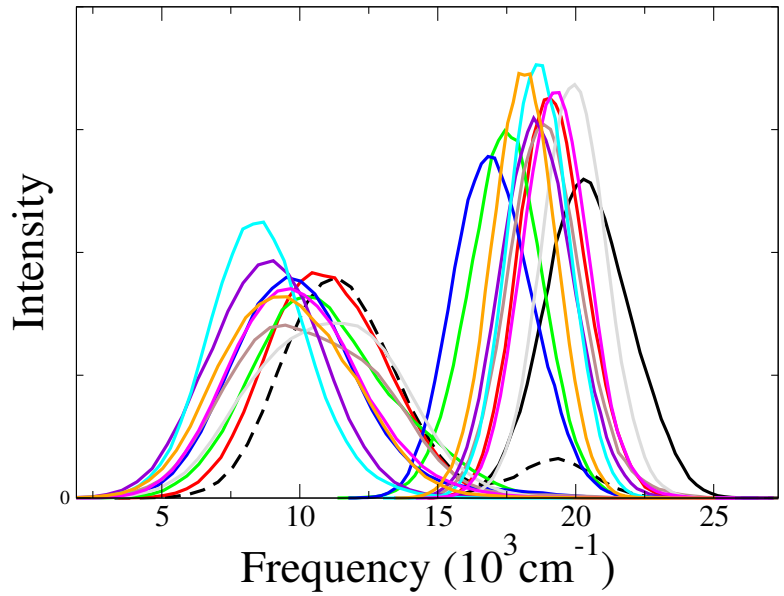

(a)

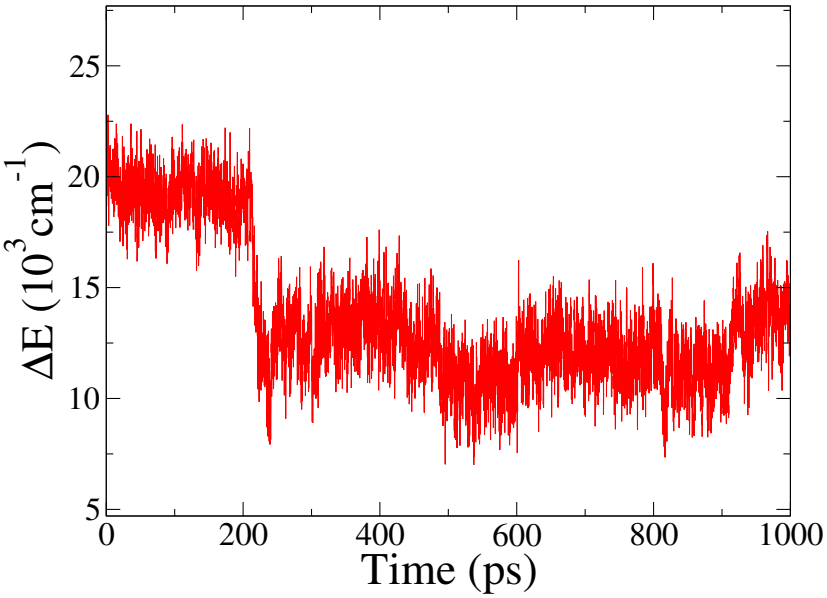

(b)

(a)Emission spectra of S_1 and S_2 states of CVL in $[Pr^{+}_{31}][NTf_2{}^{-}]$. The set of curves on the right correspond to emission from state S_1 and the set of curves on the left correspond to emission from state S_2. Each line corresponds to a different molecular dynamics trajectory.(b) ΔE as a function of time for the trajectory giving rise to the spectrum in Fig. 3.9(a) represented with dotted lines.

Figure 3.9: Emission Spectra of CVL in ionic liquid

are in slow exchange on a time scale compatible with the lifetime of either excited states of CVL. The most interesting aspect of this observation is that this heterogeneity can be exploited by photo-selecting probe molecules that are in particular solvent environments. Just like in a normal hole burning experiment, by changing the frequency of the incident light one can selectively excite a sub ensemble of fluorophores. The main difference being that in the room temperature ionic liquid the memory of this photo-selection remains active throughout the lifetime of either excited state. In essence these subensembles experience different surrounding local solvent polarities that are not time averaged on a time scale of the lifetime of the excited state molecule. Of course photo-selection also occurs in acetonitrile, but memory of this is lost within the first few picoseconds of excited state life.

It is interesting to consider the special case of one of our trajectories driven by S_2 shown in dashes in Fig 3.9(a). If we closely observe this spectrum we see that it has two peaks both corresponding to S_2 emission. In Fig. 3.9(b) we show ΔE_{em} as a function of time for this particular trajectory. It is clear that we are capturing a rare reorganization event since it only occurs in one of our trajectories. The fact that these events are uncommon explains why each trajectory has a different spectrum on this time scale.

3.3.2 Excitation wavelength dependent emission in room temperature ionic liquids

In fig 3.10 we show the excitation frequency dependent emission spectra calcu-

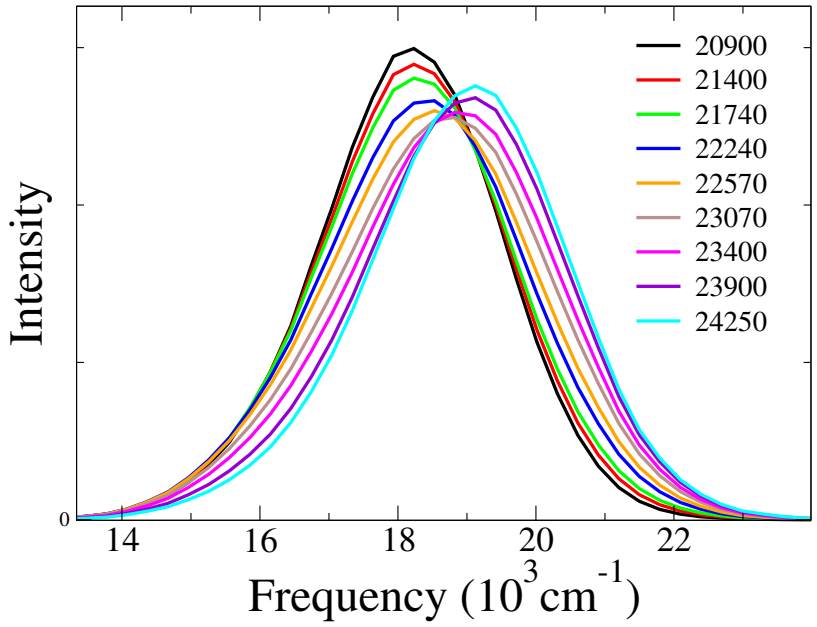

(a)

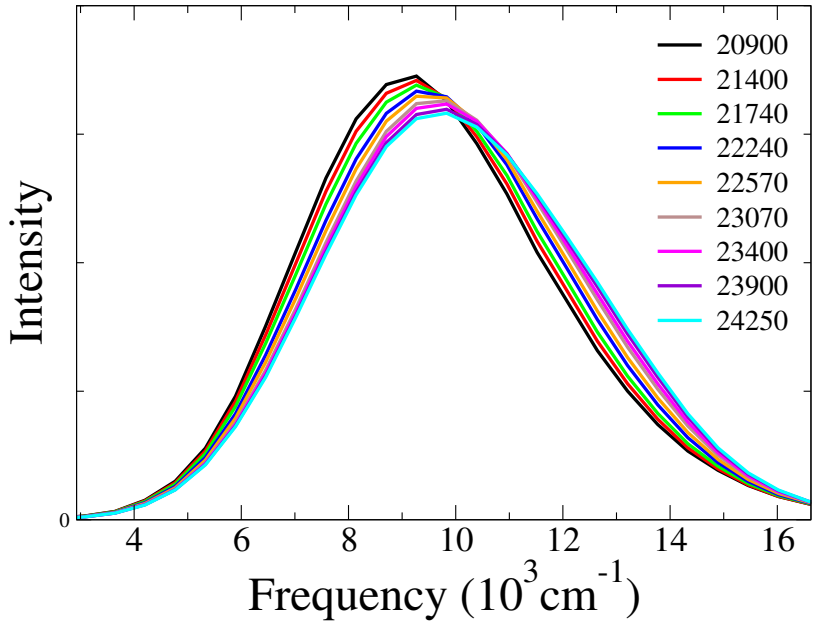

(b)

Note: Excitation dependent emission spectra (a) for S_1, (b) for S_2. Absorption frequencies in legend are in units of cm^{-1}

Figure 3.10: Excitation dependent emission spectra of CVL in ionic liquid

lated using Eq. 3.5. We can clearly see that the emission spectra from S_1 and S_2 are redshifted upon excitation towards the lower frequencies. In Fig. 3.11 we also show the maximum of emission plotted against excitation energies.

3.3.3 Electron transfer between S_1 and S_2 states of CVL

In Fig. 3.13 we show free energy curves for the electron transfer process between S_1 and S_2 in the ionic liquid. Interestingly and consistent with the work of Kim and Lynden Bell[90, 89, 91, 123, 121, 120], each couple of trajectories in the same local environment but under different electronic potentials corresponding to S_1 and S_2 give rise to color coded free energies curves that satisfy the Marcus relationship. However these Marcus curves are different in each local environment!

When we compare our free energy curves computed in acetonitrile with those in the ionic liquid it is quite obvious that the kinetics and thermodynamics of electron transfer will be absorption wavelength dependent in the room temperature ionic liquid but independent in the conventional solvent. In fact what this means is that the room temperature ionic liquid offers an extra degree of control on chemical reactivity. We can rationally choose to modify the outcome of an electron transfer reaction simply by means of initial sub-ensemble selection.

If we look at the values in table 3.1 and 3.2 we see that the curvatures of the parabolae in different local environments are different in the case of the room temperature ionic liquid but not in the case of acetonitrile. The curvature of the free energy

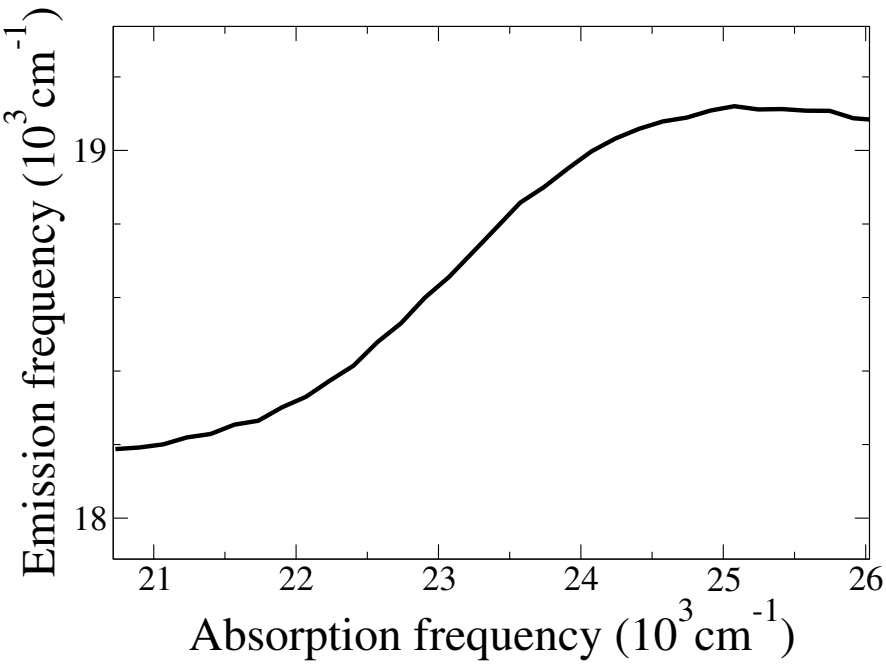

(a)

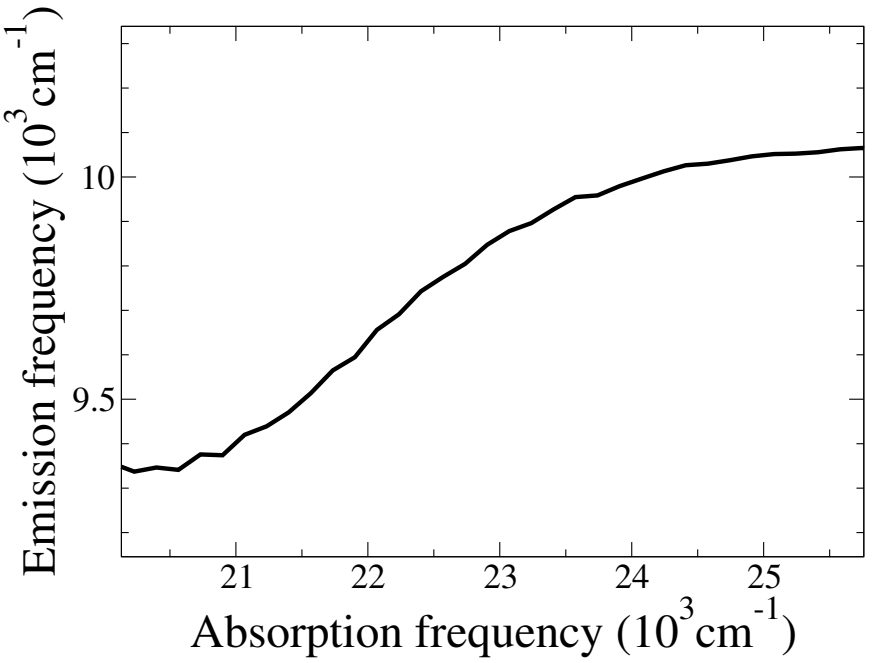

(b)

Note: Peaks of emission spectrum vs excitation frequency (a) for S_1 , (b) for S_2.

Figure 3.11: Emission maxima vs excitation frequency for S_1 and S_2

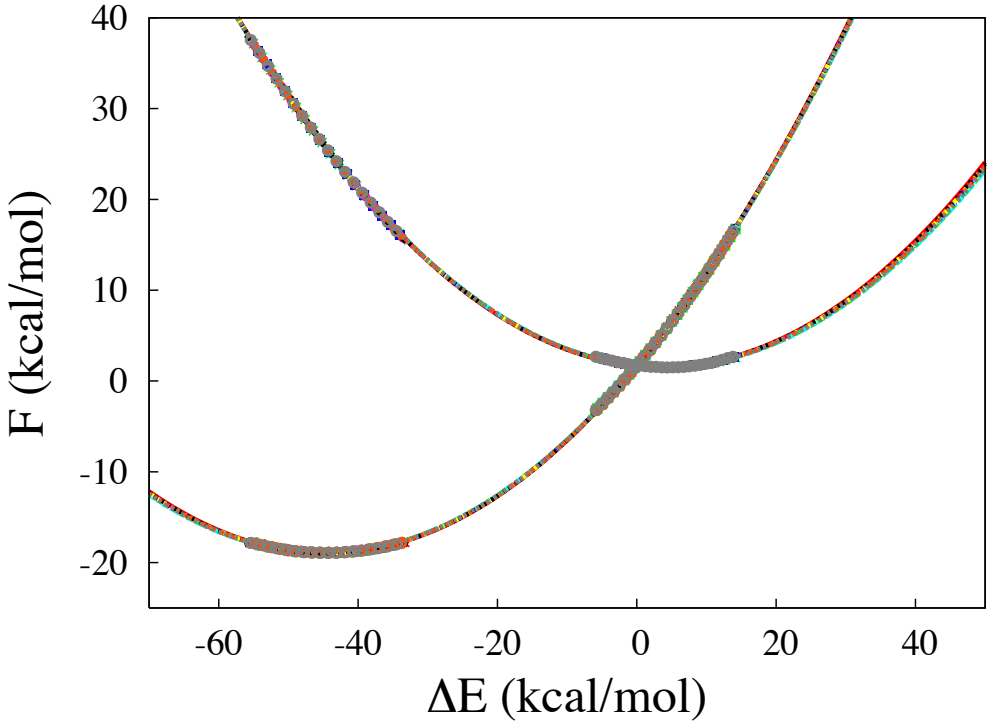

Note: Free energy curves for intramolecular electron transfer of CVL in acetonitrile. The curves on the right of each graph are for F_{S_1}, and curves on the left are for F_{S_2}. Each curve with different color represents a different MD trajectory

Figure 3.12: Marcus parabolas in acetonitrile

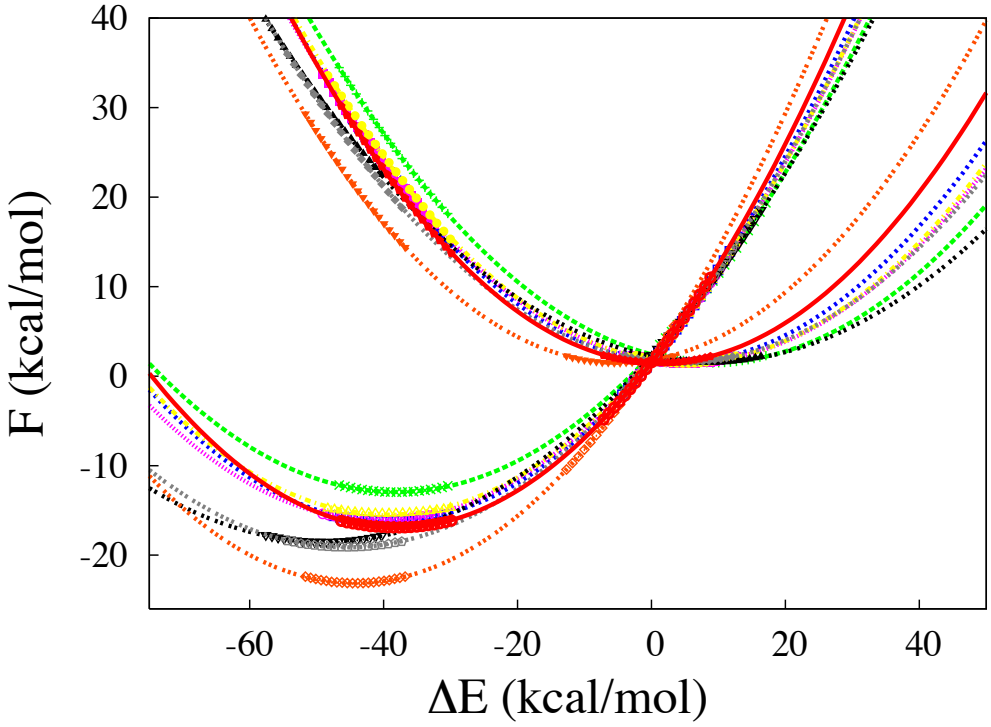

Note: Free energy curves for intramolecular electron transfer of CVL in room temperature ionic liquid. The curves on the right of each graph are for F_{S_1}, and curves on the left are for F_{S_2}. Each curve with different color represents a different MD trajectory

Figure 3.13: Marcus parabolas in ionic liquid

Table 3.1: Parameters of Marcus parabolas in acetonitrile

	F_{S_1}			F_{S_2}		
Trajectory	a	b	c	a	b	c
1	0.0104	3.48	1.54	0.0104	-44.47	-18.95
2	0.0102	3.94	1.54	0.0102	-44.92	-18.95
3	0.0103	3.73	1.54	0.0103	-44.72	-18.95
4	0.0103	3.78	1.55	0.0103	-44.80	-18.96
5	0.0102	3.97	1.56	0.0102	-44.99	-18.95
6	0.0103	3.68	1.55	0.0103	-44.70	-18.96
7	0.0104	3.59	1.55	0.0104	-44.63	-18.97
8	0.0103	3.76	1.54	0.0103	-44.74	-18.95
9	0.0103	3.86	1.56	0.0103	-44.86	-18.95
10	0.0102	4.09	1.56	0.0102	-45.12	-18.95

Note: Parameters obtained by fitting the free energy data in the case of acetonitrile to quadratic equation $y = a(x - b)^2 + c$. x and y are in units of kcal/mol

is directly related to the polarity of the solvent around the solute[125]. In table 3.3 we report the free energies computed from various pairs of trajectories characterized by their local environment. The definitions of the various Helmholtz free energy quantities are displayed in Fig. 3.3. These values clearly show the difference between conventional polar solvents and this room temperature ionic liquid. In the case of the room temperature ionic liquid the solvation free energies (ΔF°) are significantly

Table 3.2: Parameters of Marcus parabolas in ionic liquid

	F_{S_1}			F_{S_2}		
Trajectory	a	b	c	a	b	c
1	0.0122	0.70	1.50	0.0122	-40.42	-18.37
2	0.0106	9.19	1.53	0.0106	-38.15	-12.94
3	0.0116	3.77	1.51	0.0116	-39.34	-16.27
4	0.0109	5.34	1.52	0.0109	-40.62	-16.12
5	0.0090	8.73	1.58	0.0090	-47.05	-17.59
6	0.0112	5.34	1.52	0.0112	-39.35	-15.49
7	0.0087	8.68	1.58	0.0087	-48.80	-18.48
8	0.0127	-4.91	1.49	0.0127	-44.30	-23.12
9	0.0100	4.26	1.55	0.0100	-45.62	-19.13
10	0.0127	1.25	1.48	0.0127	-38.13	-16.96

Note: Parameters obtained by fitting the free energy data in the case of ionic liquid to quadratic equation $y = a(x-b)^2 + c$. x and y are in units of kcal/mol

different for the various environments while they are basically identical in the case of acetonitrile. Similarly the activation free energies ($\Delta F^{\ddagger}$), and therefore the local kinetics, as well as the solvent reorganization free energies (λ) are also significantly different in the room temperature ionic liquid.

$$k \propto e^{-\beta \Delta F^{\ddagger}} \tag{3.16}$$

Table 3.3: Free Energies for various trajectories in acetonitrile and ionic liquid

	Acetonitrile			Ionic liquid		
Trajectory	$\Delta F^{\ddagger}$	ΔF°	λ	$\Delta F^{\ddagger}$	ΔF°	λ
1	0.13	20.50	23.98	0.01	19.86	20.56
2	0.16	20.49	24.43	0.89	14.48	23.67
3	0.14	20.50	24.22	0.16	17.79	21.55
4	0.15	20.51	24.29	0.31	17.64	22.98
5	0.16	20.51	24.48	0.68	19.16	27.89
6	0.14	20.51	24.19	0.32	17.00	22.34
7	0.13	20.52	24.11	0.66	20.06	28.74
8	0.15	20.49	24.25	0.31	24.61	19.70
9	0.15	20.50	24.36	0.18	20.68	24.94
10	0.17	20.51	24.60	0.02	18.44	19.69

Note: Solvation free energy ΔF°, activation free energy $\Delta F^{\ddagger}$, and reorganization free energy λ in kcal/mol

According to transition state theory the rate constant for reaction k, depends on the activation energy as in Eq. 3.16. The electron transfer process between excited states of CVL has different activation energies, so one can expect to have locally different transfer rates. Table 3.1 shows the value of the curvatures for F_{S_1} and F_{S_2} computed independently for each particular pair of trajectories in the same local environment. Since in each case local curvatures are almost identical for states S_1 and S_2 Marcus

theory is locally applicable. However an analysis across trajectories demonstrates that reaction kinetics at each local environment level will be significantly different.

It is important to emphasize that our classical calculations can only access the solvent contribution to the free energy. In order to compare with the exact experimental kinetic values, we would need to account for the correct solute contribution to the free energy and for quantum factors. Nonetheless one can use our results to test the trends to be expected if the electron transfer process occurred in the normal and inverted regions.

In fig 3.14 we show our excitation wavelength dependent free energy curves computed using eqs: 3.14 and 3.15. It is clear that as the excitation energy increases the solvent contribution to the free energy barrier for electron transfer also increases. This is also shown in fig 3.15(a).

In our study, the electron transfer appears to occur in the normal Marcus region. If we displace the Marcus parabolae such that they intersect in the inverted region we see in Fig. 3.15(b) that the trend in activation energies gets reversed.

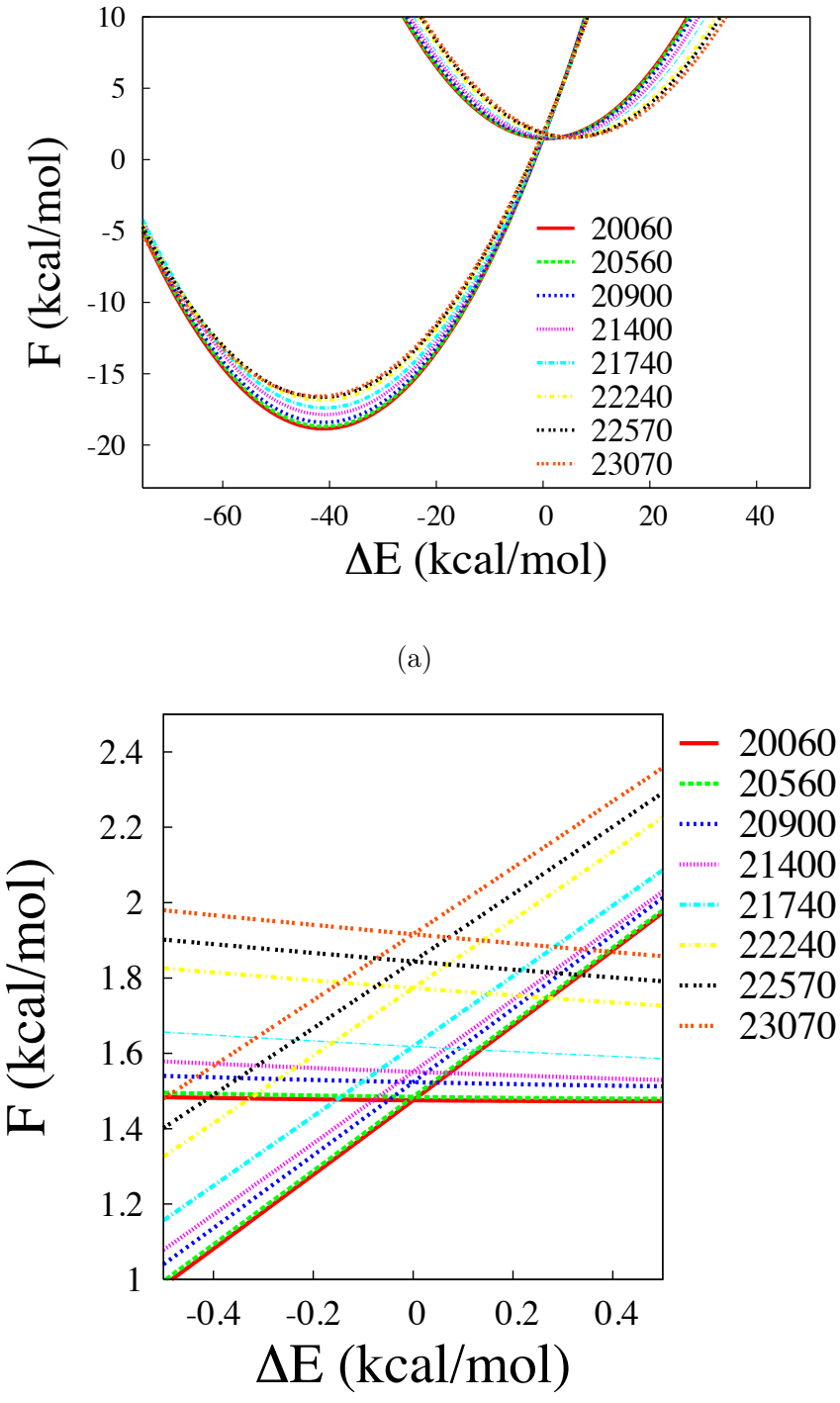

(a)

(b)

Note: Free energy plots at various excitation frequencies (a)Complete curves, (b)Near the crossing point. Absorption frequencies in legend are in units of cm^{-1}

Figure 3.14: Excitation dependent Marcus parabolas

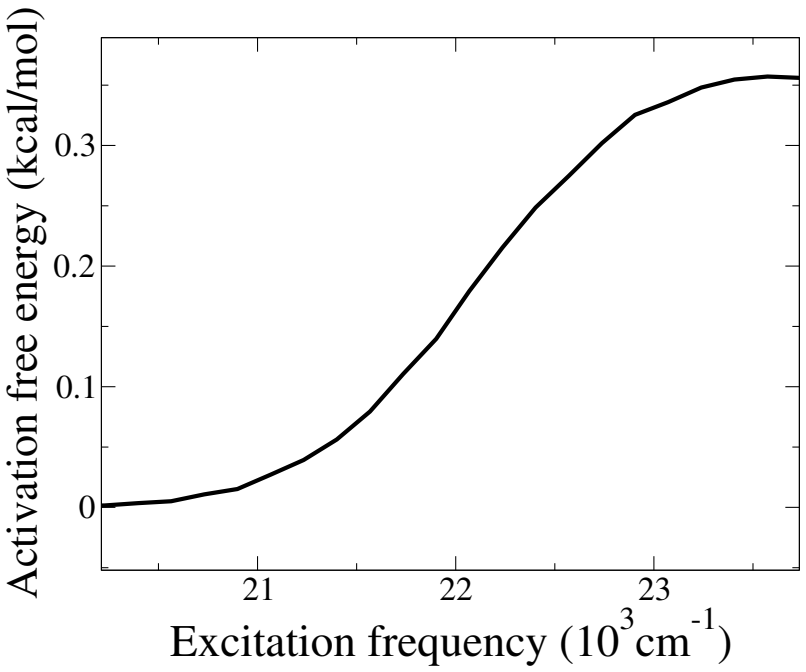

(a)

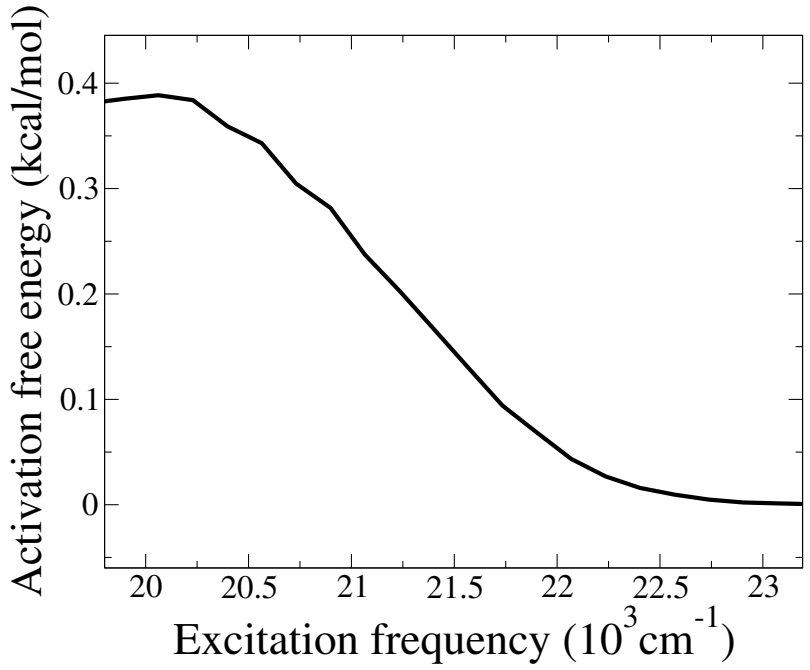

(b)

Note: Activation free energy($\Delta F^{\ddagger}$) vs excitation frequency in (a) Normal (b) Inverted region. We can clearly see that the trend is reversed in the case of inverted region

Figure 3.15: Activation free energy vs excitation frequency

3.4 Conclusion

In this chapter we demonstrated that the thermodynamics and kinetics of intramolecular electron transfer following photoexcitation of CVL in $[Pr_{31}^{+}][NTf_2{}^{-}]$is local solvent environment dependent. Our results provide molecular level understanding of experiments in which the reaction kinetics is observed to be an absorption wavelength dependent[83, 113, 79, 80, 111]. Due to the time scale difference between the electron transfer process (fast) and the dynamics of the solvent (slow) by selective red-edge excitation one is able to influence the outcome of an electron transfer reaction. On the contrary, in acetonitrile, the outcome of the electron transfer reaction is independent of excitation frequency.

CHAPTER 4
EFFECTS OF WATER ON IONIC LIQUIDS

4.1 Introduction

An important concern when working with ionic liquids is the effect of water contamination on their dynamics and thermodynamics. We are also particularly interested in the effect that water has on spectroscopy. Experimental[24, 23, 8, 33, 118, 16, 128, 82, 110, 5] and computational[69, 78, 82, 50, 49] studies have been carried out to shed light on different energetic and thermodynamic properties of mixed solvents including ionic liquids. The addition of small amounts of water alters densities, viscosities as well as the fluorescence spectroscopy of molecules dissolved in these liquids. The presence of water in room temperature ionic liquids decreases their viscosity and results in faster solvent dynamics[118]. Several infrared studies[82, 110, 16, 128] and simulations[49, 50, 69] have shown that anions are mainly responsible for the interaction between ionic liquids and water.

In this chapter, we explain how water affects the dynamical behavior of $[C_6MIM^+][PF_6^-]$ by analyzing the steady state spectrum and dynamical Stokes shift of Coumarin-153 dissolved in this system. We also analyze rotational and translational correlation functions of the solvent in the presence and absence of water. Our simulations are motivated by the interesting experiments carried out by Sarkar and coworkers [24]. The choice of ionic liquid and water concentration are based on their studies, so that our computational results can be closely compared to their experi-

ments. A sketch of the ionic liquid and probe involved is depicted in Fig. 4.1

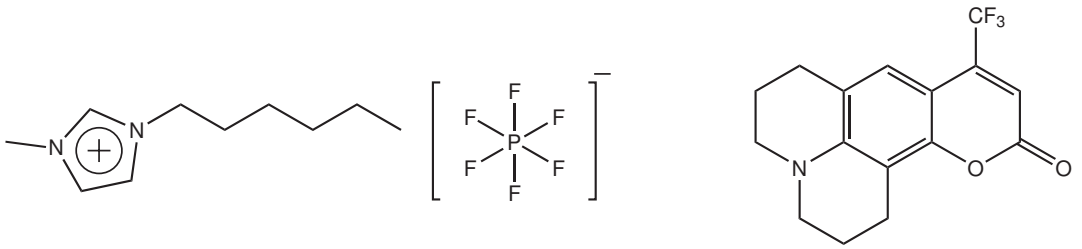

cation: 1-Hexyl-3-methylimidazolium($[C_6MIM^+]$), anion: hexafluorophosphate($[PF_6^-]$) and fluorescent probe: Coumarin-153.

Figure 4.1: Structure of $[C_6MIM^+]$ $[PF_6^-]$ and Coumarin-153

4.2 Simulations and Methods

We performed molecular dynamics simulation for the system $[C_6MIM^+][PF_6^-]$ using the software GROMACS [86, 10]. Potential energy parameters are those previously used in our group[95, 96]. Both Neat-IL and IL+Water simulations were performed in NVE ensemble with a box size of 5nm. The cut-off for both the Lennard-Jones and Coulombic interactions is 1.5nm. The integration algorithm used for the molecular dynamics simulations is "Leap-frog". To compute the absorption and emission spectra of Coumarin-153 in Neat-IL and IL+water, we used an ensemble of 13 MD trajectories. Each of these trajectories consisted of a Coumarin-153 molecule and 303 pairs of $[C_6MIM^+][PF_6^-]$ solvent ions. Simulations involving water have extra 62 SPC[9] water molecules added to the original system. This corresponds to a concentration of 0.17 mole fraction of water.

The ground state charges of Coumarin-153 were obtained from an *ab initio* ESP-fit at the (Hartree Fock(HF)/6-31G*) theory level using the Gaussian program[36]. The excited state charges were estimated by computing the ground (S_0) and first singlet excited state (S_1) charge difference using the ZINDO(Zerner's intermediate neglect of differential overlap) Hamiltonian with configuration interaction[108]. These calculations were performed with the software Hyperchem 7[66]. The charges in the excited state used for our MD calculations were obtained by adding the charge difference obtained from the ZINDO calculation to the ground state charges obtained by the HF method. The calculated ground and excited state dipole moments were 7.2 and 18.2 Debyes respectively. This methodology has already been successfully applied in the past by Maroncelli and coworkers to study ground and excited state dynamics of betaine-30 and also coumarin-153[98, 84]. Lennard-Jones, stretching, bending and torsional parameters for Coumarin-153 were taken to be the same in the ground and excited electronic state. This is a reasonable approximation given that coumarin is a fairly rigid planar molecule. These parameters were adopted from the OPLSAA force field [72]. We use the same methododology as described in Chapter 3 to compute the absorption wavelength dependent spectra of probe molecules in ionic liquids. Equations 4.1 through 4.5 are used in order to compute the time dependent and time independent spectra from an ensemble of trajectories in which Coumarin-153 is initially equilibrated in its ground electronic state and then photo-excited into its first singlet excited electronic state.

$$I_{ab}(\Delta E_{ex}) = \sum_{l} I^{l}_{ab}(\Delta E_{ex}), \tag{4.1}$$

$$I^{l}_{em}(\Delta E_{em}) = \int_{0}^{\infty} \delta(\Delta E(t) - \Delta E_{em}) \times e^{-\frac{t}{\tau_f}} dt, \tag{4.2}$$

$$I^{l}_{em}(\Delta E_{em}, t) = \int_{t-\Delta t}^{t+\Delta t} \delta(\Delta E(\tau) - \Delta E_{em}) \times e^{-\frac{\tau}{\tau_f}} d\tau, \tag{4.3}$$

$$I_{em}(\Delta E_{ex}, \Delta E_{em}) = \sum_{l} I^{l}_{em}(\Delta E_{em}) I^{l}_{ab}(\Delta E_{ex}), \tag{4.4}$$

$$I_{em}(\Delta E_{ex}, \Delta E_{em}, t) = \sum_{l} I^{l}_{em}(\Delta E_{em}, t) I^{l}_{ab}(\Delta E_{ex}). \tag{4.5}$$

$I^{l}_{ab}(\Delta E_{ex})$ is the probability distribution of absorption energy gaps ΔE_{ex} in trajectory l. $I_{ab}(\Delta E_{ex})$ denotes the total probability distribution at vertical transition excitation energy ΔE_{ex} computed as a sum over all trajectories. $I^{l}_{em}(\Delta E_{em})$ is the corresponding steady-state probability distribution of emission energy gaps ΔE_{em} weighted by an exponential decay corresponding to the lifetime (τ_f) of the probe (assumed to be 4.85 ns in the neat $[C_6MIM^+][PF_6^-]$ and 4.11 ns in the water mixtures[24, 114]) for trajectory l. $I^{l}_{em}(\Delta E_{em}, t)$ is the time-dependent intensity of emission computed from trajectory l after initial photo-excitation. $I_{em}(\Delta E_{ex}, \Delta E_{em})$ denotes the intensity or joint probability distribution of emission energy ΔE_{em} when excitation energy is ΔE_{ex}. Correspondingly $I_{em}(\Delta E_{ex}, \Delta E_{em}, t)$ stands for the time-dependent emission spectrum. It should be noted here that these are purely classical simulations.

As described in Chapter 3, emission energy is calculated using Eq. 3.2 The gas phase component $\Delta E(g) = 356nm$ is obtained from our quantum calculations and the experimental value is 368nm[32]. $\Delta E(g)$ is just an arbitrary constant that

shifts the spectra and is totally independent of the solvent. And the other component ΔE_{sol} is due to the difference in interactions between the solvent with the ground and excited states of the probe molecule. All the plots of emission spectra are area normalized.

4.3 Results and Discussion

4.3.1 Structure

Water-anion and water-cation radial distribution functions are shown in the Fig. 4.2. It is clear that the first peak of g(r) is much more prominent in the case of the anion. We only show results for C3 in the case of the cation (this is the carbon atom in between the two nitrogens) but results are similar if the center of mass of the cation ring or any of the other ring atoms are chosen instead. Our result indicating close hydrogen bonding interactions between water and the anions is in agreement with recent experiments [16] of attenuated total reflectance infrared spectroscopy for IL-water systems based on the 1-alkyl-3-methylimidazolium cation involving various different anions. The strength of the H-bonding between water molecules and different anions appears from these experiments to increase in the order $[PF_6]^- < [SbF_6]^- < [BF_4]^- < [(CF_3SO_2)_2N]^- < [ClO_4]^- < [CF_3SO_3]^- < [NO_3]^- < [CF_3CO_2]^-$. Koddermann et al. [82] combined FTIR spectroscopy and density functional calculations and also found that water molecules are mainly H-bonded to the anions. Similar conclusions have previously been reached in the molecular dynamics studies of water-dimethylimidazolium chloride mixtures by Lynden-Bell and coworkers [49, 50], and in

the case of water and 1-octyl-3-methylimidazolium nitrate by Voth and coworkers [69].

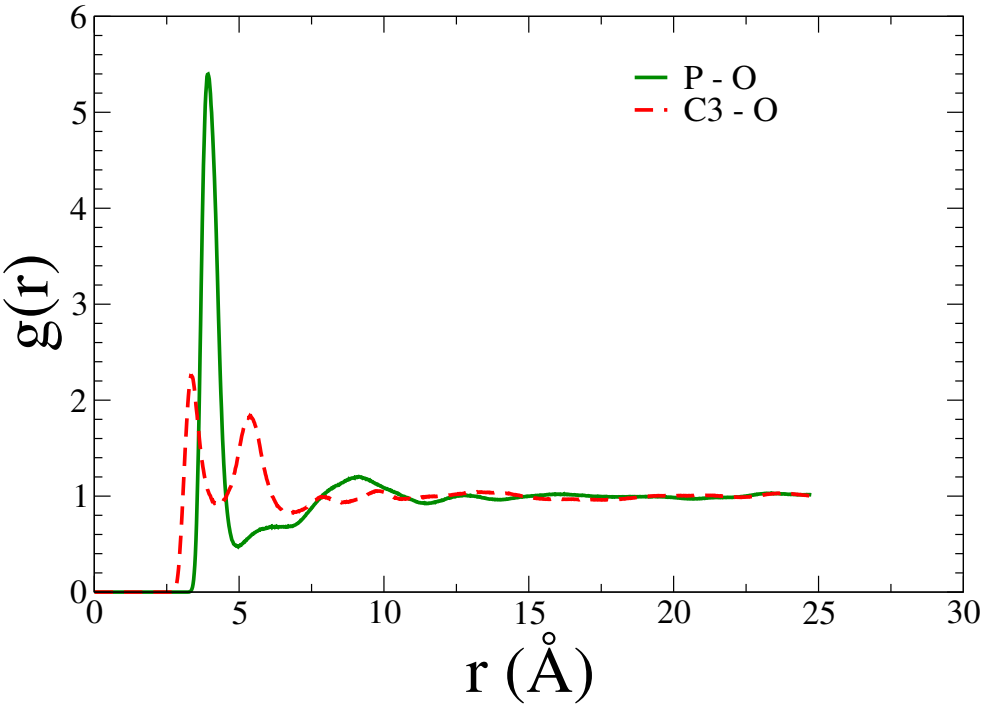

Note: Radial distribution function g(r) (green) between the P atom in the anion and the oxygen atom in water, (Red) between C3 in the cation and the oxygen atom of water.

Figure 4.2: Radial distribution functions between ionic liquid and water

4.3.2 Dynamics

In order to elucidate the effect of water on the dynamics of $[C_6MIM^+][PF_6^-]$, we show in Fig. 4.3(a) the mean square displacement (MSD)of [PF6] at 300K in the presence and absence of water. Fig. 4.3(a) clearly shows the existence of three different regimes. At short times we have sub-picosecond ballistic behavior, followed by a very long (tens of nanoseconds) sub-diffusive cage regime. This time scale is where non-

Gaussian dynamics[60] is predominant and is also the typical time scale on which most relevant chemical and photo-chemically induced electronic processes which are discussed in the previous chapter take place in the liquid. Gaussian diffusion, where the slope in Fig. 4.3(a) is one, is only established after tens to hundreds of nanoseconds in the neat ionic liquid. It is important to emphasize that not all ionic liquids are the same. Imidazolium based ionic liquids with shorter alkyl tails display faster dynamics[126, 25]. The size of the anion also plays an important role in determining the time scale on which these systems show non-Gaussian dynamics. From Fig. 4.3(a) we can see that the transition from ballistic to the intermediate cage regime is very similar in the presence and absence of water, however, the diffusive regime is achieved faster when water is present. It is fair to say that water enhances or lubricates the translational motion of this ionic liquid. Figure 4.3(b) shows a logarithmic plot of the mean square displacement as a function of time for pure SPC water at 300K and SPC water in the ionic liquid. Clearly the behavior of water in the ionic liquid is very different from that in bulk water at 300K and is similar instead to that found in the super-cooled regime.

$$C(t) =< \vec{ij}(t_0).\vec{ij}(t) > \tag{4.6}$$

Further evidence of the lubricating action of water can be obtained by analyzing the rotational motion of the [C_6MIM^+] cation. Rotational diffusion is intimately related to viscosity. We have computed rotational correlation functions C(t) for the [C_6MIM^+] cation along three different body-fixed directions depicted in Fig. 4.4. As is

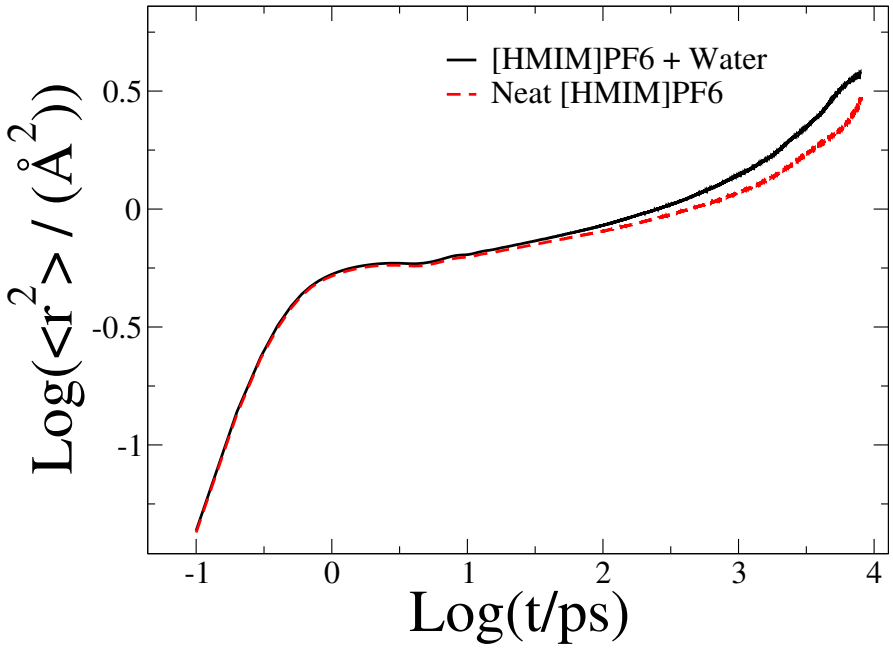

(a)

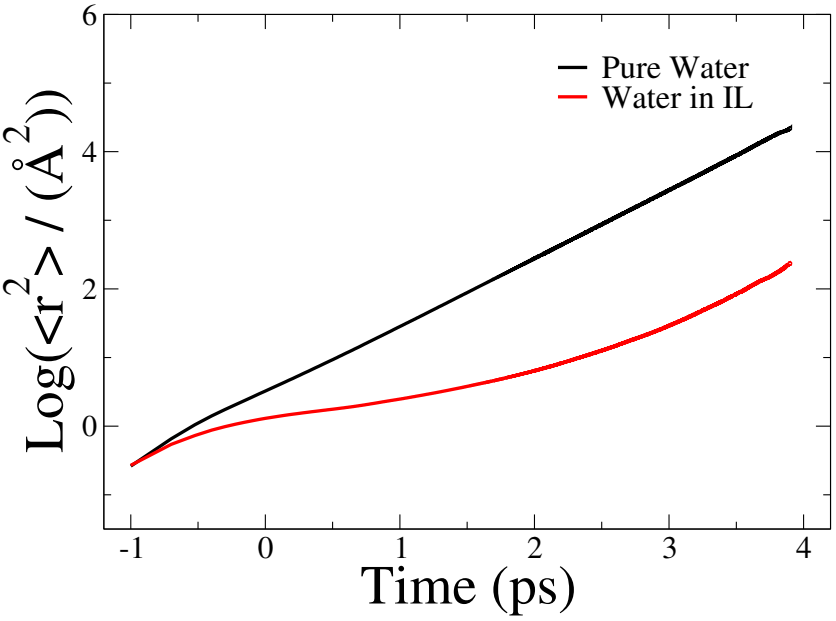

(b)

Note: Mean square displacement as a function of time for (a) PF6 in the neat IL (Red) and IL+Water (Black) (b) water in IL (red) and pure water (Black).

Figure 4.3: Mean square displacements of IL and water

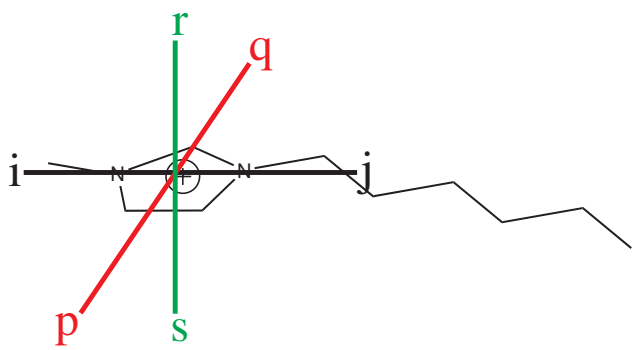

Note: Body fixed vectors used to compute rotational correlation functions

Figure 4.4: [C_6MIM^+] with body fixed vectors

to be expected, rotation of the i-j axis is slowest since it requires reorientation along the longest molecular axis. Figs. 4.5(a) show plots of these rotational correlation function in the case of the neat IL. It is really important to recognize that very little loss of correlation occurs on a 4 ns time scale. In other words on the time scale on which spectroscopy of typical fluorescent probes occur not much happens in terms of rotational dynamics in this particular ionic liquid. The effect of water on these correlation functions is noticeable and compatible with what we have observed in terms of translational diffusion. Figs 4.5(b), 4.5(c) and 4.5(d), compare rotational correlation functions in the presence and absence of water. In all cases, we observe a decay of correlations that is faster when water is present. It is clear now that the experimentally observed decrease in viscosity is a consequence of the enhancement in the translational and rotational dynamics caused by the presence of water. This phenomenon is non-negligible even though the volume or mass fraction of water is quite small (62 water molecules in a system of 303 [C_6MIM^+][PF_6^-] ions). Both anions

and cations are much larger than a single water molecule.

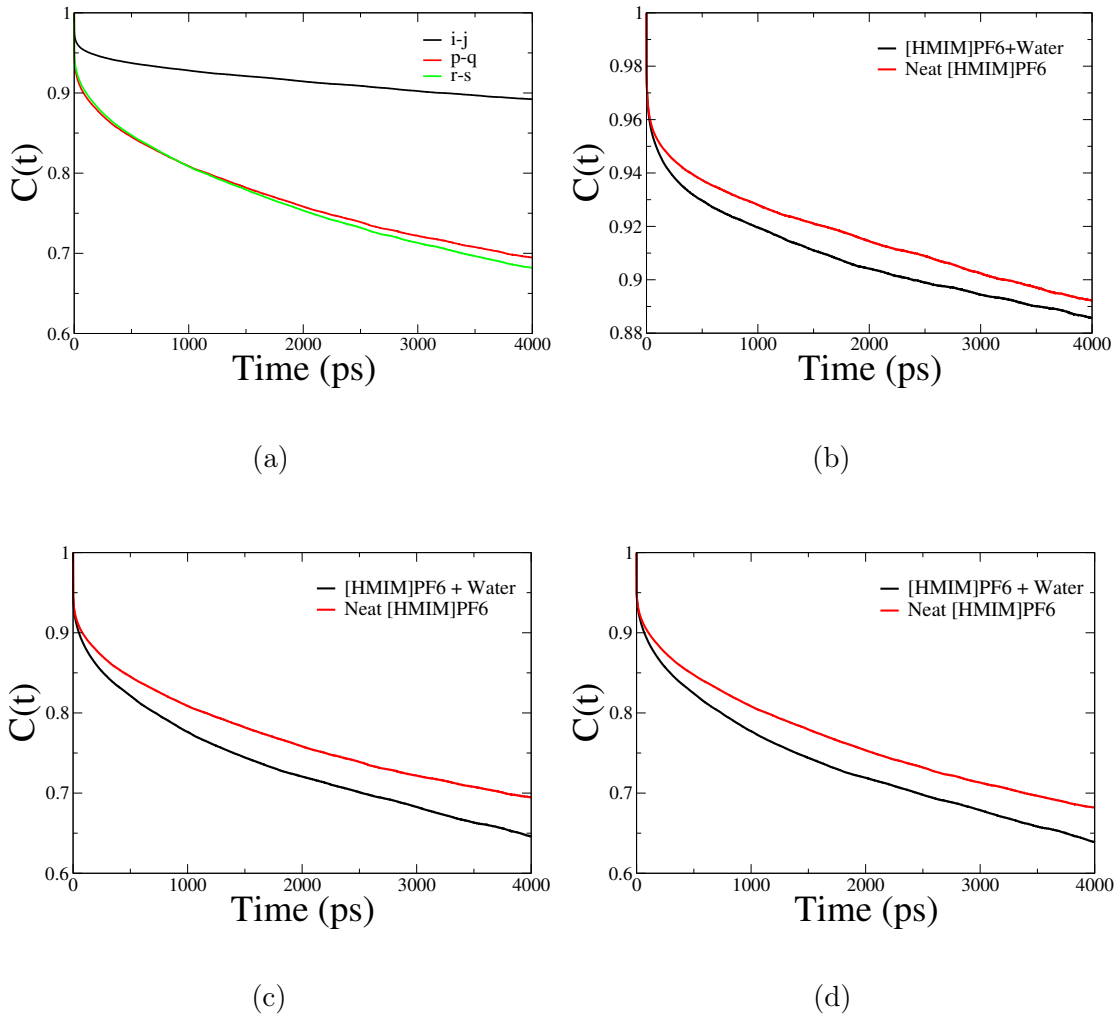

Note: Rotational correlation functions for the [C_6MIM^+] cation along the three directions defined in Fig. 4.4 (a) Neat-IL (b) ij axis (c) pq axis and (d) rs axis.

Figure 4.5: Rotational correlation functions for [C_6MIM^+]

A simple explanation is in place for these set of observations. Figure 4.6 displays a distribution of the coulombic interactions between cations and anions in the

presence and absence of water. These results are averages over 13 trajectories. It is obvious that these energies are higher in the absence of water. The screening effect is reflected in the higher translational and rotational mobility of the IL. Such lubricating effect of water is ultimately responsible for the decrease in viscosity observed experimentally [44, 24, 8, 118] and also in computer simulations [78].

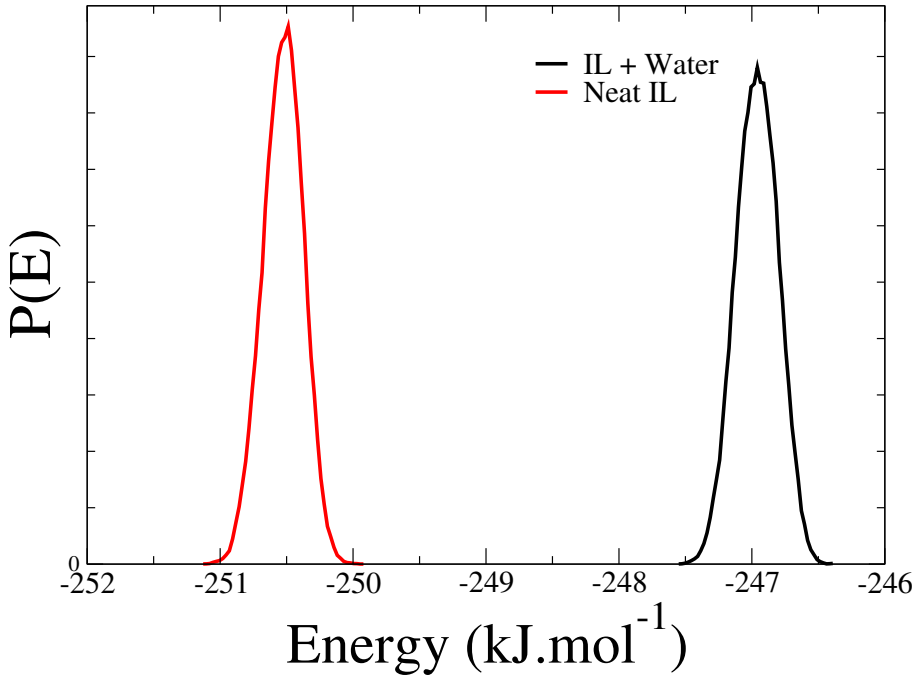

Note: Cation-anion coulombic interaction energies per ion pair averaged over 13 trajectories.

Figure 4.6: Coulombic interaction energies

4.3.3 Emission spectra of Coumarin 153 in Neat IL and IL+water systems

We presented in Chapter 3 through theoretical perspectives that ionic liq-

uids display relaxation dynamics following the photo-excitation of certain fluorescent probes that can induce absorption wavelength dependent fluorescence spectra. We also showed that this phenomenon can be exploited as a selectivity tool since the yield of photo-chemical reactions can be manipulated by adjusting the excitation wavelength. It is clear from Chapter 3 and also from the results of the emission spectra of Coumarin-153 presented in current chapter, that after fast initial energy relaxation upon photo-excitation, further relaxation of the solvent is very slow and full local environment interconversions often do not occur on a time scale that we are able to probe using computer simulations. This can be clearly seen from the fact that the solute-solvent energies after photo-excitation do not converge to a common average value if one analyzes trajectories with different initial conditions but otherwise with the same number of particles, average pressure and temperature.

Following the interesting work of Sarkar and coworkers[24] we have studied the effect of water on the fluorescence spectra of Coumarin-153 in $[C_6MIM^+][PF_6^-]$. Fig. 4.7 shows our ensemble averaged emission spectra for Coumarin-153 both in the neat IL and in the IL+water mixture corresponding to our maximum in absorption. It is clear that the emission spectrum is red shifted in the presence of water. Our results show the same trend experimentally observed by Sarkar and coworkers in reference[24] which is consistent with previous observations in other similar IL systems[23]. Analyzing our simulations we find that the red shift in the steady state emission spectrum appears to have two different origins. First the ensemble averaged ground to excited state energy difference at time zero is smaller in the presence of

water. Secondly the relaxation of the solvent surrounding the probe onto local energy minima is faster in the presence of water. This faster relaxation is clear from the time evolution of the emission spectra computed using equation 4.5 in the presence and absence of water. In Fig. 4.8(a) we see that the emission spectrum for coumarin-153 in the neat IL significantly shifts with time until at least 3000ps, whereas we do not see such slow relaxation in Fig. 4.8(b). Fig. 4.8(b) which displays the time dependence of the emission spectrum in the presence of water does not appear to significantly change after 300ps.

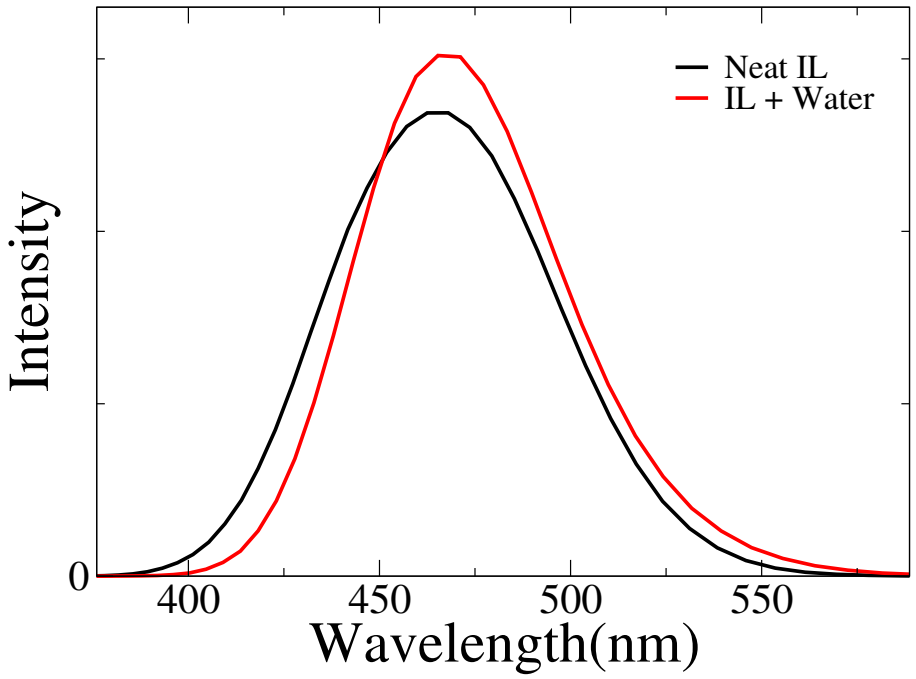

Note: Emission spectra of Coumarin-153 at 386nm in the neat IL and in the IL+water system. In the presence of water the emission spectrum is red-shifted

Figure 4.7: Emission spectra of Coumarin-153 in IL and IL+water systems

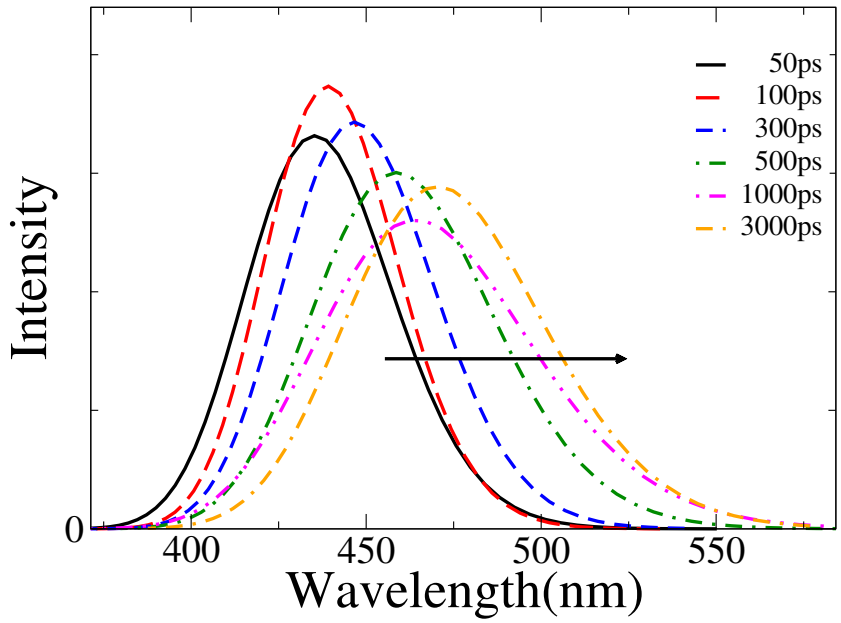

(a)

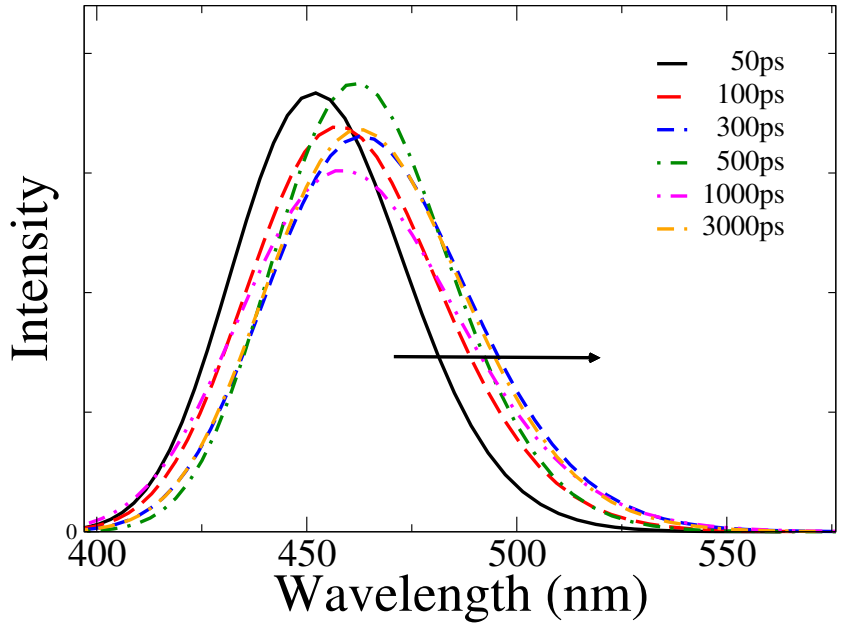

(b)

Note: Time evolution of the emission spectrum of coumarin-153 in (a) the neat IL and (b) in the IL+Water system

Figure 4.8: Time evolution of emission spectrum

Figures 4.9(a) and 4.9(b) show the excitation wavelength dependent emission spectra for Coumarin-153 in the presence and absence of water. These plots are similar to Figures 3.10 shown in chapter 3. Similar to the observations discussed in chapter 3, in both figures we can clearly see that coumarin-153 excited at different wavelengths gives rise to different emission spectra which are red-shifted as the excitation wavelength is increased. The same phenomenon is observed in the experiments of Sarkar and coworkers [24] and in a very similar system in reference [23]. As explained in previous chapter wavelength dependent emission spectra is common in ILs when the lifetime of the probe is shorter or of comparable magnitude to the time scale for solvent reorganization around the excited state probe [61, 63, 60].

One very important observation stemming from our results is that even though the solvent relaxation at the local environments level appears to be faster in the case when water is present, emission is still absorption wavelength dependent. This indicates that the fast relaxation observed is only partial and leads to local minima on a time scale compatible with the lifetime of Coumarin-153. Global solvent reorganization takes much more time at least longer than 10 nanoseconds. This is consistent with the dynamic Stokes shifts observation in experiments [24, 23, 25].

A different way to show that local relaxation is faster in the presence of small amounts of water is through the actual time history of the ground to excited state energy gaps after photo-excitation. Fig. 4.10 shows a plot of ΔE_{em}, the energy difference between ground and excited states after photo-excitation for a typical trajectory with and without water. Consistent with Fig. 4.8(a) and Fig. 4.8(b) we clearly see

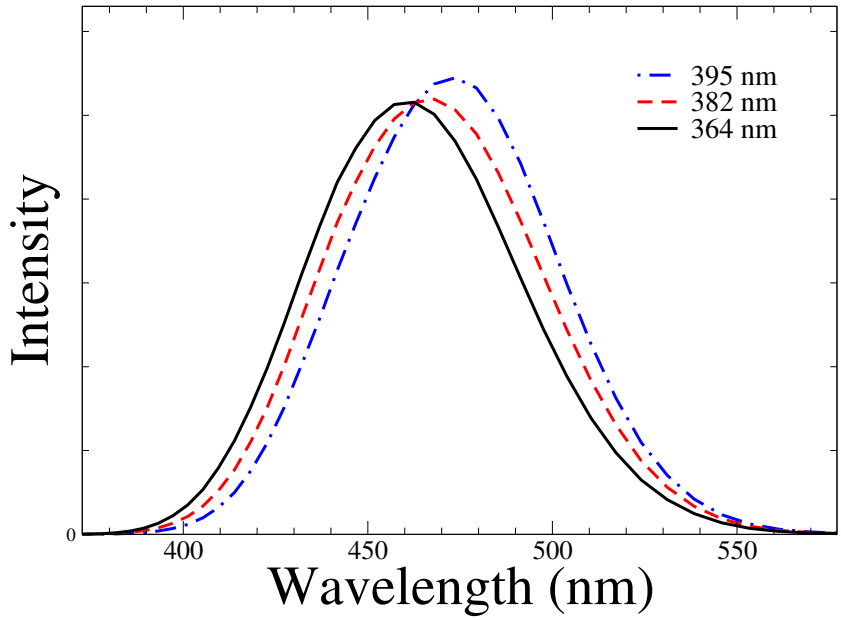

(a)

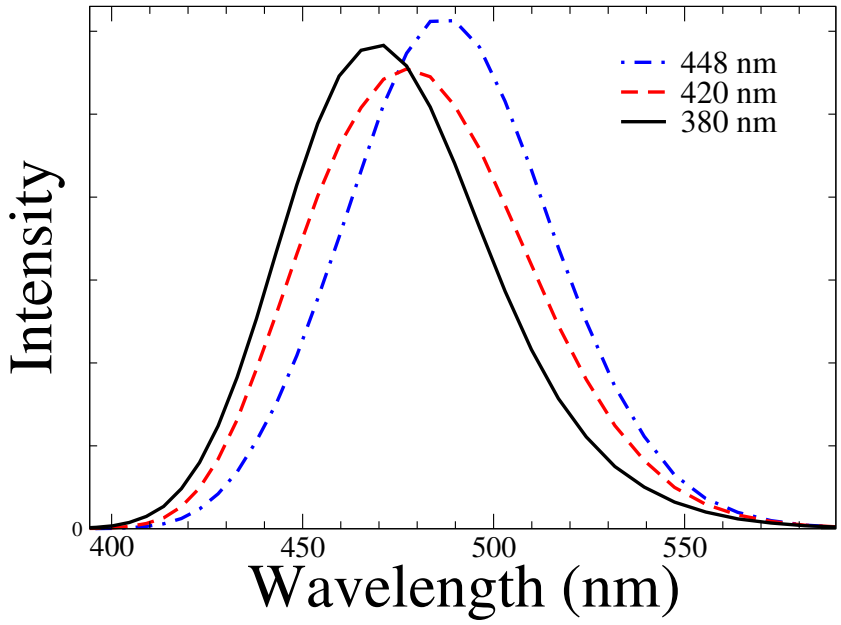

(b)

Figure 4.9: Emission spectra at different excitation energies (a) Neat-IL (b) IL+Water

that initial relaxation is faster when water is present. However, we emphasize that this is only local relaxation since the left panel in Fig. 4.11 shows that five arbitrarily chosen trajectories in which water is present have completely different steady state emission spectra. This can be compared with five trajectories in the absence of water Fig. 4.10 (right panel) in which the same phenomenon is observed. It is clear that if the solvent was able to visit all possible configurations that could solvate the excited state probe on the time scale of emission then all trajectories would yield identical emission spectra. This phenomenon is also discussed in previous chapter. Water indeed facilitates the mobility of the IL through a screening effect, but the dynamics leading to full relaxation of the solvent is still on a much longer time scale than the lifetime of the probe even in the presence of small amounts of water.

Not all ionic liquids are the same. Samanta and coworkers [112, 93] found that the phenomenon of excitation wavelength dependent emission is highly dependent on the probe molecule and the room temperature ionic liquid. In particular, they did not observe a red edge effect for coumarin-153 in $[C_4MIM^+][PF_6^-]$, $[C_2MIM^+][BF_4^-]$, and $[C_4MIM^+][BF_4^-]$. On the other hand both our simulations and the experiments in references [24, 23, 25] indicate the presence of an absorption wavelength dependent emission spectrum and Stokes Shift in the case of the same probe in a slower ionic liquid. Maroncelli and coworkers [70] also show a modest absorption wavelength dependence in the emission spectrum of Coumarin-153 in a much less viscous solvent than the one we are using in our study. Two conditions must be satisfied for the observation of such a phenomenon; [112, 61, 60, 30] the presence of inhomogeneous

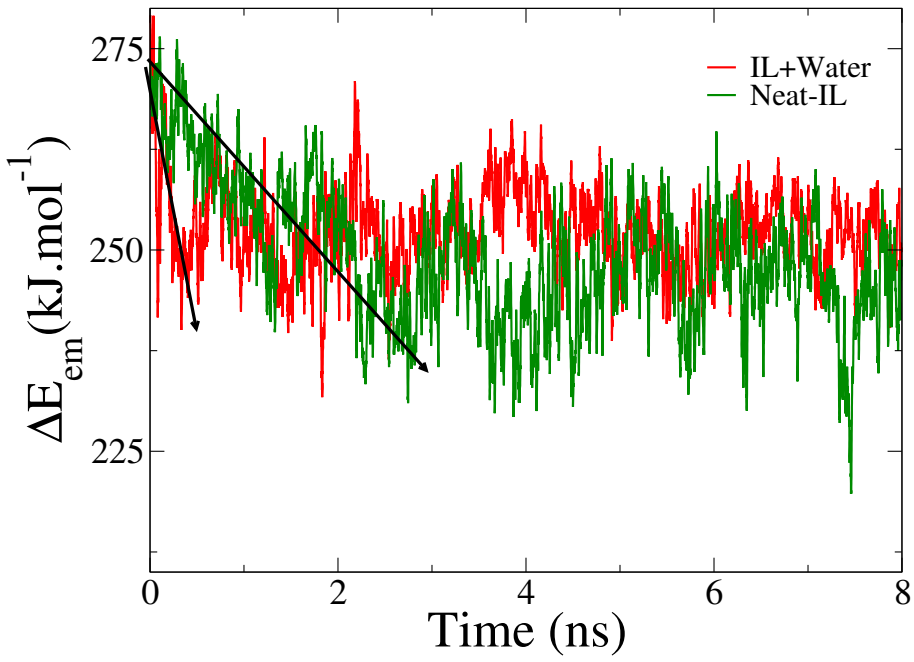

Note: ΔE_{em} as a function of time for two arbitrarily choosen trajectories (IL+Water-Red and Neat-IL-Green)

Figure 4.10: ΔE_{em} vs Time

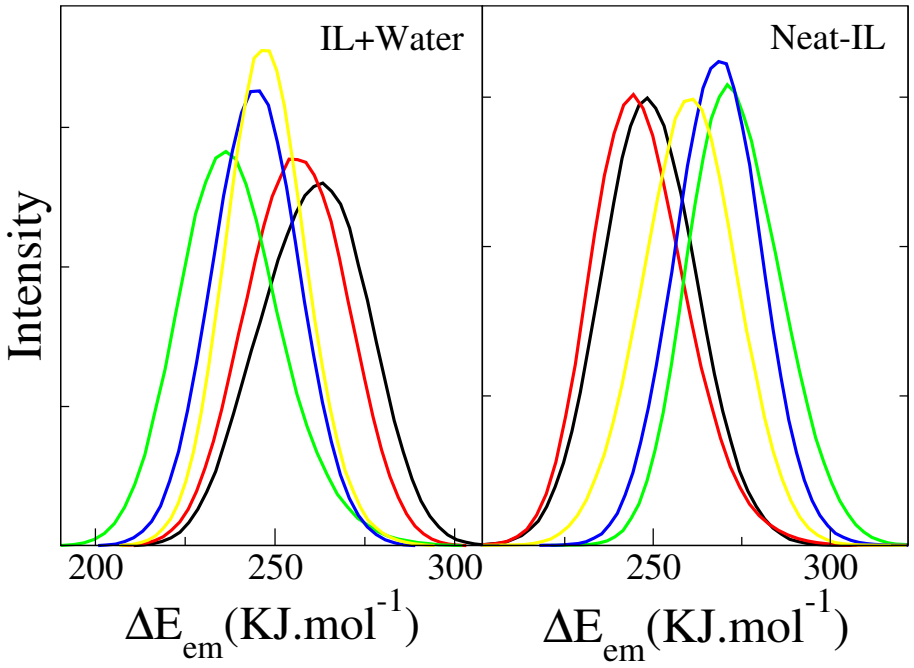

Note: Emission spectra for five independent trajectories IL+Water (left), neat IL (right)

Figure 4.11: Emission sepctra from different trajectories

broadening in the absorption spectrum (quite common in many solvents) and the solvation time scale must be slower than the fluorescence lifetime of the probe species. According to the second condition, only ionic liquids with solvation times that are rather long (the lifetime of Coumarin-153 is 4.85 ns in the neat $[C_6MIM^+][PF_6^-]$ [24]) will show a considerable red edge effect. Since the solvation times of $[C_4MIM^+][PF_6^-]$, $[C_2MIM^+][BF_4^-]$, and $[C_4MIM^+][BF_4^-]$ estimated from dynamic Stokes shift experiments are usually less than 2 ns [112, 74] it is obvious that if present at all, the importance of the red edge effect will be small in such liquids.

4.4 Conclusion

In this chapter we analyzed the role that water plays at small concentrations in the dynamics of $[C_6MIM^+][PF_6^-]$ as well as in the fluorescence spectroscopy of Coumarin-153 dissolved in this ionic liquid. We find that water screens the direct coulombic interactions between cations and anions and that it facilitates rotational and translational motion. Consistent with these observations, we also find that relaxation of solvent environments to local minima is considerably faster in the presence of small amounts of water.

In chapters 4 and 3 we discussed the slow and heterogenous dynamics of ionic liquids. We also established that this nature of ionic liquids would result in persistent local environments on time scales of several nanoseconds. These local environments not only exhibit heterogeneity in dynamics but also in structure. In order to connect these kinetic phenomena with liquid structure we will need to determine what struc-

tures are present for various ionic liquids. In the next two chapters we discuss the structural aspects of two different classes of ionic liquids.

CHAPTER 5
TEMPERATURE DEPENDENT STRUCTURE OF METHYLTRIBUTYLAMMONIUM BIS(TRIFLUORO METHYLSULFONYL)AMIDE

5.1 Introduction

The microscopic structure of ionic liquids is a subject of great current interest and intense debate. Neither our current understanding of the structure of highly symmetrical molten salts[127] nor that of neutral binary solvent mixtures can be extrapolated to adequately describe the intricacy of these systems. The complexity in the measured and calculated structure function $S(q)$ arises primarily from the intrinsic geometric anisotropy and amphiphilic nature of the ions. The structure function that we refer to in this thesis can be obtained by subtracting one from commonly known experimental structure factor.

In this chapter, the liquid structure of methyltributylammonium bis(trifluoro methylsulfonyl) amide ($N_{1444}{}^{+}/NTf_2{}^{-}$, see structure in Fig. 5.1) is characterized over a range of temperature from below glass transition temperature (T_g) to above melting point (T_m) using X-ray scattering experiments and computer simulations. The X-ray scattering experiments are performed by Prof. Castner's research group at RUTGERS and simulation studies are performed by our group.

The reason for studying this 145 K range of temperatures is that this liquid displays complex thermal behavior. In addition to being a fragile glass-former, it can also exist in a persistent, deeply super-cooled state for temperatures below the value

of $T_{\mathrm{m}} = 300$ K. Further, differential scanning calorimetry (DSC) results show phase transitions implicating two other solid phases with transition temperatures between T_{g} and T_{m}[42, 20].

Different types of x ray scattering experiments are performed: temperature-scanned dual-detector small- and wide-angle x ray scattering (SAXS-WAXS) and wide-angle high-energy x ray scattering (WAXS) at fixed-temperatures. The latter is used to obtain high quality values for $S(q)$. A primary goal of this work is to compare structure functions for $N_{1444}{}^{+}/NTf_2{}^{-}$ obtained from x ray scattering with those from MD simulations.

A number of structural studies of ionic liquids have been done using both theoretical[131, 29, 119, 116, 99, 115, 11, 117] and experimental methods.[13, 52, 55, 7, 53, 41, 39, 40, 73, 38] Structures of the molten salts have long been known to present charge-ordering[127]; this behavior is also observed in ionic liquids[131, 29, 119, 116, 99, 115, 11, 117]. Much insight into the experimental structure function $S(q)$ is gleaned by theoretically partitioning the computed structure functions into inter- and intramolecular terms with careful attention paid to the cationic, anionic and cross ionic contributions. Our temperature-dependent results permit a detailed analysis of the changes in liquid structure from the glassy state at 185 K to the liquid state at 330 K.

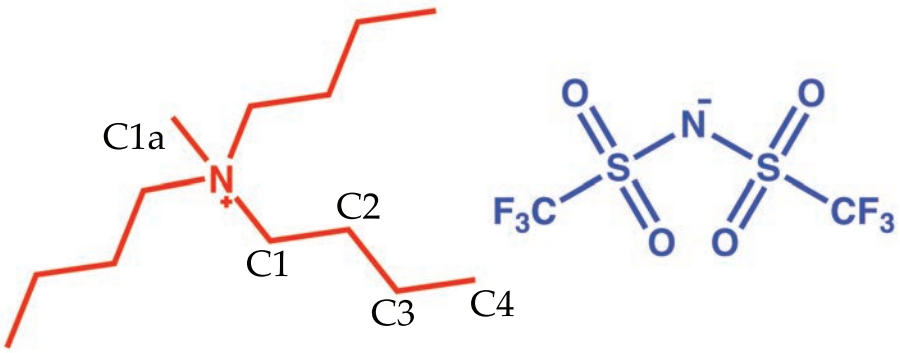

Note: Structure of methyltributylammonium (N_{1444}^+, red) and bis(trifluoromethylsulfonyl)amide (NTf_2^-, blue).

Figure 5.1: Structure of [N_{1444}^+], [NTf_2^-]

5.2 Simulations and Methods

All molecular dynamics simulations consisted of 256 ion pairs. A cubic simulation box was thoroughly equilibrated for more than 5 ns by lowering and raising the value of partial charges and by raising and lowering the temperature of the system until the volume and the structure were deemed converged. This equilibration was carried out in the NPT ensemble (constant number of particles, pressure and temperature) using the Berendsen algorithm and the Leap-Frog integration algorithm as implemented in GROMACS[56, 133]. Cutoffs for the Lennard-Jones and real space part of the Coulombic interactions were set to 15 Å. For dealing with long range electrostatic interactions, we used the Particle Mesh Ewald (PME) algorithm with an interpolation order of 6 and 0.08 nm of FFT grid spacing. Once the system was properly equilibrated we collected data for structural analysis from the final 1 ns of simulation with a frequency of 0.1 ps. The final box size was 5.4 nm, therefore, $S(q)$

could be determined for values of q down to 0.24 Å^{-1}($q = \frac{2\pi}{r}$ and $r = \frac{1}{2} \times boxlength$).

In this study, energy parameters for the anions are those derived by Lopes and Pádua [87]. We used the OPLS-AA force field[72] for the cations, except that charges were recomputed from an ab initio ESP-fit at the Hartree-Fock (HF)/6-31G* level of theory using the Merz-Kollman algorithm implemented in the Gaussian03 program suite[36]. Details on the exact potential used are reported in Appendix B.

5.2.1 Structure Function

The total x-ray static structure function can be computed from simulation results using Eq. 5.1.

$$S(q) = \frac{\rho_o \sum_i \sum_j x_i \, x_j \, f_i(q) f_j(q) \int_0^\infty 4\pi r^2 (g_{ij}(r) - 1) \frac{\sin qr}{qr} dr}{\left[\sum_i x_i f_i(q) \right]^2} \tag{5.1}$$

Here, $g_{ij}(r)$ corresponds to the partial radial pair distribution function (RDF) for atomic species of type i and j. Specifically, the indices i and j span the set of constituent atoms that includes C, H, N, O, F and S. x_i and x_j are the fractions of atoms of type i and j, $f_i(q)$ and $f_j(q)$ are the x-ray atomic form factors[104]. X-ray atomic form factors are calculated using the Eq. 5.2

$$f(\frac{sin\theta}{\lambda}) = \sum_i^4 a_i \, exp(-b_i \, \frac{sin^2\theta}{\lambda^2}) + c \tag{5.2}$$

where 2θ is the scattering angle. The parameters a_i, b_i and c for each element are obtained from international tables of crystallography [104]. ρ_o is the total number density of the system. A detailed derivation of structure function can be found in

literature [51].

For interpreting experimental structure functions, it is useful to decompose $S(q)$ into its many atomic pair interaction components. Mathematically this is a complicated problem since many combinations of functions can give rise to the same $S(q)$. Computationally the problem is much simpler since one generates the individual pair structure functions first and $S(q)$ is obtained as a weighted sum over these pair components.

Much insight can be derived from choosing different computational partitions of the atomic contributions. The general algebra involved in carrying out such partitioning in reciprocal space is demonstrated in Eqs. 5.3-5.16. These equations are quite general and simple modifications to them can be used to obtain other kinds of splittings as needed.

We start by recognizing that some $g_{ij}(r)$ have concomitant contributions from cations and anions. This is because the cations and anions each contain both carbon and nitrogen atoms. We therefore partition $g_{ij}(r)$ into two self-self correlation and two cross correlation components as written in Eq. 5.3; the superscripts c and a denote contributions from atoms on cations and anions, respectively.

$$g_{ij}(r) = g_{ij}^{c-c}(r) + g_{ij}^{c-a}(r) + g_{ij}^{a-c}(r) + g_{ij}^{a-a}(r) \tag{5.3}$$

The self- and cross-terms in the partial pair distribution functions are given here as

$$
\begin{aligned}
g_{ij}^{c-c}(r) &= \frac{V}{N_i N_j} \sum_{i}^{N_i^c} \sum_{j}^{N_j^c} \frac{\delta(r_{ij} - r)}{\frac{4}{3}\pi((r+\delta r)^3 - r^3)} \\
g_{ij}^{c-a}(r) &= \frac{V}{N_i N_j} \sum_{i}^{N_i^c} \sum_{j}^{N_j^a} \frac{\delta(r_{ij} - r)}{\frac{4}{3}\pi((r+\delta r)^3 - r^3)} \\
g_{ij}^{a-c}(r) &= \frac{V}{N_i N_j} \sum_{i}^{N_i^a} \sum_{j}^{N_j^c} \frac{\delta(r_{ij} - r)}{\frac{4}{3}\pi((r+\delta r)^3 - r^3)} \\
g_{ij}^{a-a}(r) &= \frac{V}{N_i N_j} \sum_{i}^{N_i^a} \sum_{j}^{N_j^a} \frac{\delta(r_{ij} - r)}{\frac{4}{3}\pi((r+\delta r)^3 - r^3)}
\end{aligned}
\tag{5.4}
$$

where V is the volume, N_i is the total number of atoms of type i in the system and N_i^c, N_i^a are the total number of atoms of type i in cations and anions respectively. In a condensed phase system, these definitions lead to the following condition:

$$
\lim_{r\to\infty} g_{ij}^{c-c}(r) + \lim_{r\to\infty} g_{ij}^{c-a}(r) + \lim_{r\to\infty} g_{ij}^{a-c}(r) + \lim_{r\to\infty} g_{ij}^{a-a}(r) = 1. \tag{5.5}
$$

Explicitly,

$$
\begin{aligned}
\lim_{r\to\infty} g_{ij}^{c-c}(r) &= \frac{N_i^c \times N_j^c}{N_i \times N_j} \\
\lim_{r\to\infty} g_{ij}^{c-a}(r) &= \frac{N_i^c \times N_j^a}{N_i \times N_j} \\
\lim_{r\to\infty} g_{ij}^{a-c}(r) &= \frac{N_i^a \times N_j^c}{N_i \times N_j} \\
\lim_{r\to\infty} g_{ij}^{a-a}(r) &= \frac{N_i^a \times N_j^a}{N_i \times N_j}
\end{aligned}
\tag{5.6}
$$

By substituting Eq. 5.3 and Eq. 5.5 into Eq. 5.1 we obtain Eq. 5.7.

$$S(q) = \frac{\rho_o \sum_i \sum_j x_i\, x_j f_i(q) f_j(q)}{\left[\sum_i x_i f_i(q)\right]^2} \times \left\{ \begin{array}{l} \int_0^\infty 4\pi r^2 \frac{\sin qr}{qr} dr \left(g_{ij}^{c-c}(r) - \lim_{r\to\infty} g_{ij}^{c-c}(r) \right) \\ + \int_0^\infty 4\pi r^2 \frac{\sin qr}{qr} dr \left(g_{ij}^{c-a}(r) - \lim_{r\to\infty} g_{ij}^{c-a}(r) \right) \\ + \int_0^\infty 4\pi r^2 \frac{\sin qr}{qr} dr \left(g_{ij}^{a-c}(r) - \lim_{r\to\infty} g_{ij}^{a-c}(r) \right) \\ + \int_0^\infty 4\pi r^2 \frac{\sin qr}{qr} dr \left(g_{ij}^{a-a}(r) - \lim_{r\to\infty} g_{ij}^{a-a}(r) \right) \end{array} \right\} \tag{5.7}$$

Eq. 5.7 is quite useful since it suggests how to properly partition $S(q)$ into anionic, cationic and cross term contributions in reciprocal space. This partitioning is defined in Eqs. 5.8 and 5.9.

$$S^{c-c}(q) = \frac{\rho_o \sum_i \sum_j x_i\, x_j f_i(q) f_j(q)}{\left[\sum_i x_i f_i(q)\right]^2} \times \int_0^\infty 4\pi r^2 \frac{\sin qr}{qr} dr \left(g_{ij}^{c-c}(r) - \lim_{r\to\infty} g_{ij}^{c-c}(r) \right)$$

$$S^{a-a}(q) = \frac{\rho_o \sum_i \sum_j x_i\, x_j f_i(q) f_j(q)}{\left[\sum_i x_i f_i(q)\right]^2} \times \int_0^\infty 4\pi r^2 \frac{\sin qr}{qr} dr \left(g_{ij}^{a-a}(r) - \lim_{r\to\infty} g_{ij}^{a-a}(r) \right) \tag{5.8}$$

$$S^{c-a}(q)+S^{a-c}(q) = \frac{\rho_o \sum_i \sum_j x_i\, x_j f_i(q) f_j(q)}{\left[\sum_i x_i f_i(q)\right]^2} \times \left\{ \begin{array}{l} \int_0^\infty 4\pi r^2 \frac{\sin qr}{qr} dr \left(g_{ij}^{c-a}(r) - \lim_{r\to\infty} g_{ij}^{c-a}(r) \right) \\ + \int_0^\infty 4\pi r^2 \frac{\sin qr}{qr} dr \left(g_{ij}^{a-c}(r) - \lim_{r\to\infty} g_{ij}^{a-c}(r) \right) \end{array} \right\} \tag{5.9}$$

For clarification, it is perhaps worth emphasizing that the two integrals below are not the same:

$$\int_0^\infty 4\pi r^2 \frac{\sin qr}{qr} dr \left(g_{ij}^{c-a}(r) - \lim_{r\to\infty} g_{ij}^{c-a}(r) \right) \neq \int_0^\infty 4\pi r^2 \frac{\sin qr}{qr} dr \left(g_{ij}^{a-c}(r) - \lim_{r\to\infty} g_{ij}^{a-c}(r) \right) \tag{5.10}$$

As an example g_{NC}^{c-a} is the partial pair distribution function of N atoms in the cations and C atoms in the anions, whereas g_{NC}^{a-c} is the partial pair distribution function of N atoms in the anions and C atoms in the cation.

Clearly, the total $S(q)$ can be written as

$$S(q) = S^{c-c}(q) + S^{c-a}(q) + S^{a-c}(q) + S^{a-a}(q). \tag{5.11}$$

In order to further separate intramolecular from intermolecular contributions in Eq. 5.8 we notice that

$$\begin{aligned} g_{ij}^{c-c}(r) &= g_{ij}^{c-c,intra}(r) + g_{ij}^{c-c,inter}(r) \\ g_{ij}^{a-a}(r) &= g_{ij}^{a-a,intra}(r) + g_{ij}^{a-a,inter}(r) \end{aligned} \tag{5.12}$$

where

$$\begin{aligned} g_{ij}^{c-c,intra}(r) &= \frac{V}{N_i N_j} \sum_i^{N_i^c} \sum_j^{N_j^{c,intra}} \frac{\delta(r_{ij} - r)}{\frac{4}{3}\pi((r+\delta r)^3 - r^3)}, \\ g_{ij}^{c-c,inter}(r) &= \frac{V}{N_i N_j} \sum_i^{N_i^c} \sum_j^{N_j^{c,inter}} \frac{\delta(r_{ij} - r)}{\frac{4}{3}\pi((r+\delta r)^3 - r^3)}. \end{aligned} \tag{5.13}$$

Anionic terms are defined analogously. It follows that

$$\begin{aligned} \lim_{r\to\infty} g_{ij}^{c-c,intra}(r) + \lim_{r\to\infty} g_{ij}^{c-c,inter}(r) &= \lim_{r\to\infty} g_{ij}^{c-c}(r) \\ \lim_{r\to\infty} g_{ij}^{a-a,intra}(r) + \lim_{r\to\infty} g_{ij}^{a-a,inter}(r) &= \lim_{r\to\infty} g_{ij}^{a-a}(r). \end{aligned} \tag{5.14}$$

Substituting these expressions in Eq. 5.8 we obtain

$$S^{c-c}(q) = S^{c-c,intra}(q) + S^{c-c,inter}(q)$$

$$S^{a-a}(q) = S^{a-a,intra}(q) + S^{a-a,inter}(q) \tag{5.15}$$

where

$$S^{c-c,intra}(q) = \frac{\rho_o \sum_i \sum_j x_i\, x_j f_i(q) f_j(q)}{\left[\sum_i x_i f_i(q)\right]^2} \int_0^\infty 4\pi r^2 \frac{\sin qr}{qr} dr \left(g_{ij}^{c-c,intra}(r) - \lim_{r\to\infty} g_{ij}^{c-c,intra}(r)\right)$$

$$S^{c-c,inter}(q) = \frac{\rho_o \sum_i \sum_j x_i\, x_j f_i(q) f_j(q)}{\left[\sum_i x_i f_i(q)\right]^2} \int_0^\infty 4\pi r^2 \frac{\sin qr}{qr} dr \left(g_{ij}^{c-c,inter}(r) - \lim_{r\to\infty} g_{ij}^{c-c,inter}(r)\right)$$

$$S^{a-a,intra}(q) = \frac{\rho_o \sum_i \sum_j x_i\, x_j f_i(q) f_j(q)}{\left[\sum_i x_i f_i(q)\right]^2} \int_0^\infty 4\pi r^2 \frac{\sin qr}{qr} dr \left(g_{ij}^{a-a,intra}(r) - \lim_{r\to\infty} g_{ij}^{a-a,intra}(r)\right)$$

$$S^{a-a,inter}(q) = \frac{\rho_o \sum_i \sum_j x_i\, x_j f_i(q) f_j(q)}{\left[\sum_i x_i f_i(q)\right]^2} \int_0^\infty 4\pi r^2 \frac{\sin qr}{qr} dr \left(g_{ij}^{a-a,inter}(r) - \lim_{r\to\infty} g_{ij}^{a-a,inter}(r)\right) \tag{5.16}$$

Terms in Eq. 5.9 do not require further partitioning since they are all intermolecular in nature.

Since we are interested in carrying out structural predictions as a function of temperature, it is important to verify that the chosen force field properly reproduces the experimental behavior of the density as a function of temperature. The computational results overestimate the experimental density with a systematic error of about 2.5 %. However, the overall slope of these two curves is almost identical. This gives us confidence that trends in $S(q)$ as a function of temperature that are solely due to density changes should be captured by our simulations.

5.3 Results and Discussion

5.3.1 Total structure factor

Computational and experimental x ray structure functions ($S(q)$), are shown in Fig. 5.2 in the q range from 0.4 to 17 Å^{-1}. The experimental structure functions were obtained from the raw scattering data using the PDFgetX2 program[105]. The structure functions from experiment are shown superposed with those calculated from the molecular simulations in Fig. 5.2. The positions of the measured and simulated peaks in $S(q)$ show quantitative agreement, though the amplitudes show a noticeable discrepancy, the agreement is still best at temperatures near ambient.

The structure functions shown in Fig. 5.2 were collected at six different temperatures. The scattering is dominated by two main peaks at lower q values and broader features beyond 2 Å^{-1}. Fig. 5.3 (top) emphasizes the q range from 0.4 to 2.0 Å^{-1}. The peak at the lowest q values in the $S(q)$ plot shifts from $q_{max} = 0.82$ Å^{-1} at 185 K to 0.78 Å^{-1} at 330 K, as shown in Fig. 5.3 (bottom). The next peak behaves similarly with q_{max} decreasing from 1.46 Å^{-1} at 185 K to 1.39 Å^{-1} at 330 K. We remind the reader that a range in q values corresponds to a larger range in distances as q gets smaller. Therefore it is not surprising that shifts are smaller for peaks at lower q. The scattering data from SAXS-WAXS measurements show a similar trend, with a shift in the peak positions to a lower q with increasing temperature. Although a shift in the positions of both diffraction peaks as a function of temperature is observed, it is clear that no abrupt transformation in the structure is noticeable between the glassy state at 185 K and the relatively high temperature liquid state at 330 K (and

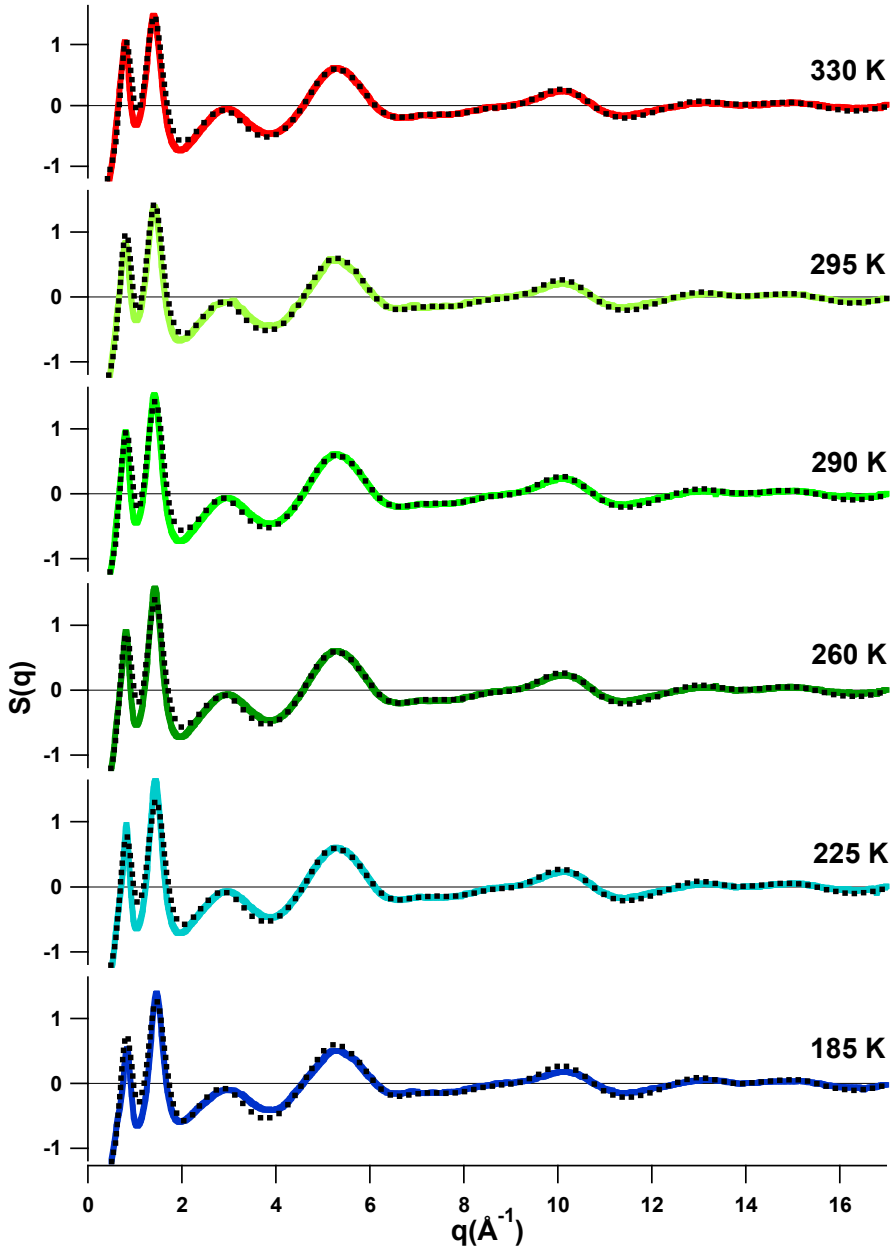

Note: The measured high energy x ray structure function $S(q)$ for $N_{1444}{}^{+}/NTf_2{}^{-}$ at six temperatures. Black dotted lines are total $S(q)$ functions calculated from MD simulations. For each temperature, the residuals of experiment vs. simulation are plotted above the $S(q)$ graph.

Figure 5.2: Total structure factor: Experiment and Simulation

up to 351 K for SAXS-WAXS measurements). Thus, these peak shifts are likely to be a simple consequence of density changes in a material. The scattering peaks observed in the range from 0.75 to 1.5 Å^{-1}, shown in Fig. 5.2 at 295 K are in good agreement with previous measurements by Pott and Méléard[101].

5.3.2 Analysis of the Structure Function

We used the partitioning schemes described in the methods section to define the ranges of q for which peaks in $S(q)$ can be identified as purely inter- or intramolecular. Fig. 5.4 (top) plots $S^{intra}(q) = (S^{c-c,intra}(q) + S^{a-a,intra}(q))$ superposed with $S(q)$. Clearly, for values of q greater than 3 Å^{-1}, all contributions to $S(q)$ are intramolecular. Fig. 5.4 (bottom) shows cationic and anionic contributions to $S^{intra}(q)$. From Fig. 5.4 (bottom) we conclude that the anionic contribution almost completely determines $S^{intra}(q)$. This is consistent with the fact that the structure function for $N_{1444}{}^{+}/NTf_2^{-}$ is qualitatively similar to that for other ILs containing the NTf_2^{-} anion[41, 40]. Since the average electron density per atom is much greater for the anion than for the cation, this should not be surprising.

The charge ordering typically observed in molten salts and in ionic liquids is manifested in Fig. 5.5. This figure shows the decomposition of the simulated $S(q)$ into cation-cation, anion-anion and anion-cation cross contributions. For clarity, the total $S(q)$ is shown with a vertical offset. All intermolecular structural features of $N_{1444}{}^{+}/NTf_2{}^{-}$ appear at values of $q \leq 3$ Å^{-1}. In this low q region, two prominent peaks can be observed at 0.81 Å^{-1} and 1.43 Å^{-1}.

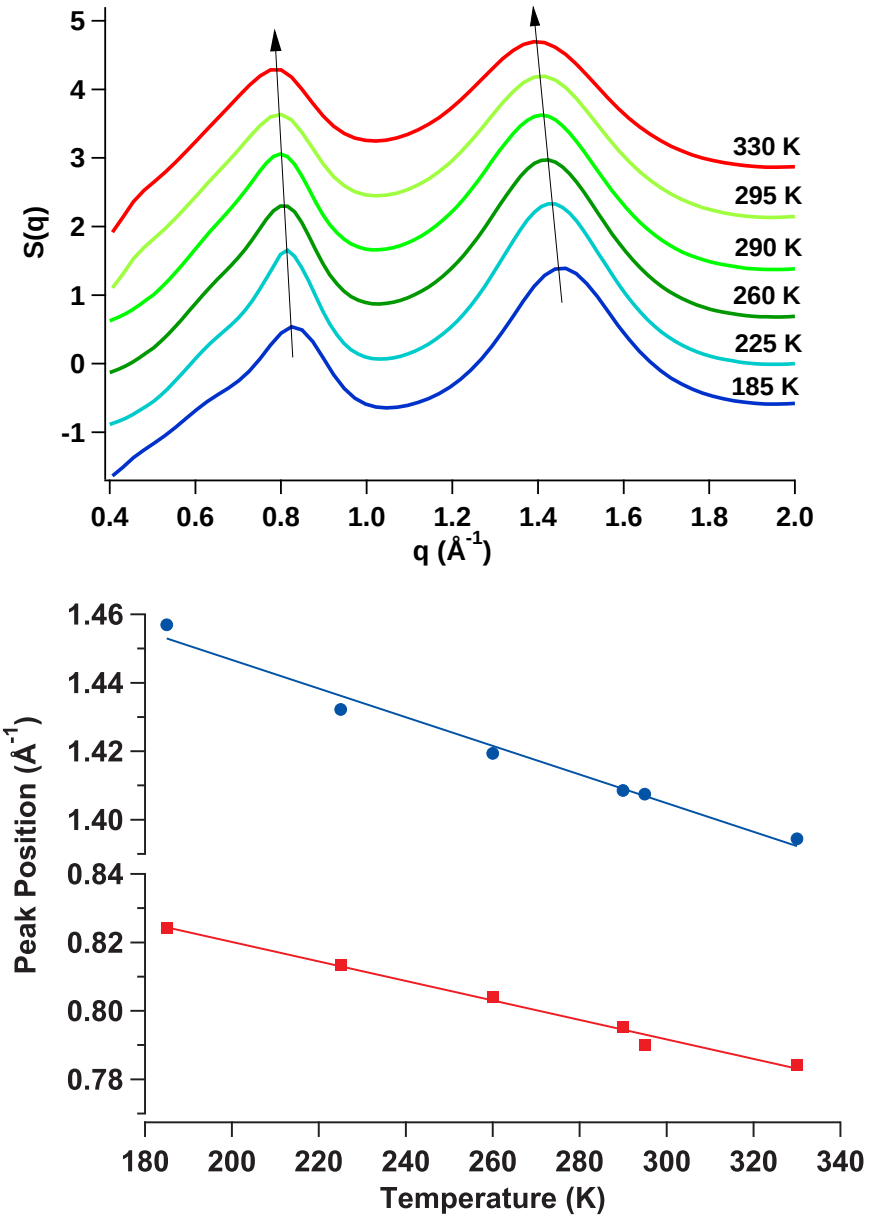

(top) $S(q)$ showing only the q range from 0.4 to 2.0 Å^{-1}. The black arrows are a guide to the shift in peak positions. Curves are offset by 0.7 units for clarity. (bottom) Temperature dependence of the positions of both diffraction peaks. Solid lines are linear fits to the data.

Figure 5.3: Peaks as function of temperature

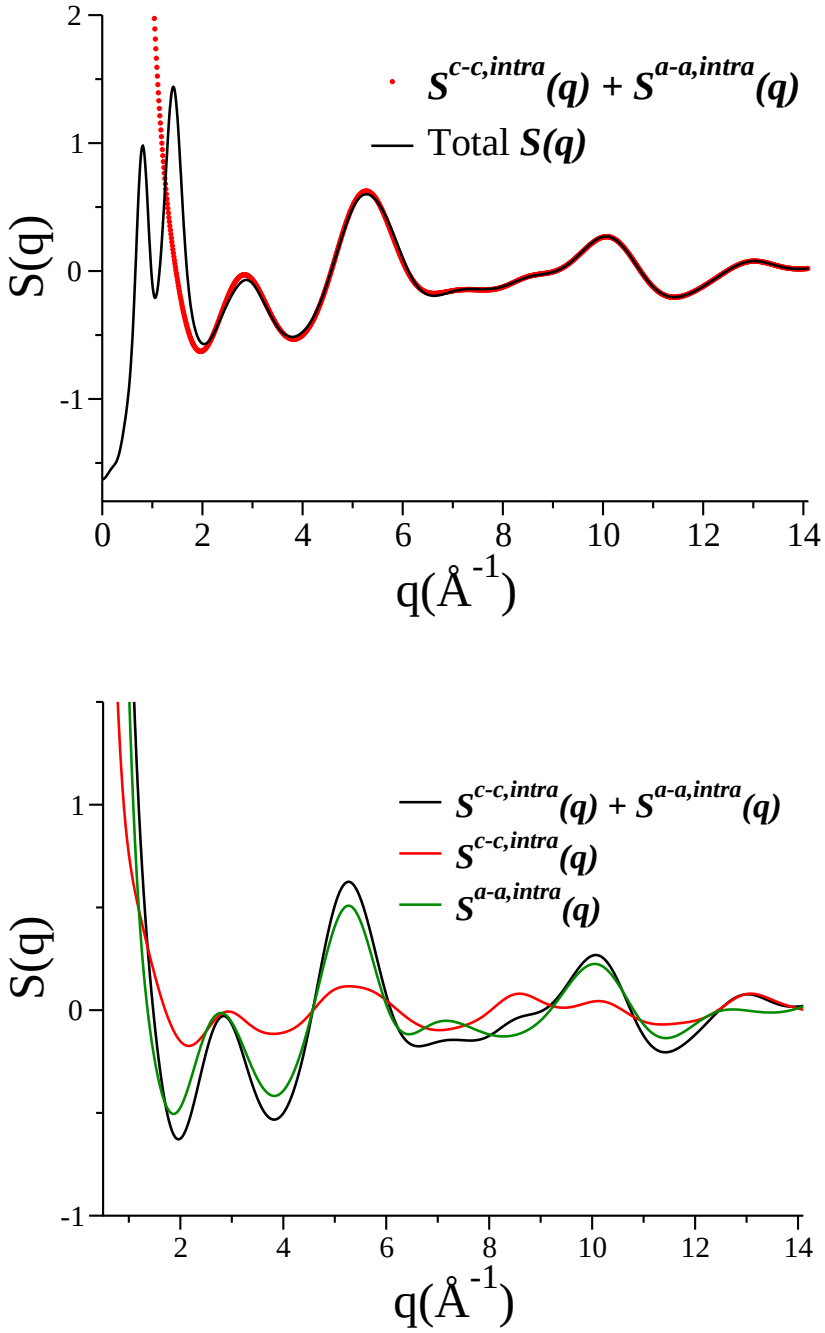

Note: (Top) Comparison between structure function $S(q)$ and intramolecular part of the structure function. (Bottom) Intramolecular part of the structure function compared with the cationic and anionic parts.

Figure 5.4: Intra and inter partial structure functions

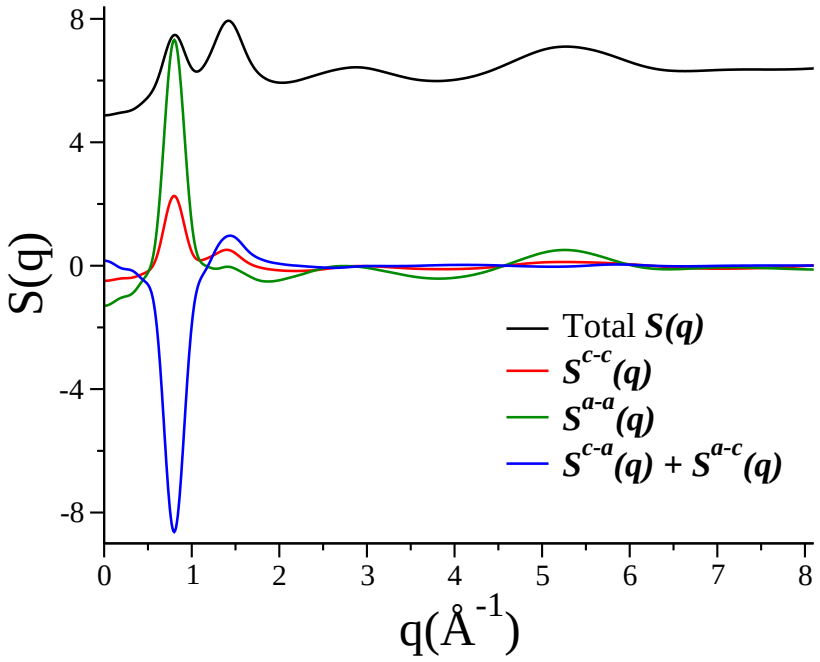

Note: Plots of partial and total $S(q)$ functions vs q. The total $S(q)$ is offset by 6.5 units.

Figure 5.5: Partial ion structure functions

Fig. 5.5 shows that positive contributions to the peak at 0.81 Å^{-1} arise from the cation-cation and anion-anion self-correlation terms. This means that this value of q corresponds to the characteristic inverse length at which the closest ions of the same charge occur in the liquid. Because of the differences in atomic form factors, the anionic contribution to this peak is significantly larger. Interestingly, a large and negative contribution at the same value of q can be observed from anion-cation cross correlations. This simply means that at the distance that one expects to find ions of the same charge one is unlikely to find ions of the opposite charge. In contrast, the peak in $S(q)$ at 1.43 Å^{-1} arises from a sum of contributions from several different intermolecular terms of close contact adjacent ions as well as intramolecular terms. We see in Fig. 5.6 that while minor intermolecular contributions arise from close contact ions of the same charge, intermolecular contributions to the peak at 1.43 Å^{-1} arise mainly due to ions of opposite charge that are nearest neighbors. For imidazolium based ionic liquids, we have observed the same type of out-of-phase behavior illustrated in Fig. 5.5 at around 0.9 Å^{-1}[3].

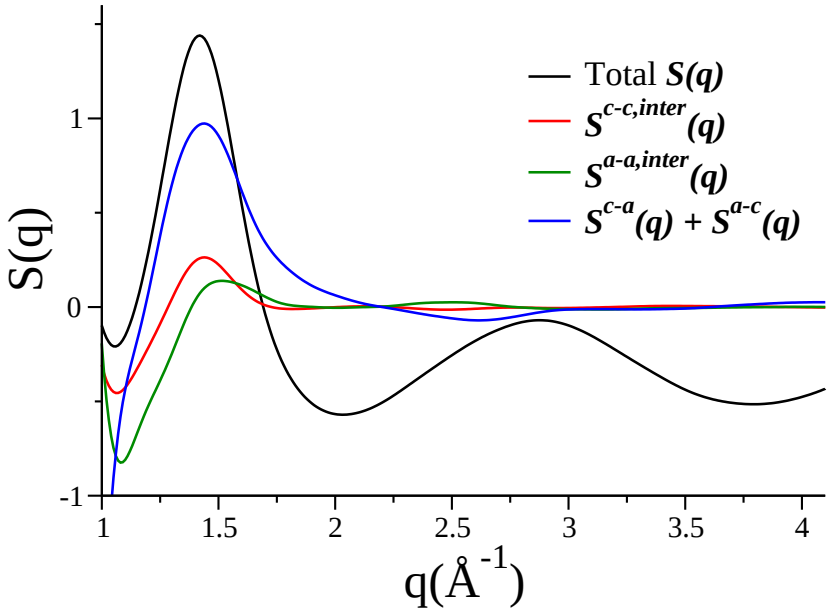

Note: $S^{c-c,inter}(q)$, $S^{a-a,inter}(q)$ and $S^{c-a}(q) + S^{a-c}(q)$ contributions to the peak at 1.43 Å^{-1} in $S(q)$.

Figure 5.6: Contributions to the peak at 1.43 Å^{-1}

5.3.3 Real Space Analysis

Since both the cation and anion of liquid N_{1444}^{+}/NTf_2^{-} are flexible, it is important to understand the effect that this conformational variability has on the overall structure of the liquid. Fig. 5.7 shows the anionic dihedral angle distribution in the liquid as a function of temperature. The Lopes and Pádua potential [88] predicts that the *trans* conformation is the most likely at all temperatures. At low temperatures, the probability for the *gauche* conformation increases slightly and a small probability appears at about 110 degrees for a conformation in between the *trans* and *gauche* forms. In Figure 5.8 we show the comparison of atomic pair distributions functions between N_{1444}^{+}cations and *gauche* and *trans* conformations of $[NTf_2^{-}]$anion. In Figure 5.9 we show the comparison of partial pair distributions functions for *gauche* and *trans* conformations of the NTf_2^{-} anion. The overall conclusion from these plots is that only very small changes in the intermolecular RDFs are observed when different anionic conformers are considered.

To better appreciate the three dimensional arrangement of ions in solution, we show in Fig. 5.10 the distribution of anion nitrogen atoms around a central cation and the distribution of cation nitrogen atoms around a central anion. We note that the cation and anion nitrogen atoms are unique and situated near the ion center of mass. Thus the nitrogen atoms serve as useful reference atoms for visualization purposes. This distribution was obtained by averaging over all cations (anions) from an equilibrated MD snapshot. If one considers the $[N_{1444}^{+}]$ cation as a tetrahedron with terminal methyl carbons at the vertices, the cationic nitrogen defining the origin

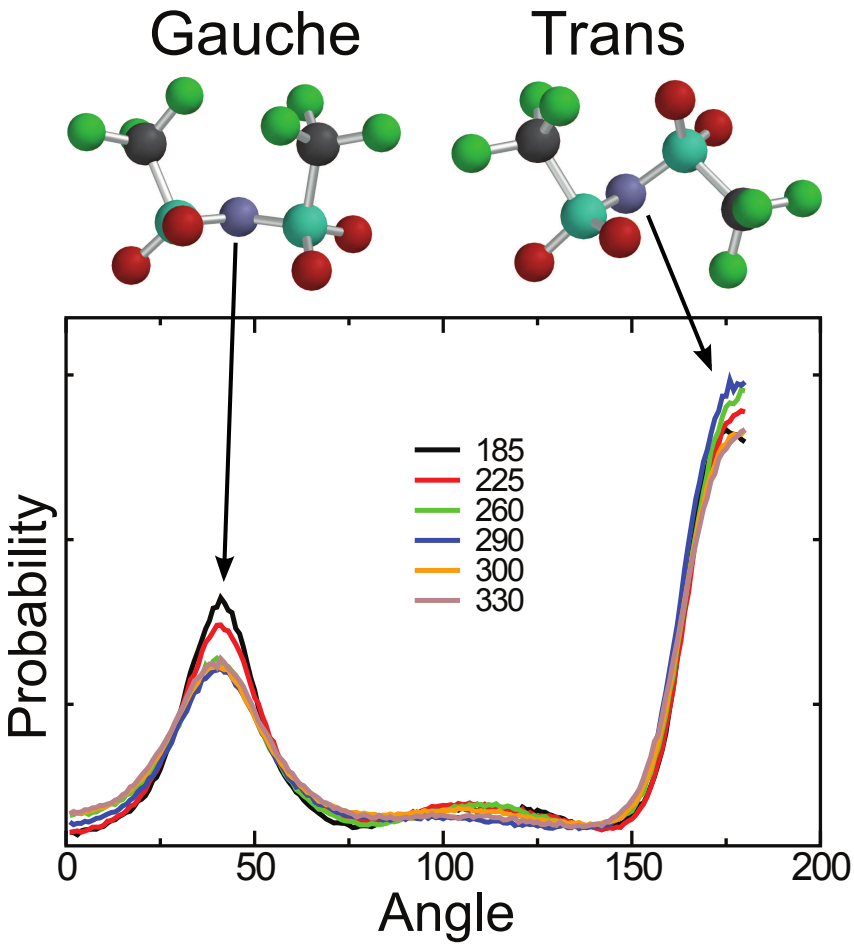

Figure 5.7: Normalized distribution of C-S-S-C dihedral angles for NTf_2^-.

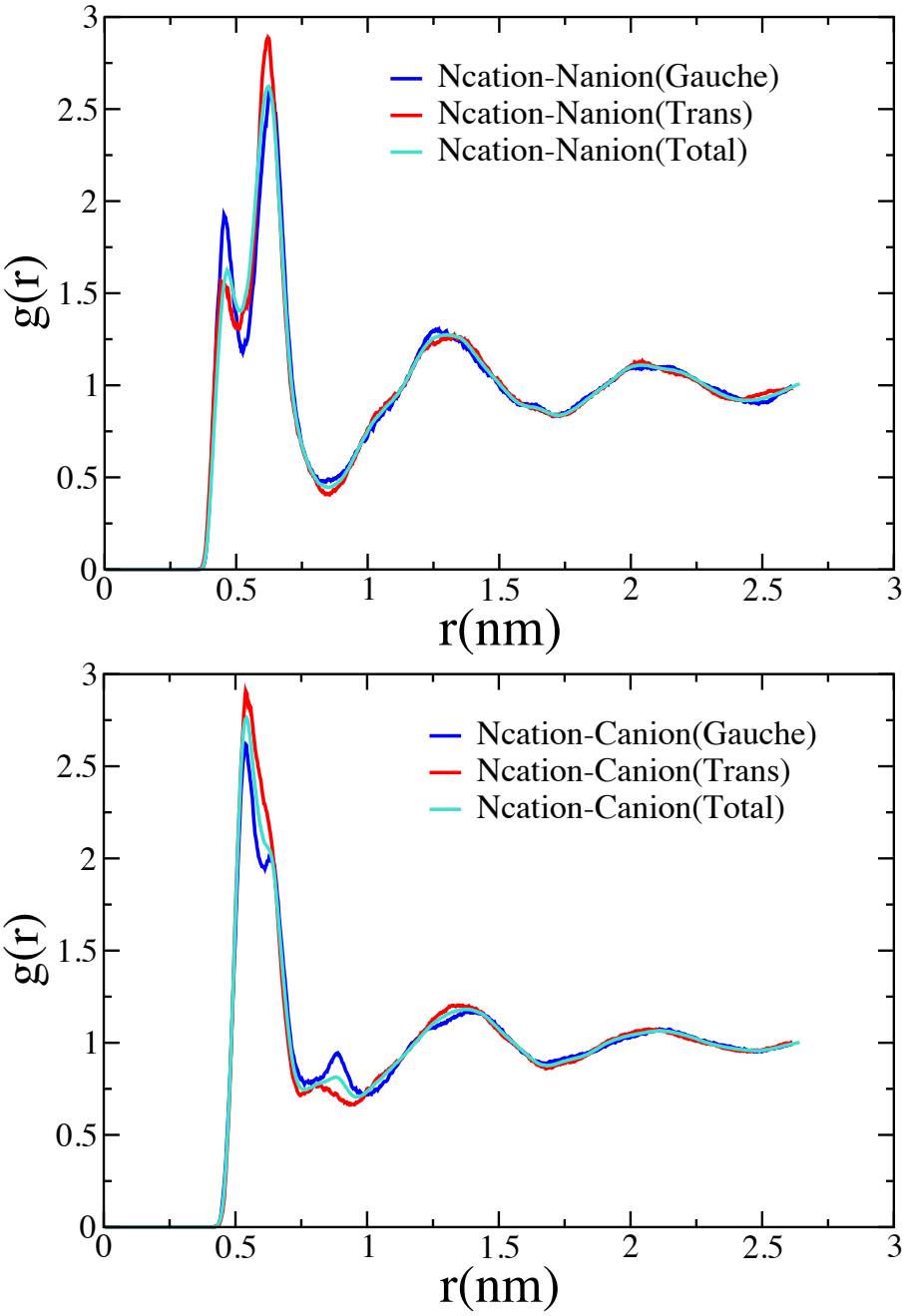

Note: Atomic radial distribution functions between (top) nitrogen of the cation and nitrogen of anion(bottom) nitrogen of cation and carbon of the anion.

Figure 5.8: Atomic RDFs of *trans* and *gauche* conformations

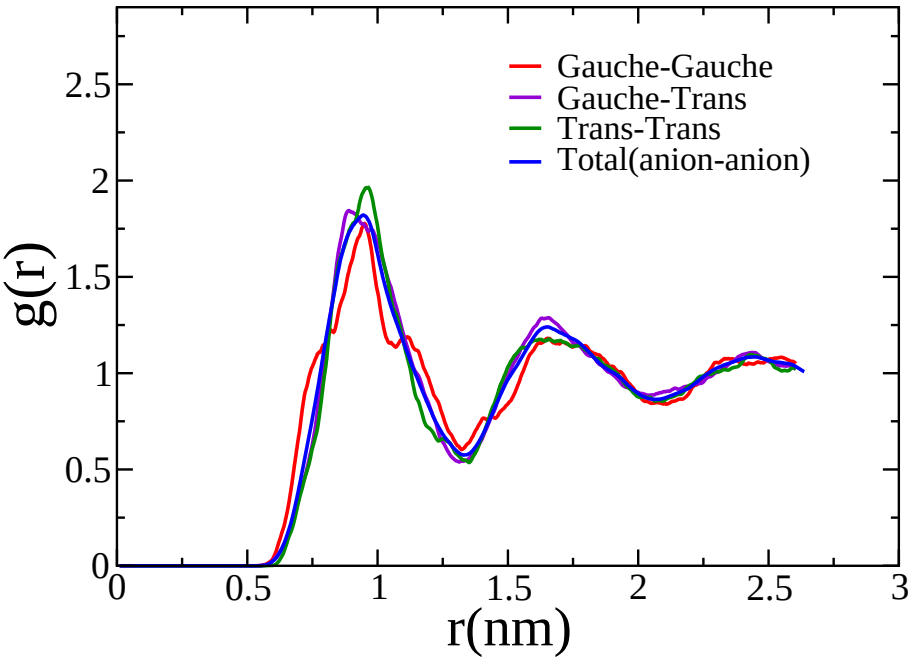

Note: Center of mass radial distribution functions for the *gauche* and *trans* conformations of the [NTf_2^-] anion.

Figure 5.9: Center of mass RDFs for *trans* and *gauche* conformations

in Cartesian coordinates and the positive Z axis along the line that joins the nitrogen and the methyl group, Fig. 5.10 (top) shows that the anionic N density forms an opposing tetrahedron with a single vertex along the negative Z axis and the other three vertices on the positive side of the Z axis bisecting the angles between the butyl groups. Fig. 5.10 (bottom) shows that if one considers the average conformational structure of NTf_2^- as a cylinder, cationic nitrogen density can be found forming a ring around this cylinder at the location of the anionic nitrogen.

A typical snapshot of the solvation environment of an individual $N_{1444}{}^+$ cation in this liquid is shown in Fig. 5.11. It is clear from this figure that significant variability in the intramolecular cationic conformation is present in the system. We have considered the distribution of cationic conformations and found that the [$N_{1444}{}^+$] cation can exist with many permutations of *trans* and *gauche* conformers of the butyl groups. If we focus on the dihedral angles defined by the four carbon atoms in each of the butyl tails, we find that at 300 K, approximately 45 % have only one butyl group in the *trans* conformation, 21 % have two butyl groups in the *trans* conformation and 0 % have three butyl groups in the *trans* conformation. These results are consistent with the Raman spectroscopy evidence for the existence of both *trans* and *gauche* conformers of the alkyl substituents on the cations for several 1-alkyl-3-methylimidazolium ionic liquids[48].

In a recent article, Pott and Méléard [101] attempted to rationalize the intermolecular features of their measured $S(q)$ for liquid $N_{1444}{}^+/NTf_2{}^-$, by speculating that the [$N_{1444}{}^+$] cations formed an interdigitated smectic A phase[101]. The charac-

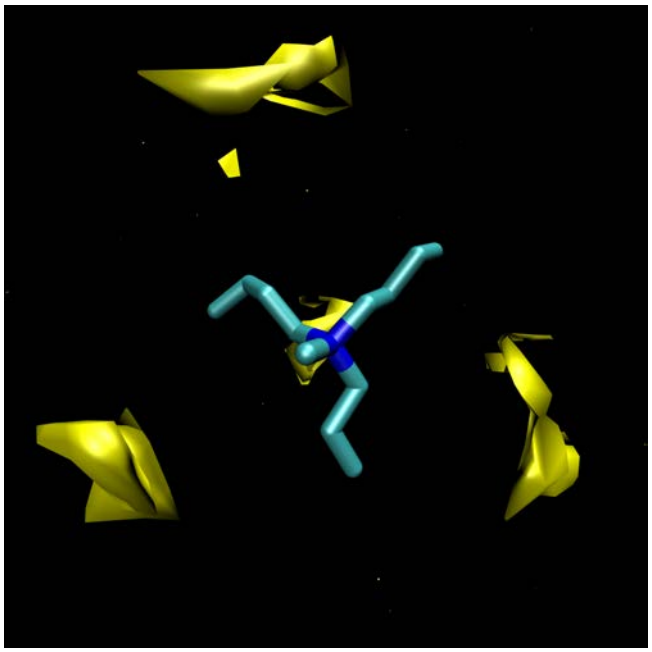

(a)

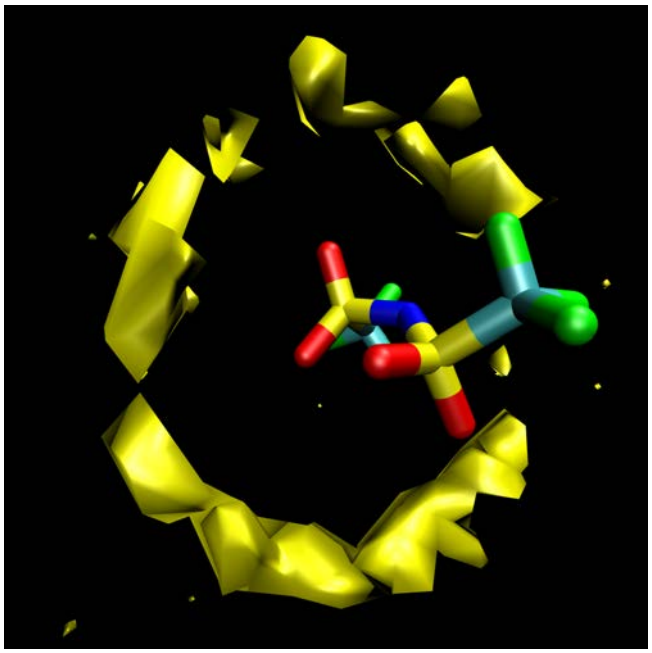

(b)

(a) Average anion nitrogen density distribution around a cation. (b) Average cation nitrogen density around an anion. Results are averaged over the 256 ions from the simulation at 300 K.

Figure 5.10: Spatial distribution functions

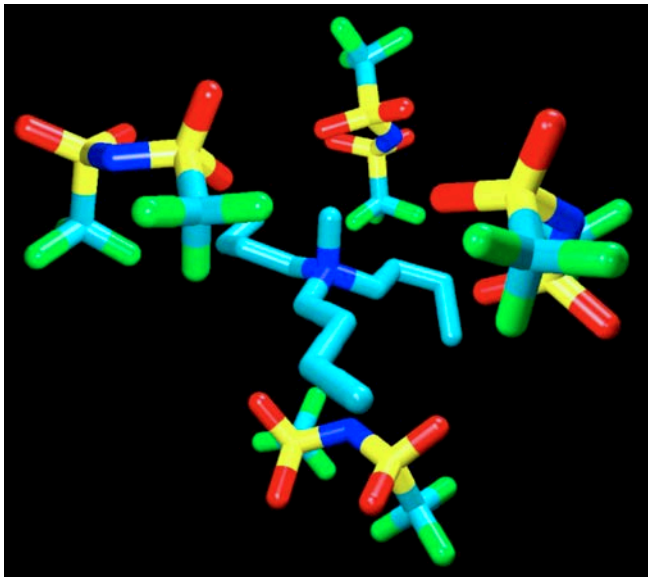

Note: Snapshot of a typical arrangement of anions around cation from the MD simulation at T = 300 K.

Figure 5.11: Typical Distribution of anions around a cation

teristic distances for this phase were assigned based on the peaks in their measured $S(q)$. In Fig. 5.12 we show the purely intermolecular radial pair distribution functions between each carbon atom in the butyl tails of [N_{1444}^{+}]. The results shown in Fig. 5.12 are not consistent with their speculation. The atom labels C1-C4 are defined in Fig. 5.1. The carbon atom of the terminal methyl group (C4) of each of the butyl chains has enhanced probability density at the contact distance for C4 atoms of adjacent cations. This is also true but to a lesser extent between C4-C3 pairs. On the contrary, the correlations between C4-C2 and C4-C1 pairs show decreased probabilities at contact distances. This is inconsistent with the interdigitation proposed by Pott and Méléard [101] because if interdigitation were present, then one should observe an enhancement of the probability at contact for C4-C1 and C4-C2 pairs.

The trend shown in Fig. 5.12 is exactly the opposite. Since our molecular dynamics simulations reproduce all features of the measured $S(q)$, we are confident that liquid $N_{1444}{}^{+}/NTf_2{}^{-}$ does not form an interdigitated smectic A phase of the type proposed.

No peaks in the structure function of $N_{1444}{}^{+}/NTf_2{}^{-}$ are observed for low values of q below the peak at 0.8 $Å^{-1}$. Despite speculations to the contrary[101], we find no evidence for any mesoscale ordering, smectic phases, or interdigitated alkyl chains in this particular ionic liquid. At the same time, it is important to recognize that smectic phases and interdigitated chains clearly do exist in other ionic systems with long alkyl chains[13] since these tend to form liquid crystals. It may well be that this is also the case for the long tail tetra-alkylammonium systems studied by Pott and coworkers.[101] First sharp diffraction peaks in the range $q < 0.5$ $Å^{-1}$ have been widely observed in the x ray[129, 109] or neutron structure functions[54] for a number of 1-alkyl-3-methylimidazolium ionic liquids. Caution is required when interpreting these low q peaks in $S(q)$ in terms of mesoscale structures such as smectic phases or interdigitated alkyl chains, as the amorphous charge-ordered structures of these liquids may be sufficient to explain the data.

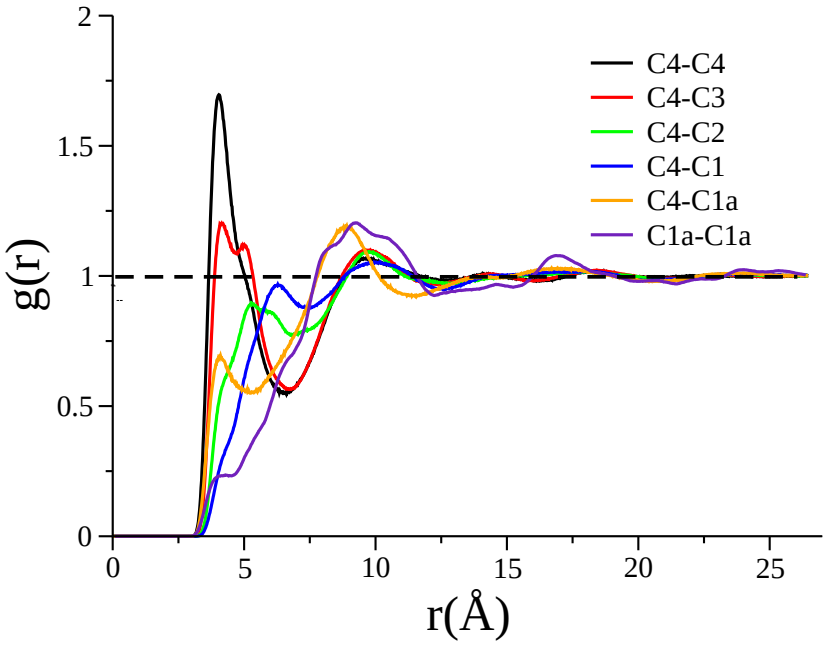

Note: Partial radial pair distribution functions between the cation carbon atoms. C1, C2, C3, C4, are the carbon atoms of the butyl chain. Numbering starts from the carbon atom next to the nitrogen, C1a is the N-methyl carbon. The atom labels for C1-C4 are defined in Fig. 5.1.

Figure 5.12: RDFs of carbon atoms in alkyl chains in cation

5.4 Conclusion

We have performed detailed experimental and computational analyses of the structure of N_{1444}^{+}/NTf_2^{-} over a 145 K range in temperature from the supercooled state to the high temperature liquid state. This system is interesting because while it shares common features in the low q range with other previously studied ionic liquids, it does not show a prepeak or first sharp diffraction peak for q values between 0.2-0.7 $Å^{-1}$. While the topic is still quite controversial, our current understanding of such prepeaks is that they appear to arise because of anisotropies in the ionic solvation environment. In chapter 6 we discuss this issue of prepeak and its geometric origin for the case of imidazolium based ionic liquids. While the anion is the main scatterer in this system, the organizing role of the cation is also very important. For example, In Chapter 6 we show that for the case of imidazolium ionic liquids with pseudo-spherical anions, there exists two types of polar neighbors surrounding a cation: those that are in close contact with its polar part (the imidazolium ring) and those that are separated from the ring because of the presence of a long alkyl tail[3]. This is consistent with recently published experimental and computational work by the Hardacre group[54]. We speculate based on Fig. 5.11 that such anisotropy is not significant in this system but one might expect it to arise if the alkyl tails of the cations were longer. Empirical evidence indicates that in many cases, liquids that show a prepeak in $S(q)$ also display a first sharp diffraction peak in the crystal state. Unfortunately a crystal structure is not yet available for the system studied here. One common feature that arises from this study and our analysis of other ionic liquids is the identity of the peak at around

0.81 $Å^{-1}$. As shown in Figs. 5.5 and 5.6, contributions from cation-cation and anion-anion terms are positive whereas cross-ion contributions are negative. This indicates that this is the spatial frequency corresponding to typical separations between ions of the same charge. Similar kind of charge ordering can also be noticed in Figure 6.11 of chapter 6 for case of imidazolium based ionic liquids. The prominent peak at 1.43 $Å^{-1}$ instead arises from close contact of ions having opposite charges. These two types of peaks are typical of ILs having the NTf_2^- anion and highlight the alternating ionic nature of the systems.

CHAPTER 6
STRUCTURAL FEATURES OF IMIDAZOLIUM BASED IONIC LIQUIDS

6.1 Introduction

In this chapter we explain the structure of imidazolium based ionic liquids with spherical or pseudo spherical anions. We put more emphasis on explaining the origin of the low frequency peak (often referred as pre-peak or first sharp diffraction peak) observed in the structure factor of the x-ray scattering experiments performed on imidazolium based ionic liquids.

The first sharp diffraction peak (FSDP) observed at low frequency in the x-ray and neutron scattering spectra of different imidazolium based room-temperature ionic liquids (the so called prepeak) has often been experimentally interpreted as indicative of mesoscopic organization leading to nanoscale segregation and the formation of domains of different morphologies. This interpretation which has permeated the analysis of many recently published articles deserves an in depth theoretical analysis. In this chapter, we use several different computational techniques to thoroughly dissect the atomistic components giving rise to the low frequency FSDP as well as other features in the structure function (S(q)).

Prepeaks or FSDPs are by no means peculiar or exclusive to RTILs, neither is the controversy on their geometrical origin. X-ray measurements and computer simulations show that common non-ionic liquids such as octanol also display a FSDP below 0.5Å^{-1} [27, 34, 132]. Whether these features carry relevant information about struc-

ture in the liquid phase has been a source of extensive debate in the glass/melt/non-crystalline solid community (for example see citations [47, 68, 103, 15, 97, 144, 122] and the many references therein).

In the case of RTILs, pioneering work by Bradley and coworkers[13] on long chain 1-alkyl-3-methylimidazolium ($[C_nMIM^+]$) systems, demonstrated the existence of low angle FSDPs in the crystalline and liquid crystalline phases that transformed into a broader low intensity peak upon melting (see Figure 2 in reference [13]). Early computational work by Urahata and Ribeiro[131] also predicted the occurrence of a prepeak in the $[Cl^-]$ component of the S(q) in their 1-alkyl-3-methylimidazolium systems. Urahata and coworkers carefully highlighted the standing controversy on the origin of these types of features in the high temperature ionic melt literature.

Insightful work by Wang and Voth[136, 138, 137], Bhargava *et. al.*[11] and Lopez and Padua[18, 43] directed the attention of the RTILs community[145, 22] to the interesting morphology of these systems as observed in computer simulations. It is clear from these author's early work that because of Coulomb interactions, imidazolium heads and anions associate, and longer cationic alkyl tails appear to aggregate. Approximately at the same time, some very interesting experiments by the group of Triolo[109, 129, 130] showed that the prepeak observed by Bradley and coworkers on imidazolium liquids with very long alkyl tails could also be detected in systems with cations possessing shorter tails. These experiments greatly enhanced our understanding of the systematic structural and dynamical changes in the prepeak to be expected as the length of the longest cationic alkyl tail is adjusted. In order to interpret the

observed structural dependency of the FSDP on alkyl tail length, different ideas have been proposed. These include cationic tail interdigitation or the formation of micelles (see for example figure 3 in reference[130]) which could account for the alkyl tail length dependence on the q value at which the prepeak shows in Triolo's SAXS experiments. This type of interpretation involving the notion of complex long range multi-cation correlations to form micelles, strands and other more complex morphologies even in the case of imidazolium systems of modest tail lengths such as $[C_5MIM^+]$ has become quite popular (see for example[28, 146]). However, recent work by Hardacre and coworkers[54] has suggested that the prepeak is a simple consequence of cationic anisotropy which imposes certain patterns of coordination along the direction of the longer alkyl tail and not due to complex long range morphologies. In this chapter we present our attempts to combine detailed computer simulations with evidence from published experimental data in order to clarify the geometrical origin of the prepeak in imidazolium based ILs with spherical or pseudo-spherical anions. In particular we will work with the $[C_6MIM^+][Cl^-]$, $[C_8MIM^+][PF_6^-]$ and $[C_{10}MIM^+][PF_6^-]$ ionic systems.

6.2 Simulations and Methods

All molecular dynamics (MD) simulations were carried out with the GROMACS package [56, 133]. We used OPLS-AA parameters[72] with partial charges derived from the work of Lopes and Padua [87]. For clarity in the exposition of ideas, much of the preliminary work we did trying to understand the prepeak dependence

on simulation box size is not shown. It is sufficient to say that if the box length is larger than $2 \times \frac{2\pi}{q_{prepeak}}$ there is a dependency on the intensity (but not the position) of the prepeak with box size. Boxes with sides smaller than this threshold value should never be used since obviously they will not display any prepeak. In practice, we find that 300 pairs of ions periodically replicated are adequate in order to properly account for all features in S(q) above 0.24Å^{-1} ; however some of our simulations consisted of up to 21,952 ion pairs in order to generate the most accurate possible reciprocal space structure function that we could afford.

All simulations involving $[C_6MIM^+][Cl^-]$ except for those in 6.3.4 were carried out with 21,952 ions pairs corresponding to 702,464 atoms. Simulations of $[C_8MIM^+][PF_6^-]$ were 2,744 ion pairs in size whereas in our study of melting of $[C_{10}MIM^+][PF_6^-]$ we used 576 ion pairs. Because of the larger computational cost involved in the multivariate global optimization procedure described in 6.3.4, this study was done with an equilibrated simulation box of 300 $[C_6MIM^+][Cl^-]$ ion pairs.

We equilibrated each of our systems for several nanoseconds using the same protocol as reported in previous chapters. The large system with 21,952 ions pairs was built by stacking a subsystem of 2744 equilibrated ion pairs and re-equilibrating for 800 ps. Equilibration and production runs were carried out in the NPT (constant number of particles, pressure, and temperature) ensemble using the Berendsen algorithm and the Leap-Frog integration scheme coded in GROMACS [56, 133]. Production runs for $[C_6MIM^+][Cl^-]$ and $[C_8MIM^+][PF_6^-]$ were performed at 300K and 1atm pressure. We used the PME (Particle Mesh Ewald) algorithm with interpolation

order 6 and 0.8 Å grid spacing for proper accounting of long range electrostatic interactions. Cutoffs for Lennard-Jones and real space part of the Coulombic interactions were set to 15 Å.

Melting of $[C_{10}MIM^+][PF_6^-]$ was simulated in a triclinic box of symmetry $P2_1/c$ by imposing a temperature ramp in the range 400K to 600K at 1atm on a time scale of 1ns. Subsequently the system was further simulated at 600K for 2ns.

All aspects of the global optimization procedure to enrich real space coordinates in the spatial frequencies of the prepeak are discussed in 6.3.4.

6.3 Results and Discussion

Imidazolium based systems with longer alkyl tails and with counterions that are spherically- or pseudo-spherically symmetric tend to show significant similarities in their intermolecular structure. This can be appreciated by comparing corresponding structure functions S(q) at inverse distances below $2Å^{-1}$. This is exemplified in Fig. 6.1 where we show computationally derived S(q) for $[C_6MIM^+][Cl^-]$, $[C_8MIM^+][PF_6^-]$ and $[C_{10}MIM^+][PF_6^-]$ in the liquid state. Features at q values larger than $2Å^{-1}$ are mostly intramolecular in nature.

Three main features below $2Å^{-1}$ are always observed. The prepeak, below $0.5Å^{-1}$, a shoulder at around $0.9Å^{-1}$ and a major peak at around $1.5Å^{-1}$. It turns out that for imidazolium based systems with these types of counterions, the FSDP and other intermolecular peaks present in the S(q) of the liquid are also often found in the simulated powder spectrum of the crystal (see for example[45]). It is therefore

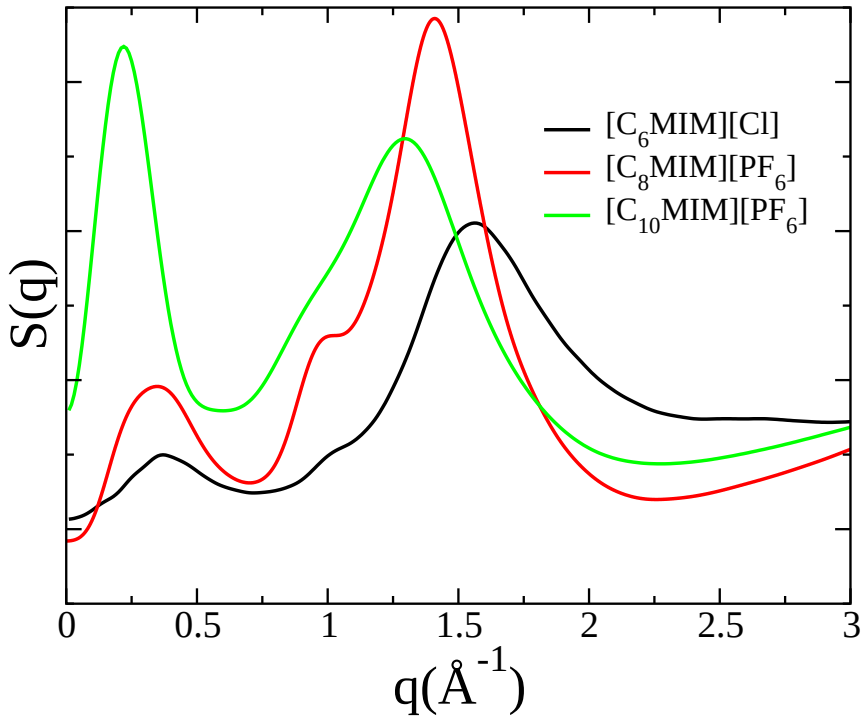

Note: S(q) for liquid $[C_6MIM^+][Cl^-]$ and $[C_8MIM^+][PF_6^-]$ at 300K and for $[C_{10}MIM^+][PF_6^-]$ at 600K from our computer simulations described in 6.2

Figure 6.1: Structure functions of $[C_6MIM^+][Cl^-]$ and $[C_8MIM^+][PF_6^-]$

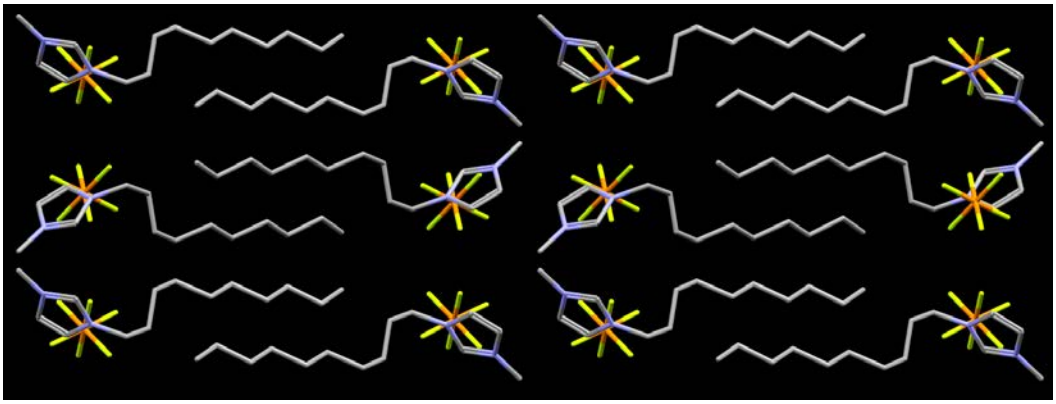

Crystal structure of $[C_{10}MIM^+][PF_6^-]$ (identifier ODOLOJ) from reference[45] plotted using the program Mercury[92]

Figure 6.2: Crystal structure of $[C_{10}MIM^+][PF_6^-]$

natural to approach the problem first from the perspective of the crystal since much insight can be gained from interpreting these features in terms of distances between Miller planes.

6.3.1 Structure factor of the Crystal

While imidazolium based ionic liquids are known to crystallize as different polymorphs[58, 67], a pattern of anions associated with cationic heads such as that in Fig. 6.2 is quite common[45].

The asymmetry caused by the longer cationic alkyl tail gives rise to packing patterns with characteristic short and long separations between neighboring polar groups.

From the perspective commonly used in computational theory of liquids, the

coherent x-ray intensity ($I_{coh}(q)$) is defined as[77]:

$$S(q) = \frac{I_{coh}(q) - \sum_i x_i f_i^2(q)}{(\sum_i x_i f_i(q))^2} \tag{6.1}$$

In (6.1), i labels an atom type and x_i, f_i are the corresponding atomic fraction and atomic form factor[104] of said atom type.

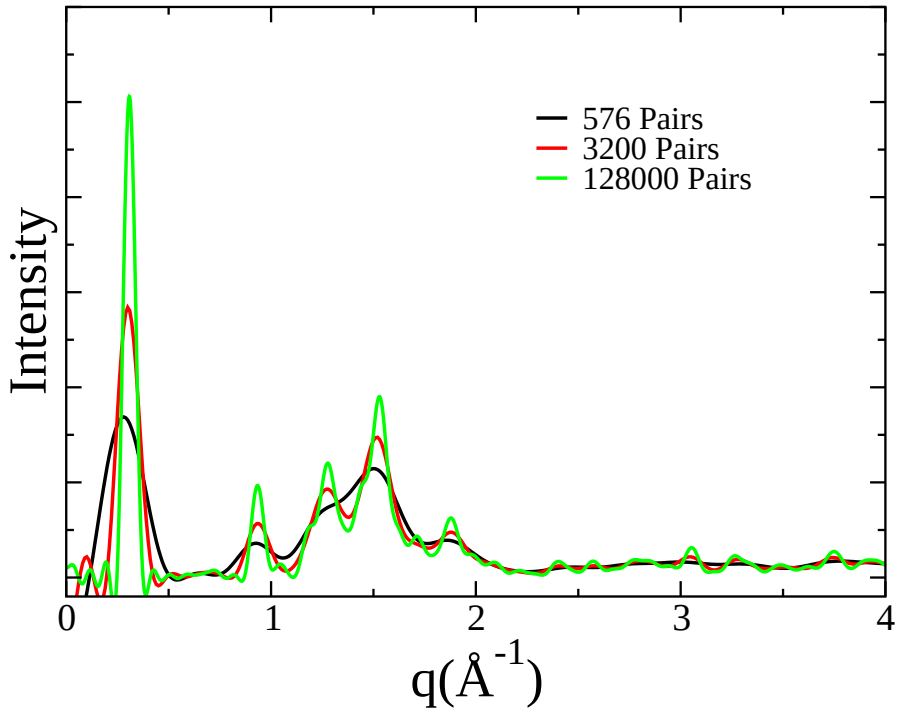

Note: Coherent intensity I_{coh} derived from (6.1) for crystalline $[C_{10}MIM^+][PF_6^-]$ as a function of system size computed using proper periodic boundary conditions for space group P $2_1/c$.

Figure 6.3: Coherent intensity I_{coh} as a function of system size

Fig. 6.3 shows the coherent intensity computed using (6.1) for $[C_{10}MIM^+][PF_6^-]$ crystals of different size constructed by replication of the unit cell[45] and by applying

proper periodic boundary conditions. Since the persistence lengthscale of a solid is infinite, the peaks converge to δ functions only as the box size approaches the macroscopic limit.

Approaching the same problem from the crystal literature perspective, one can compute the simulated powder pattern coherent intensity[92] from the known crystal structure. Each of the lines in the powder spectrum is associated with a family of Bragg crystal planes.

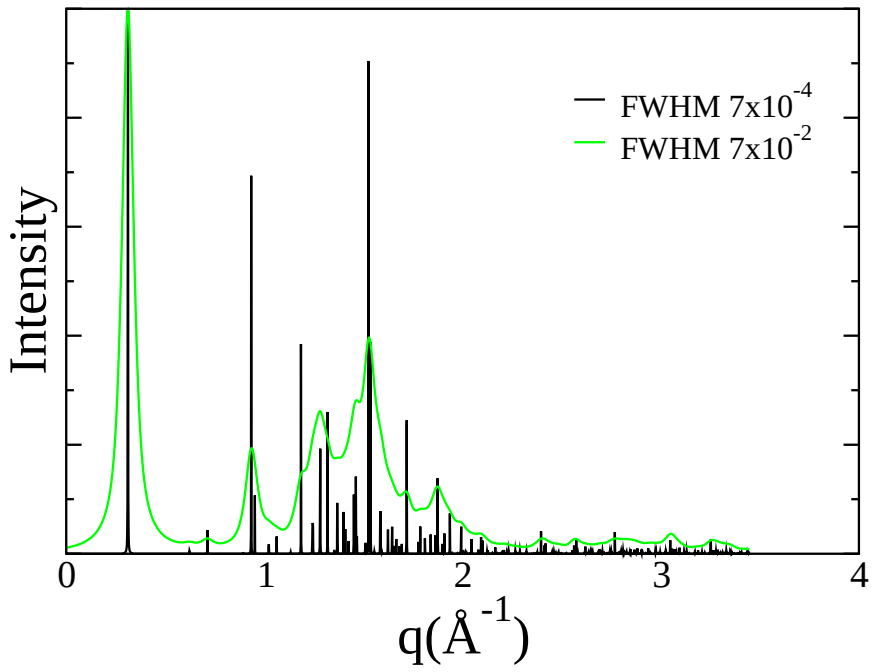

Note: Coherent powder pattern intensity of $[C_{10}MIM^+][PF_6^-]$ (identifier ODOLOJ) simulated from the known crystal structure[45] using Mercury.[92] FWHM in units of $Å^{-1}$.

Figure 6.4: Powder pattern from mercury for $[C_{10}MIM^+][PF_6^-]$ system

Fig. 6.4 shows the coherent intensity computed this way. Clearly, Fig. 6.4 and Fig. 6.3 coincide once broadening is introduced in the powder pattern calculation.

The three characteristic features found in the coherent scattering intensity of the liquid (or in S(q)) at around 0.4Å^{-1} , 0.9Å^{-1} and 1.5Å^{-1} exist also in the crystal. The single isolated peak in the powder spectrum closest to the frequency of the liquid prepeak corresponds to reflections of the [1,0,0] family of crystal planes. These planes represent the boundary of the unit cell perpendicular to the longest cell axis. The shoulder feature in the liquid at about 0.9Å^{-1} corresponds to the crystal lines at about the same q value which are mainly due to reflections from planes [3,0,0] and [1,1,-1] whereas the intense broad band at around 1.5Å^{-1} in the liquid corresponds to the scattering of a large number of different crystal planes.

Most scattering intensity in these systems results from the anions and the polar head of the cations (together, commonly referred as the polar groups). It is therefore reasonable to expect Miller planes of high intensity to coincide with *loci* of high density of polar group scatterers. Fig. 6.5 shows Miller planes [1,0,0] giving rise to the prepeak in solid $[C_{10}MIM^{+}][PF_6^{-}]$.

Clearly, in the crystal, the FSDP corresponds to the typical inverse length separation between polar groups of neighboring ions separated by the longest alkyl tail of the cations. The intermediate feature at around 0.9Å^{-1} due to planes [1,1,-1] and [3,0,0] can be interpreted as arising from short characteristic separations between polar groups in adjacent ions not separated by long alkyl tails. Fig. 6.6 and Fig. 6.7 show family of planes [3,0,0] and[1,1,-1] respectively. Within a unit cell, two out of

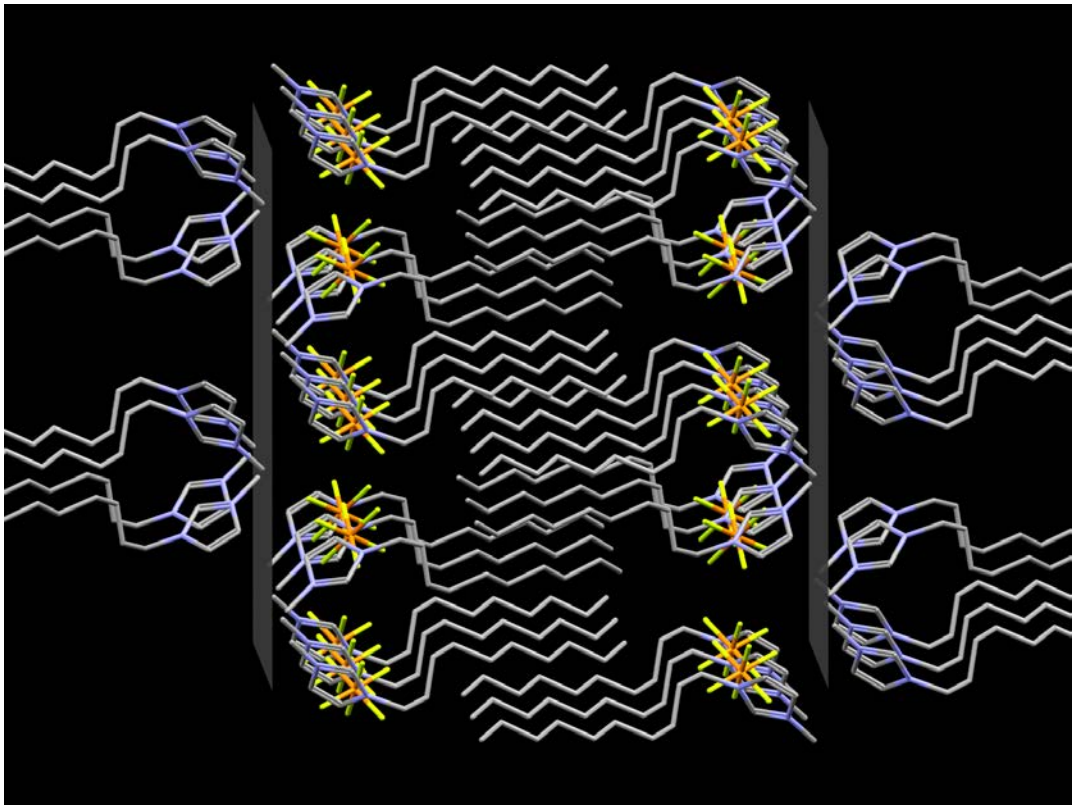

Note: Miller planes [1,0,0] of $[C_{10}MIM^+][PF_6^-]$ (identifier ODOLOJ). The scattering from this family of planes gives rise to the prepeak in the solid.

Figure 6.5: [1,0,0] Plane of $[C_{10}MIM^+][PF_6^-]$ crystal structure

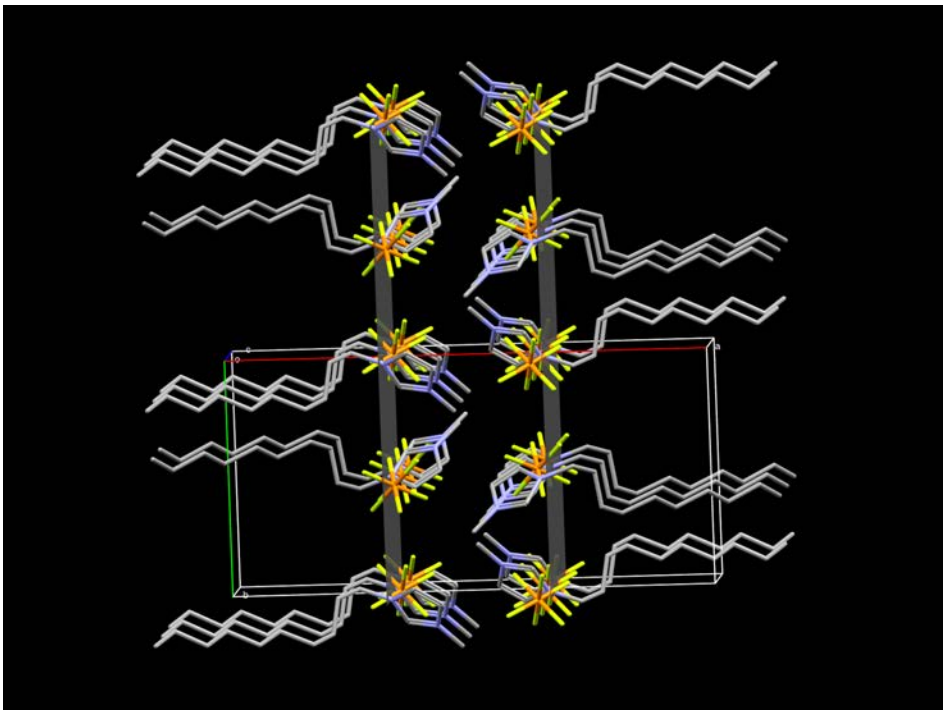

Figure 6.6: Miller planes [3,0,0] of $[C_{10}MIM^+][PF_6^-]$ (identifier ODOLOJ).

three times planes [3,0,0] fall close to polar groups which are heavily weighted in the coherent intensity by their atomic form factors.

Planes [1,1,-1] are very interesting since they define the characteristic distance between polar groups of the same charge. We will demonstrate in 6.3.3 that our interpretation of this characteristic distance in the solid will still be valid in the liquid for the shoulder peak at around 0.9Å^{-1} . Fig. 6.7 shows that [1,1,-1] planes lie almost along the long alkyl tail of the cations and are intercalated by $[PF_6^-]$ anions.

Of the many crystal planes that can be associated with the intense features close to 1.5Å^{-1} , those that are intermolecular in nature correspond to short close contact distances between ions.

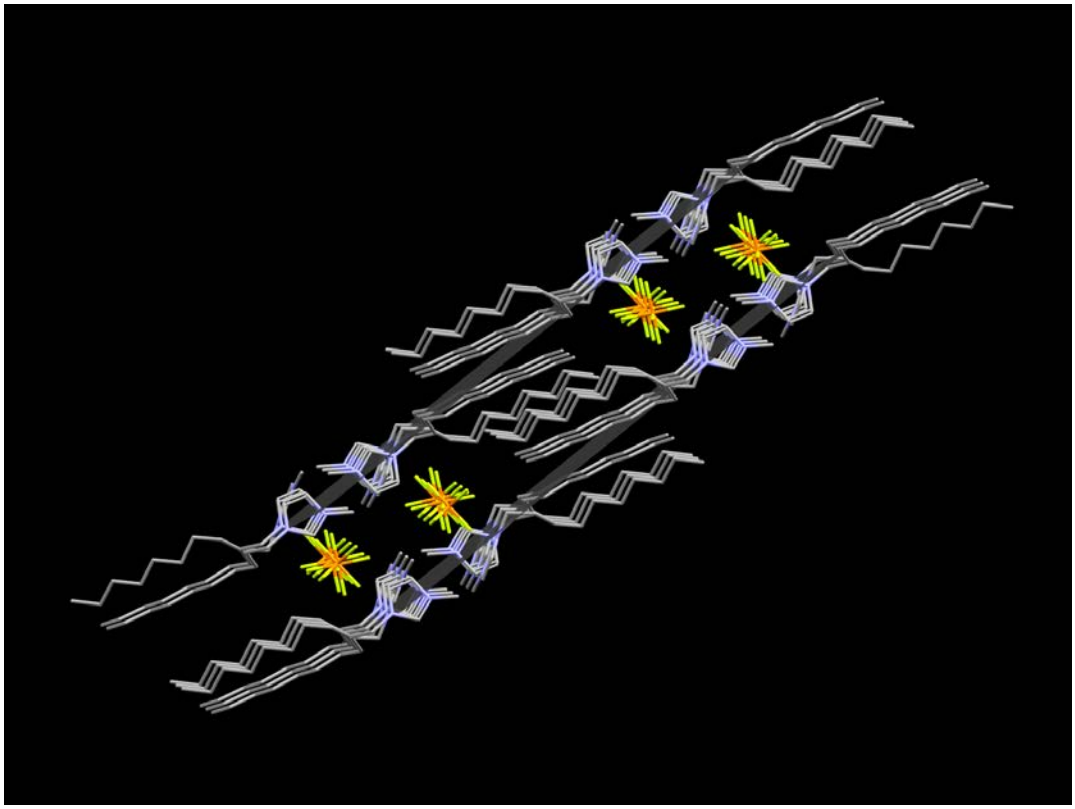

Note: Miller planes [1,1,-1] of $[C_{10}MIM^+][PF_6^-]$ (identifier ODOLOJ) which define the characteristic distance between ions of the same charge

Figure 6.7: [1,1,-1] plane of $[C_{10}MIM^+][PF_6^-]$ crystal structure

6.3.2 The Evolution of the structure function through the melting transition and a 3D view of local liquid structure

Fig. 6.8 shows simulated coherent intensity and S(q) for the $[C_{10}MIM^+][PF_6^-]$ system as a function of time during melting. As the crystal melts, the change in density results in a shift of all peaks towards lower q values (larger inter ionic distances). What originally was a peak at around 0.9Å^{-1} in the solid phase becomes a shoulder in the liquid phase. The peak originally at about 1.5Å^{-1} significantly broadens and

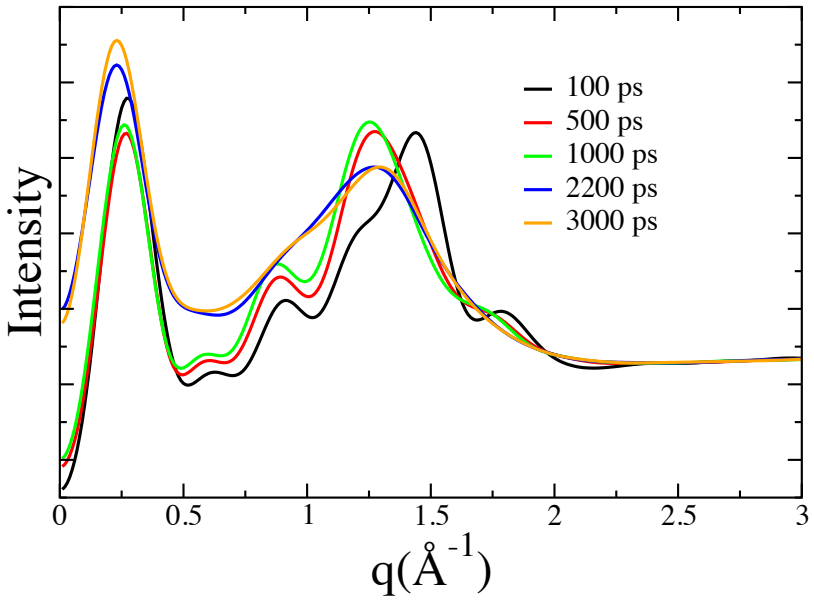

(a)

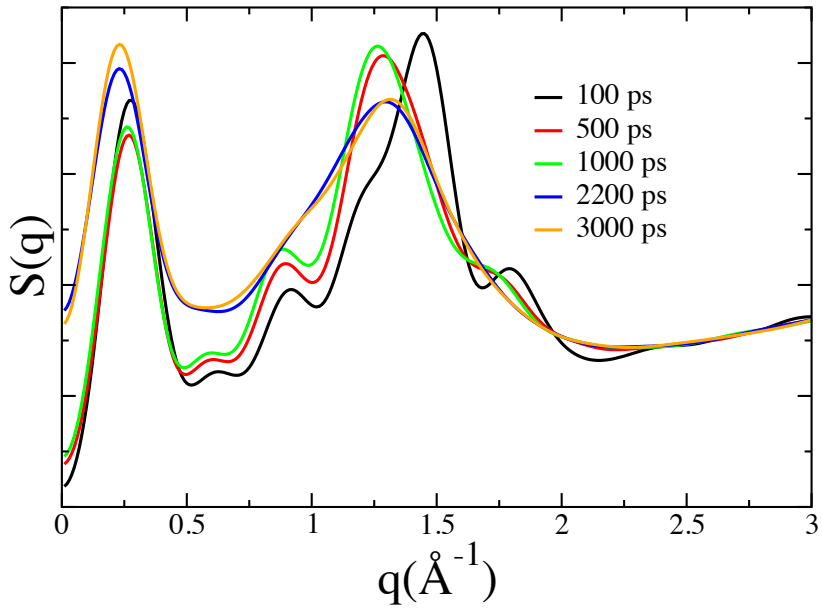

(b)

(a) Coherent intensity and (b) S(q) computed along a melting simulation of $[C_{10}MIM^+][PF_6^-]$

Figure 6.8: Structure functions during the melting of $[C_{10}MIM^+][PF_6^-]$

shifts to lower q values.

Many of the features in the crystal persist in an average way in the liquid phase. This can be appreciated from the 3-D density isosurfaces depicted in Fig. 6.9(a) and Fig. 6.9(b) around the cations in $[C_6MIM^+][Cl^-]$ and $[C_8MIM^+][PF_6^-]$ respectively. Fig. 6.9(a) shows the distribution of $[Cl^-]$ (red) and $[C_6MIM^+]$ heads (green) around $[C_6MIM^+]$ whereas Fig. 6.9(b) shows the distribution of P atoms in $[PF_6^-]$ (red) and head atoms in $[C_8MIM^+]$ (green) around $[C_8MIM^+]$. The alternating nature of the polar components which for the most part stay away from the non-polar alkyl tails, is clearly reminiscent of the solid state. A similar analysis can be made from the perspective of the anion. 3-D density isosurfaces of $[C_8MIM^+]$ heads and P atoms around $[PF_6^-]$ in $[C_8MIM^+][PF_6^-]$ are shown in Fig. 6.10.

6.3.3 Contributions of the partial structure functions

The total static structure function is computed from (6.2)

$$S(q) = \frac{\rho_o \sum_i \sum_j x_i\, x_j\, f_i(q) f_j(q) \int_0^\infty 4\pi r^2 (g_{ij}(r) - 1) \frac{\sin qr}{qr} dr}{\left[\sum_i x_i f_i(q)\right]^2} \tag{6.2}$$

where, ρ_0 is the bulk density and $g_{ij}(r)$ is the corresponding pair distribution functions for atom types i and j (other quantities have been previously defined in (6.1)). In order to unequivocally identify the species giving rise to the prepeak and shoulder peak, it is instructive to dissect S(q) into its properly form factor weighted subcomponents

$$\frac{\rho_o x_i\, x_j\, f_i(q) f_j(q) \int_0^\infty 4\pi r^2 (g_{ij}(r) - 1) \frac{\sin qr}{qr} dr}{\left[\sum_i x_i f_i(q)\right]^2}.$$

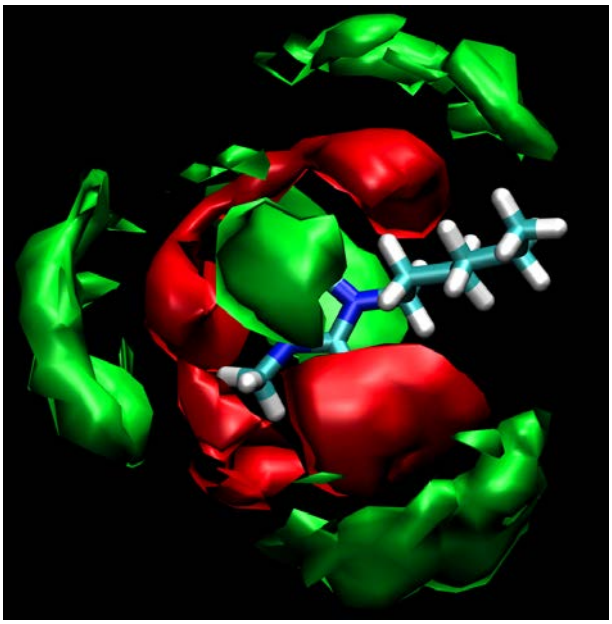

(a)

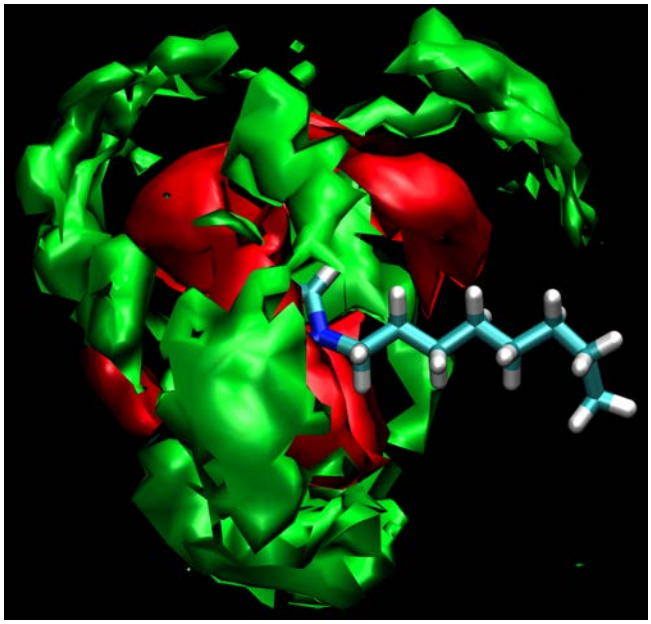

(b)

(a) Density isosurfaces of [Cl^-] (red) and [C_6MIM^+] heads (green) around [C_6MIM^+] in [C_6MIM^+][Cl^-] and (b) density isosurfaces of P atom in [PF_6^-] (red) and [C_8MIM^+] heads (green) around [C_8MIM^+] in [C_8MIM^+][PF_6^-]

Figure 6.9: Iso-density surfaces around the cations

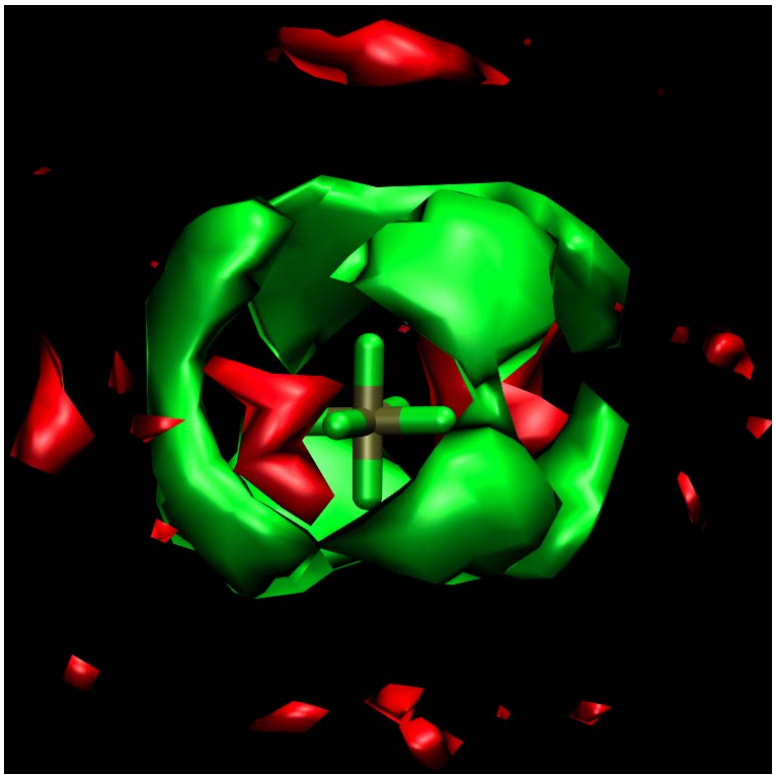

Figure 6.10: Density isosurfaces of [C_8MIM^+] heads (green) and P atom in [PF_6^-] (red) around [PF_6^-] in [C_8MIM^+][PF_6^-]

Fig. 6.11(a) and Fig. 6.11(b) show these subcomponents in the case of $[C_6MIM^+][Cl^-]$ and $[C_8MIM^+][PF_6^-]$ respectively.

It is clear from Fig. 6.11 that in both liquids N atoms and the anion, not the carbons, are responsible for the appearance of the prepeak. Clearly, just as in the case of solid $[C_{10}MIM^+][PF_6^-]$, this indicates that the FSDP is associated with a characteristic inverse lengthscale between polar groups. This lengthscale is larger in the liquid since it appears at lower q values as shown in Fig. 6.8. In 6.3.4 we present a detailed analysis of the geometric origin of this characteristic distance in the liquid phase.

Fig. 6.12 provides complementary information to the selective deuteration neutron scattering studies recently published by Hardacre and coworkers[54]. Fig. 6.12 shows why, whereas C and N have similar atomic form factor weights and the fraction of C atoms is much larger, the contribution of C to the prepeak is negligible. Subdividing the carbon contribution into head and tail groups results in three terms: head-head, tail-tail and head-tail. The first two introduce a peak in the S(q) at the prepeak region whereas the cross term introduces a trough that cancels it. This off phase spatial behavior tells us that on average there is absence of tails where one would expect to find heads and *vice versa*.

This result combined with the fact that in the liquid phase the terminal carbon of the longest alkyl tail is most likely to be found closest to other terminal carbons (as shown in Fig. 6.13) provides some clues regarding the typical separation distance between groups of atoms that without negative interference give rise to the prepeak.

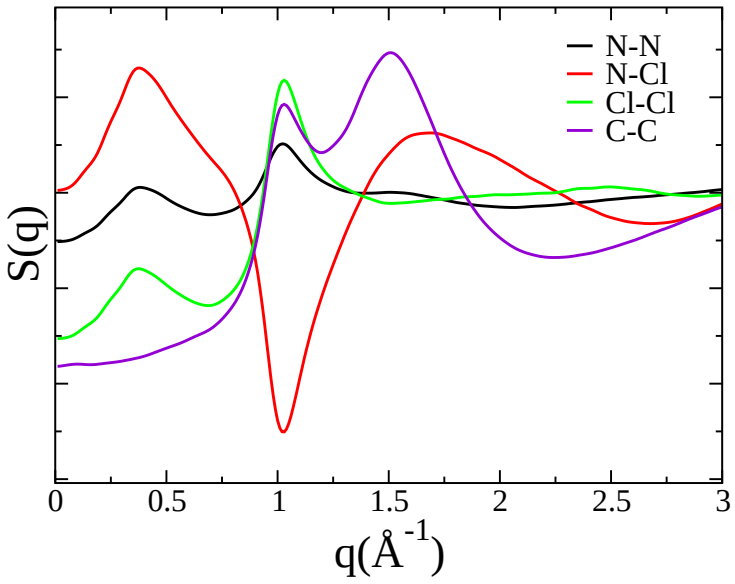

(a)

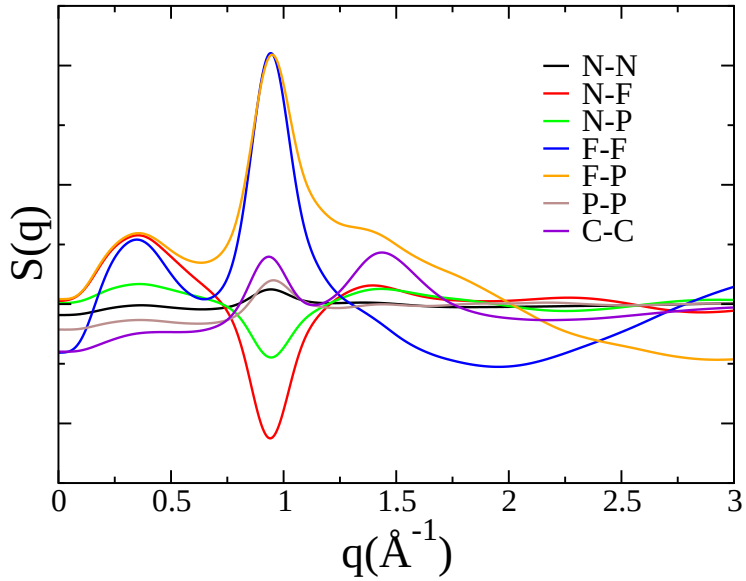

(b)

(a) Atomic subcomponents of S(q) in liquid $[C_6MIM^+][Cl^-]$ and (b) atomic subcomponents of S(q) in liquid $[C_8MIM^+][PF_6^-]$

Figure 6.11: Partial structure factors for $[C_6MIM^+][Cl^-]$ and $[C_8MIM^+][PF_6^-]$ systems

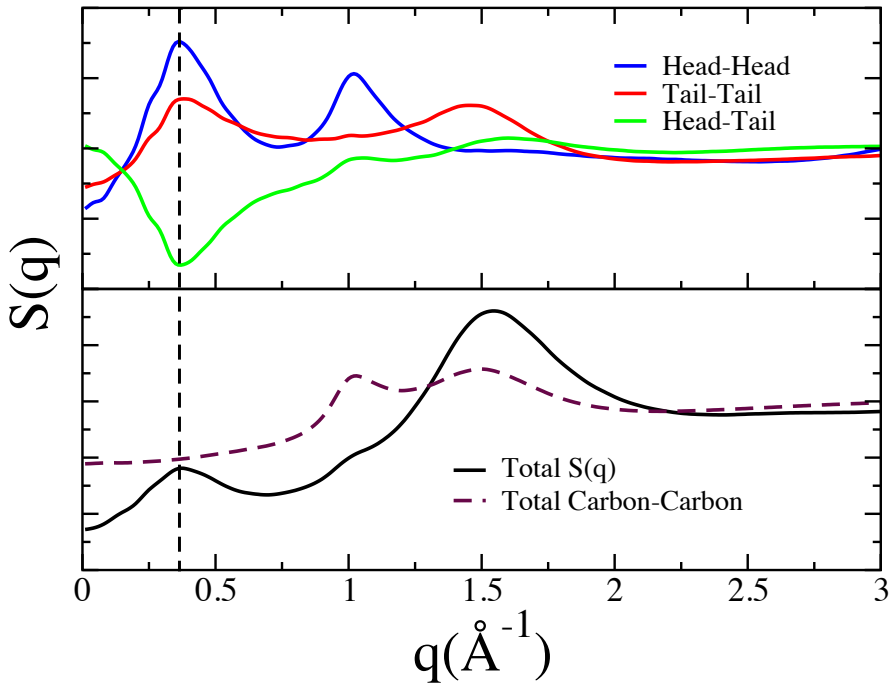

Upper panel: Head-Head, Tail-Tail and Head-Tail partial carbon structure functions of $[C_6MIM^+]$ in liquid $[C_6MIM^+][Cl^-]$. Lower panel: Total S(q) and partial Carbon-Carbon S(q) obtained from the sum of the three functions in the upper panel weighted by $(x_C^{Head} \times x_C^{Head})$, $(x_C^{Tail} \times x_C^{Tail})$ and $2(x_C^{Head} \times x_C^{Tail})$ respectively. Here, $x_C^{Head} = \frac{4}{32}$ and $x_C^{Tail} = \frac{6}{32}$ are the fraction of head and tail carbon atoms as defined in 6.1. Clearly there is almost complete cancellation of carbon contribution to the prepeak region

Figure 6.12: Splitting of Carbon-Carbon Partial structure factor

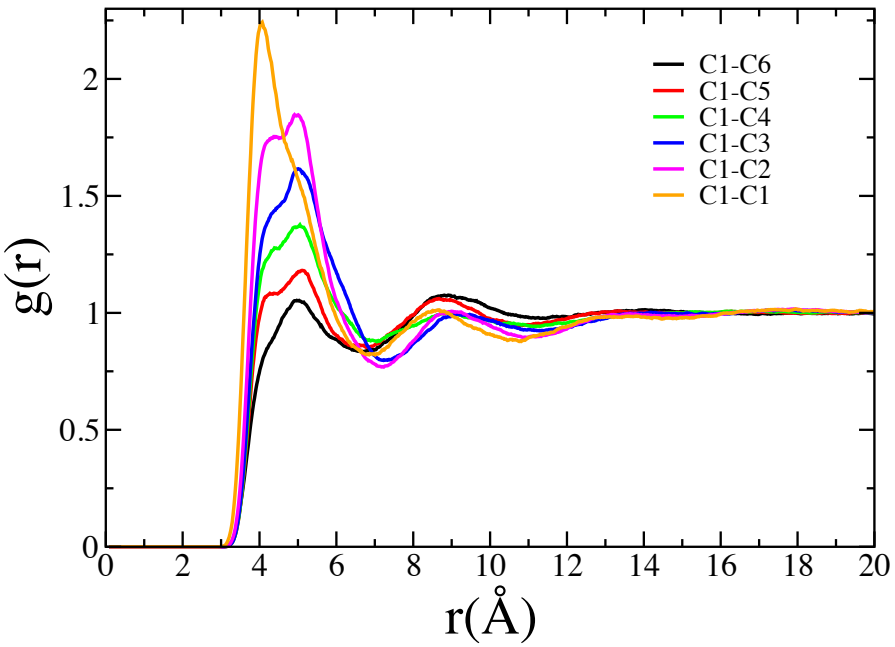

Note: Radial distribution function between carbon atoms in the long alkyl tail of $[C_6MIM^+][Cl^-]$. Carbon atoms are labeled starting at 1 from the terminal carbon.

Figure 6.13: RDF between carbon atoms of long alkyl tail

Perhaps equally as interesting in the comparison of solid and liquid phases is the interpretation of the S(q) subcomponents responsible for the shoulder peak at around 0.9Å^{-1} . In the crystal phase, two planes with Miller indexes [3,0,0] and [1,1,-1] were responsible for this feature (see Fig. 6.6 and Fig. 6.7). Careful mathematical analysis (not shown) explains why in the crystal phase, reflections from the [1,1,-1] planes are of less intensity[6, 31]. The scattering intensity computed from fractional distances and lattice planes turns out to be a sum of cation-cation, anion-anion and cation-anion cross terms. In the case of the [1,1,-1] plane, all of these terms are large, but the cross term is of similar magnitude and opposite sign resulting in significant intensity cancellation. In 6.3.1 we showed that planes [1,1,-1] define the short interi-

onic distance between polar groups of the same charge (see Fig. 6.7). In the liquid, the feature at 0.9Å^{-1} has the same phase characteristics as the [1,1,-1] plane in the solid. This is clearly seen from Fig. 6.11(a) and Fig. 6.11(b) where Cl-Cl, P-P and N-N terms give rise to positive contributions while the cross terms N-Cl or N-P give rise to negative contributions. This indicates that the periodicity of plane [1,1,-1] is preserved in the liquid phase. Since this lengthscale corresponds to the short distance between polar groups of the same sign, it can also be interpreted as a periodicity in the absence of ions of opposite charge at that particular distance.

6.3.4 Prepeak in liquid Phase

While the comparison between liquid and solid spectral features has helped us draw conclusions about the nature of S(q) in the liquid phase, a most satisfying explanation of the origin of the FSDP should be attempted without invoking the now established origin of this feature in the solid. The conclusion of this analysis can at a later point be contrasted against what we know from the crystal phase. Of the different RTILs that are studied here, we have chosen to focus in this section on $[C_6MIM^+][Cl^-]$ because it is the shorter alkyl tail systems that challenge our understanding of the identity of the prepeak the most. The prepeak of $[C_6MIM^+][Cl^-]$ in the liquid state is of low intensity compared to other reciprocal space features in the low q regime. Because in alkylimidazolium systems with shorter tails the inherent disorder in the liquid phase makes it quite difficult to assign longer range correlations unequivocally, to gain important insight, the community has often approached the

problem through visual inspection of 3-D computer simulation snapshots, that while quite illustrative have the potential to be misleading. This is because snapshots only present circumstantial configurational evidence of structures or morphologies. Instead, we present a method not based on visual inspection, that attempts to tease out the global coordinates that couple most strongly to the magnitude of the prepeak.

The inverse Fourier transform of the prepeak corresponds to a real space sum of waves. Since in the liquid state the intensity of the prepeak is small compared to that of other spectral features, filtering out the prepeak in reciprocal space results in real space atomic RDFs with very modest changes. This is evident in the case of the Cl-Cl and Cl-N correlations shown in Fig. 6.14(a) and Fig. 6.14(b) respectively. The reader is reminded that these are the most important correlations giving rise to the prepeak.

One is therefore unable to gain much insight by simple comparison of RDFs that include or exclude information about the prepeak. In other words, geometrically, this particular liquid would appear to be quite similar if it had no prepeak. It is therefore our goal to exaggerate this reciprocal space feature as a way to identify its origin in the liquid and to establish global molecular positions that produce unphysical S(q)s enriched in the frequencies of the prepeak band.

We approach this problem from a multivariate optimization perspective using the praxis algorithm[14]. From Fig. 6.11(a) and (6.2) it is clear that N-N, N-Cl and Cl-Cl correlations are the most heavily weighted in the prepeak region of liquid $[C_6MIM^+][Cl^-]$. Therefore, the global optimization routine is asked to maximize the

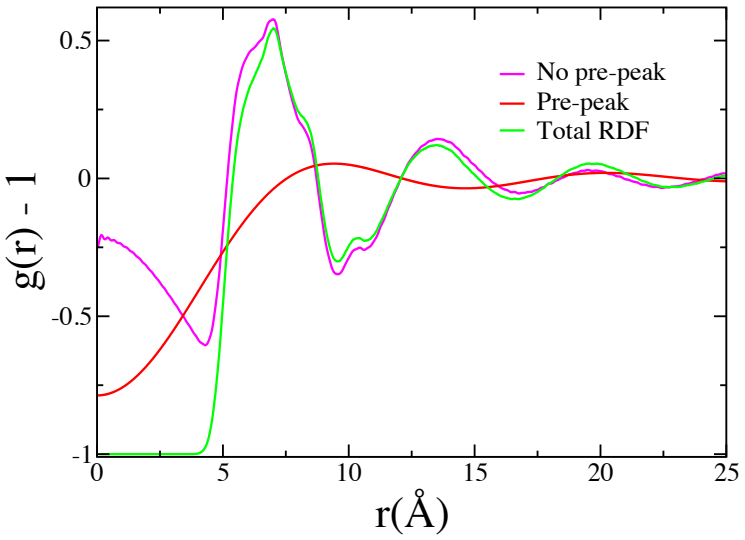

(a)

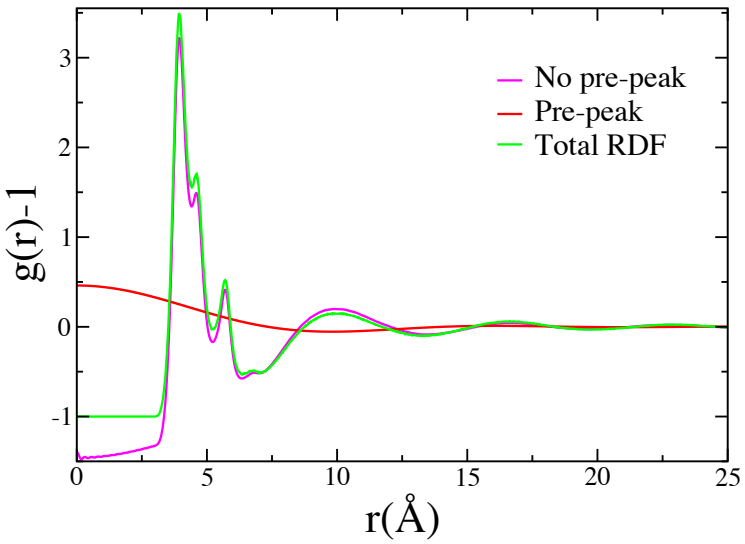

(b)

Note: In red is the inverse Fourier transform of the prepeak region; in magenta is (g(r)-1) when the contribution of the prepeak region is filtered out, and in green is the full (g(r)-1) in the case of (a) Cl-Cl correlations and (b) N-Cl correlations in liquid $[C_6MIM^+][Cl^-]$. Clearly filtering out the prepeak produces modest changes in the RDFs of the atomic species that should be the most affected by the prepeak.

Figure 6.14: Inverse Fourier transforms partial S(q)s

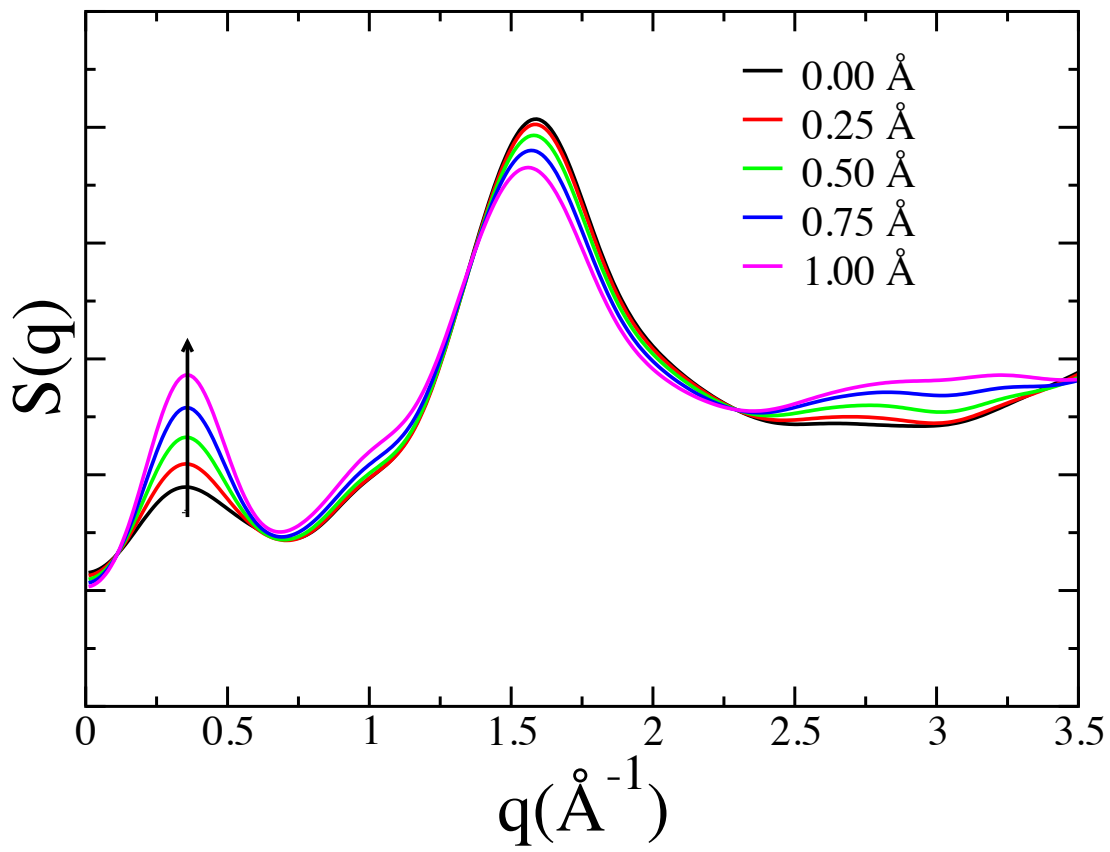

Note: Total S(q) enriched in the frequencies of the prepeak. Ions are displaced along the vector than enhances S(q) in increments defined in the figure legend.

Figure 6.15: Enhancement of prepeak

intensity of the prepeak generated from the form factor weighted sum of these sub-components of S(q) by translating ions. We further impose the reasonable geometric constraint that ions not move more than 1Å. The enrichment of the total S(q) in the frequencies of the prepeak due to this optimization procedure is shown in Fig. 6.15.

Fig. 6.16(a) and Fig. 6.16(b) show RDFs between Cl-Cl and Cl-N as we displace ionic coordinates in the global directions that enrich S(q). The enrichment gives rise to RDFs that clearly show polar groups coming closer together, while the second

peak in the RDF becomes of lower intensity and in the case of Cl-Cl slightly moves to longer distances.

Fig. 6.17(a) shows an enlarged snapshot of the system used for optimization (the actual snapshot is replicated one time in each positive and negative direction along x, y and z for visual clarity). Fig. 6.17(b) shows the polar groups in the same liquid snapshot whereas Fig. 6.17(c) shows the same groups after displacements are applied in the direction derived from the optimization procedure. It is clear that exaggerating the importance of the prepeak results in the grouping of nearest neighbor polar groups and separation from other polar groups by a characteristic longer lengthscale.

As shown in Fig. 6.5, in the case of solid $[C_{10}MIM^+][PF_6^-]$, this longer lengthscale is defined by the separation between planes [1,0,0] corresponding to the distance between polar groups separated by the longer cationic alkyl tail . Fig. 6.11(a) proves that in liquid $[C_6MIM^+][Cl^-]$ the mild prepeak also arises due to the correlation between N and Cl atoms. These polar group atoms are separated because of the steric hindrance imposed by the longer cationic alkyl tail. In contrast to what is expected in the solid (as can be seen in the case of $[C_{10}MIM^+][PF_6^-]$ in Fig. 6.5), and in agreement with the experiments of Triolo[130], Fig. 6.13 indicates that in this liquid there is no tail interdigitation.

It is the intrinsic anisotropy in the geometry of the cation along the direction of the longer alkyl tail that prevents the close approach of other polar groups in that particular direction. As a consequence neighboring polar groups can either be in

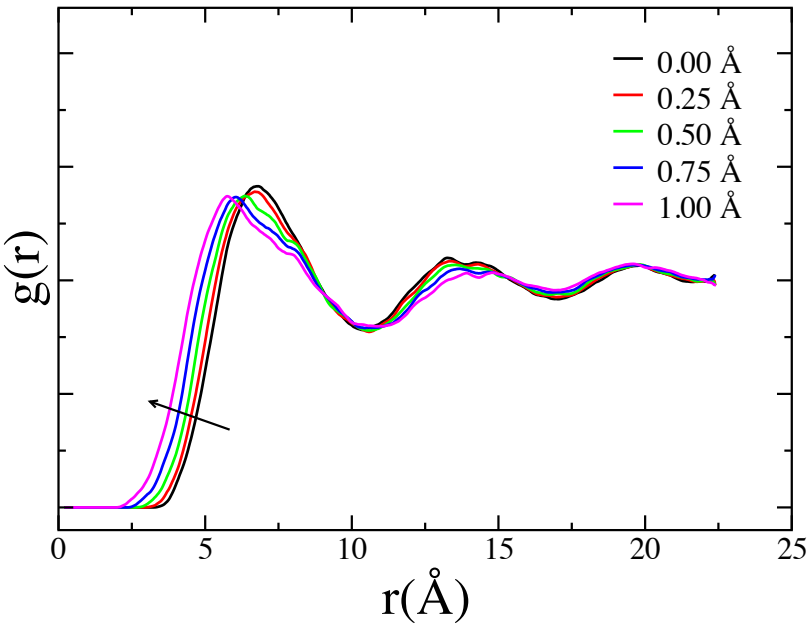

(a)

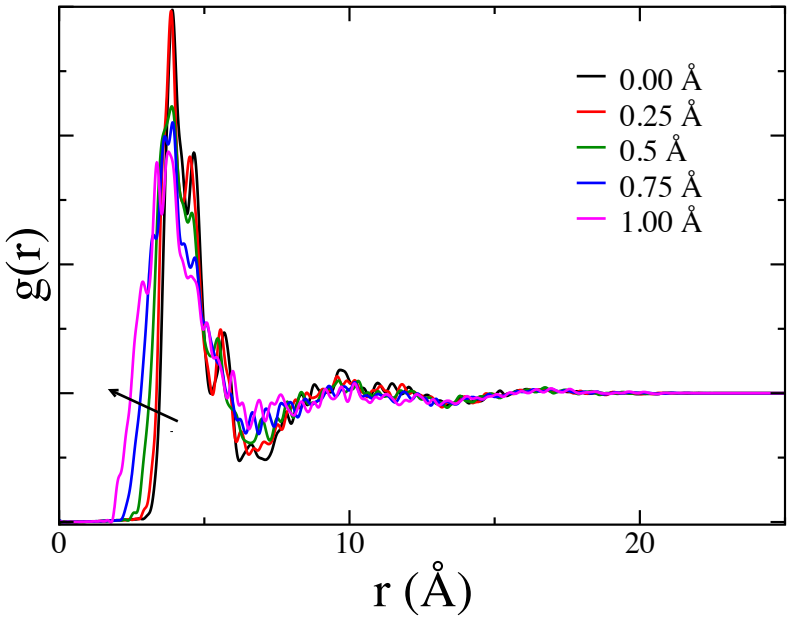

(b)

(a) Cl-Cl RDF and (b) N-Cl RDF as global coordinates are displaced to enhance S(q) in the frequencies of the prepeak.

Figure 6.16: Partial RDFs with the enhancement of prepeak

close contact as shown in Fig. 6.9 and Fig. 6.10 or appear further apart if they are separated by the long cationic tail. Since the prepeak is of very low intensity, this anisotropy is only barely noticeable in Fig. 6.17(b), however it becomes increasingly visible in Fig. 6.17(c) as we enhance the coordinates in the frequencies of the prepeak. In brief, both in the liquid and in the solid two characteristic distances exist between adjacent polar groups. A short distance much like the one we would expect from less structured ions giving rise to the shoulder peak at 0.9Å^{-1} and a longer separation due to the hindering presence of the long alkyl tail.

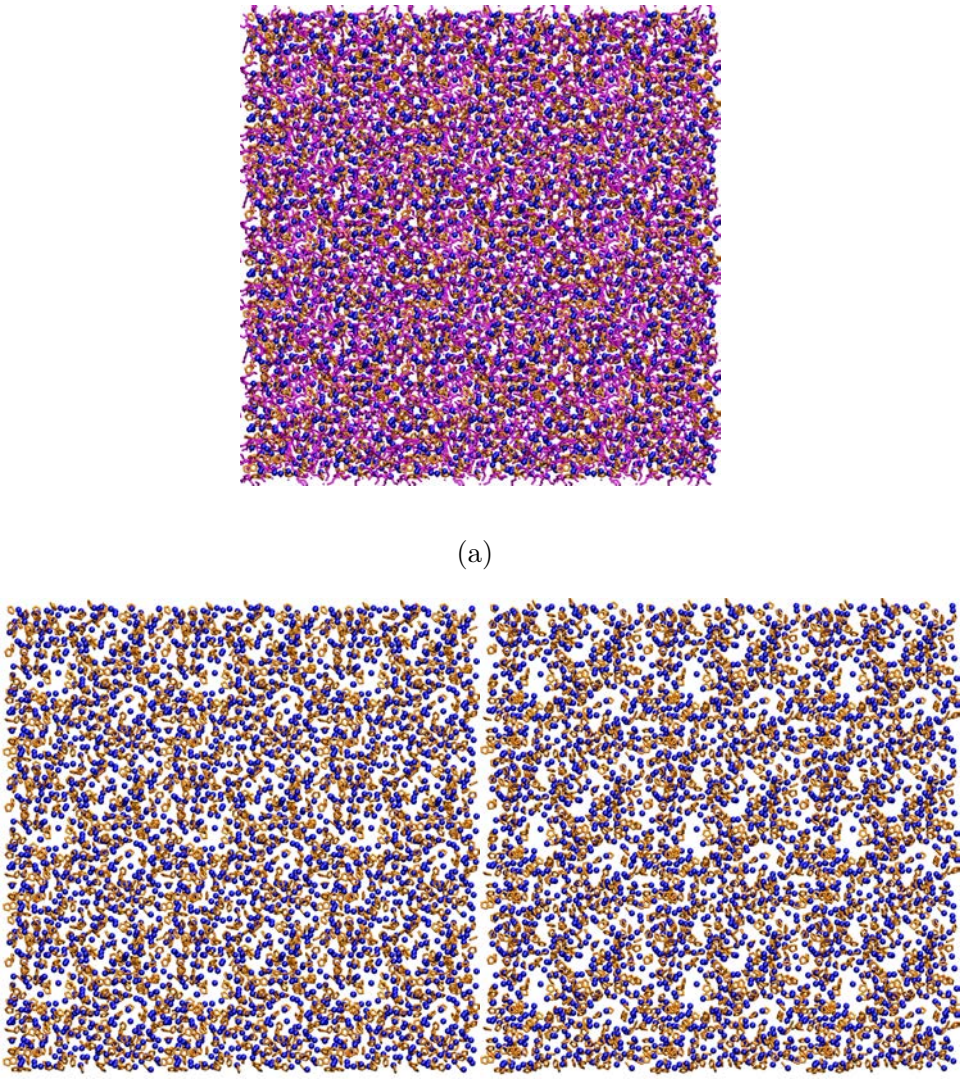

(a)

(b) (c)

(a) Depicts orthographic view of a typical system snapshot (periodically replicated in ± x, ± y and ± z); alkyl tails are in magenta, anions in blue and cation heads in orange, (b) shows only cation heads and anions for the same snapshot while (c) shows the same group of atoms after multivariate optimization to enhance the prepeak.

Figure 6.17: Snapshots of the liquids during the multivariate optimization to enhance the prepeak

6.4 Conclusion

Imidazolium based ionic liquids with moderately long alkyl tails and with spherical or highly symmetrical anions tend to show common features in the low q region of the coherent x-ray scattering intensity. These same features are also often present in the simulated coherent intensity of their solid powder pattern. The broad peak at 1.5Å^{-1} is due to intramolecular and close contact intermolecular interactions. Both in the solid and in the liquid phase, the shoulder peak at around 0.9Å^{-1} defines the typical short separation distance between polar groups of the same charge. The prepeak in the liquid and strong intensity [1,0,0] Miller planes in the solid define the typical distance between charged groups separated by the long cationic alkyl tails. In this family of systems the prepeak exists because of the intrinsic anisotropy of the cation. Two kind of nearest neighbors are possible, those in which close contact between polar groups are sterically allowed and those that because of cationic anisotropy are separated by a typical longer length scale associated with the long cationic alkyl tail. While the existence of complex morphologies is neither proved nor disproved by our study, it is fair to say that the anisotropy in the cation is a necessary but not a sufficient condition for such morphologies.

CHAPTER 7
SUMMARY, IMPACT AND FUTURE DIRECTIONS

The goal of this research work has been to understand both the dynamic and structural complexity of ionic liquids. Previous work in our research group had established that the slow nature of ionic liquids leads to distributed dynamics and persistent local environments. When certain solute molecules are photo excited in such systems, the resulting emission spectra is often but not always excitation wavelength dependent. One of the contributions of this thesis to our understanding of room temperature ionic liquids is that we show this phenomenon to be relevant not only to spectroscopic problems, but also to more general chemical problems such as electron transfer. Many experiments have since followed [83, 113, 79, 80, 111] confirming that indeed distributed dynamics is ubiquitous in these systems at room temperature. In particular, our studies have indicated that Marcus theory is likely valid for intra-molecular electron transfer reactions in room temperature ionic liquids but the shape of Marcus parabolas is local solvent environment dependent. This leads to reaction kinetics and local energetics that are distinct in different parts of these liquids. Different ionic liquids display these characteristics to different extents. A deep understanding of dynamics in room temperature ionic liquids will influence our ability to better control the outcome of chemical reactions. One can choose to work with liquids of varied relaxation time scales and hence influence the extent to which distributed dynamics will be relevant in a particular problem .

We have also studied the effect of water on the dynamics of ionic liquids.

Using computer simulations we explained that water screens Coulombic interactions between cations and anions and therefore increases rotational and translation diffusion of the ions. We also investigated how water affects the fluorescence spectrum of prototypical fluorescence probe coumarin-153 in these systems. Our results explain the faster dynamics observed in the time resolved experiments carried out in the group of Nilmoni Sarkar.

Whereas the first few chapters of my thesis are concerned with complexity in dynamics and chemical reactivity in ionic liquids, the final part of my thesis is devoted to structural complexity as manifested in SAXS-WAXS and neutron scattering types of experiments. Some of the work presented stems from collaborations with the Castner group that carried out measurements at different high energy facilities.

The intrinsic geometric anisotropy and amphiphilic nature of these materials adds complexity to their liquid phase structure. In this thesis we derive a set of equations that allows for exact partitionings of structure functions into components that are convenient to interpret. In this way, we can dissect intra- from intermolecular contributions, as well as cationic and anionic subcomponents. Our structural studies also involved extensive investigation of the origin of the pre-peak (or first sharp diffraction peak) observed in the low frequency region of x-ray and neutron scattering experiments of imidazolium based ionic liquids. The research community has conflicting opinions on the origin of the pre-peak. This feature in the x-ray or neutron scattering is often attributed to nanoscale segregation of ions forming domains of different morphologies. It has frequently been proposed that the pre-peak

may be due to morphologies such as bi-layers or micelles. While our studies do not necessarily disprove these assertions, they appear to agree with recent experiments in the Hardacre laboratory that suggest the pre-peak can be explained by much simpler consideration of solvation shell asymmetry. The asymmetry giving rise to the pre-peak scales with alkyl tail length since tails are the spacers between the strongly scattering polar groups.

Ionic liquids appears to display two or three (depending on whether they have a prepeak) intermolecular features in S(Q). Often a broad peak at large Q corresponds to adjacency correlations. These are either close contacts between cations and anions, hydrophobic contacts between non-polar parts or intramolecular components. At lower Q values we find a peak or shoulder that is the result of very large positive and negative cancellations. This shoulder or peak is the signature of charge alternation in ionic liquids and is due to the systematic distance between ions of the same charge. The negative contribution to this feature is due to a systematic absence of ions of opposing charges at this given inverse distance. This cancellation of large factors is sometimes almost perfect and in such cases the feature is absent. The peak at lowest Q value, when present, is the so-called prepeak. In the systems we have studied, this peak is a manifestation of solvation environment anisotropy. In the case of imidazolium based ionic liquids, it corresponds to the inverse distance between anions or polar heads of the cations separated by the longer alkyl tails.

APPENDIX A
ATOMIC CHARGES FOR CRYSTAL VIOLET LACTONE(CVL)

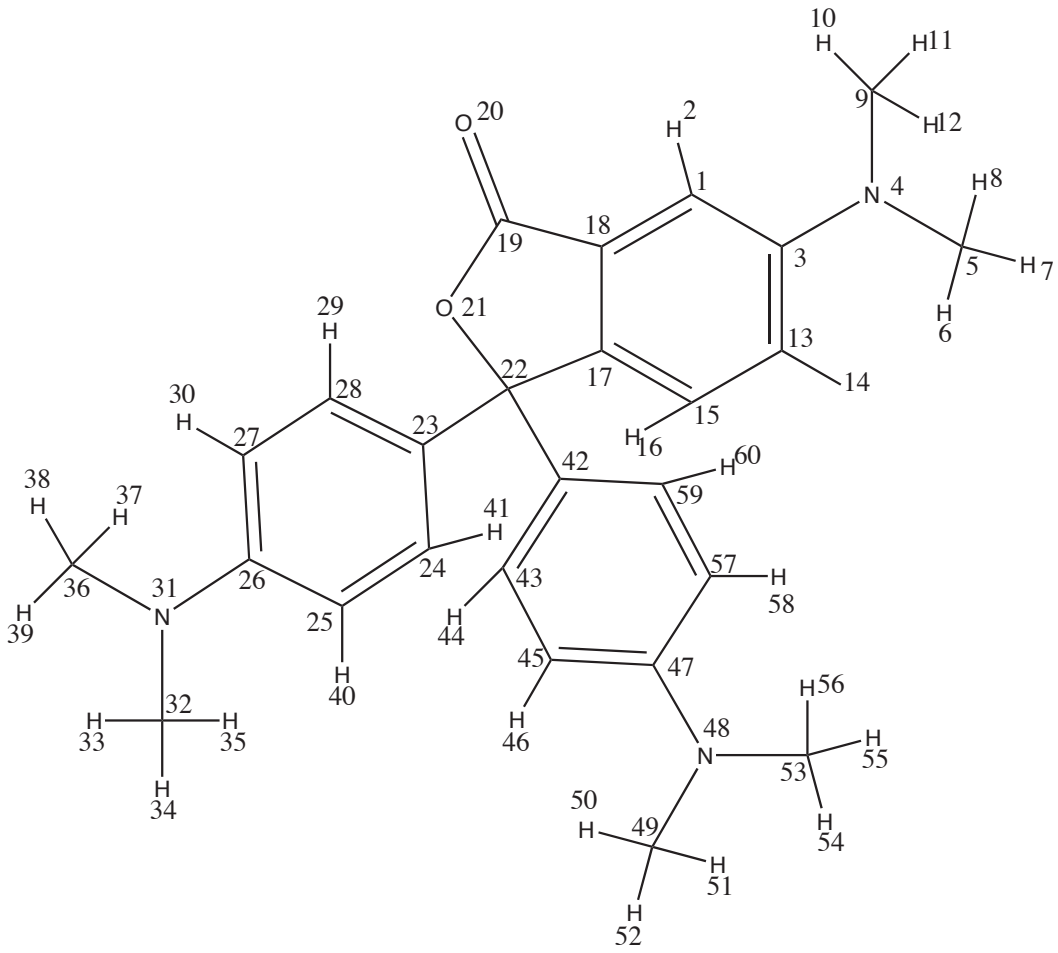

Figure A.1: Crystal violet lactone(CVL)

.

Table A.1: Partial charges for CVL

Atom No.	S0	S1	S2a	S2b
1	-0.0247	-0.1733	-0.1733	-0.1733
2	0.0404	0.1150	0.1150	0.1150
3	0.1168	0.0398	0.0398	0.0398
4	-0.2684	0.0303	-0.4497	-0.4497
5	0.0690	0.0300	0.0300	0.0300
6	0.0168	0.0600	0.0600	0.0600
7	0.0168	0.0600	0.0600	0.0600
8	0.0168	0.0600	0.0600	0.0600
9	0.0690	0.0300	0.0300	0.0300
10	0.0168	0.0600	0.0600	0.0600
11	0.0168	0.0600	0.0600	0.0600
12	0.0168	0.0600	0.0600	0.0600
13	-0.0350	-0.1994	-0.1994	-0.1994
14	0.0246	0.1150	0.1150	0.1150
15	-0.0296	-0.1657	-0.1657	-0.1657
16	0.0239	0.1150	0.1150	0.1150
17	0.0204	0.0604	0.0424	0.0424
18	-0.0020	-0.0340	-0.0340	-0.0340

Note: Labels are shown in Figure A.1.

Table. A.1 continued

Atom No.	S0	S1	S2a	S2b
19	0.4773	0.4453	0.4453	0.4453
20	-0.5271	-0.6771	-0.7771	-0.7771
21	-0.2759	-0.3019	-0.3239	-0.3239
22	0.1778	0.1678	0.1478	0.1478
23	0.0042	0.0042	0.0030	0.0054
24	-0.0268	-0.1196	-0.1084	-0.1208
25	-0.0519	-0.1446	-0.1549	-0.1443
26	0.1202	0.1202	0.1223	0.1181
27	-0.0519	-0.1446	-0.1549	-0.1443
28	-0.0268	-0.1196	-0.1084	-0.1208
29	0.0222	0.1150	0.1150	0.1150
30	0.0223	0.1150	0.1150	0.1150
31	-0.2687	-0.4546	0.1864	-0.4555
32	0.0693	0.0300	0.0300	0.0300
33	0.0159	0.0600	0.0600	0.0600
34	0.0159	0.0600	0.0600	0.0600
35	0.0159	0.0600	0.0600	0.0600
36	0.0693	0.0300	0.0300	0.0300

Table. A.1 contiued

Atom No.	S0	S1	S2a	S2b
37	0.0159	0.0600	0.0600	0.0600
38	0.0159	0.0600	0.0600	0.0600
39	0.0159	0.0600	0.0600	0.0600
40	0.0223	0.1150	0.1150	0.1150
41	0.0222	0.1150	0.1150	0.1150
42	0.0042	0.0042	0.0054	0.0030
43	-0.0268	-0.1196	-0.1208	-0.1084
44	0.0222	0.1150	0.1150	0.1150
45	-0.0519	-0.1446	-0.1443	-0.1549
46	0.0223	0.1150	0.1150	0.1150
47	0.1202	0.1202	0.1181	0.1223
48	-0.2687	-0.4546	-0.4555	0.1864
49	0.0693	0.0300	0.0300	0.0300
50	0.0159	0.0600	0.0600	0.0600
51	0.0159	0.0600	0.0600	0.0600
52	0.0159	0.0600	0.0600	0.0600
53	0.0693	0.0300	0.0300	0.0300
54	0.0159	0.0600	0.0600	0.0600

Table. A.1 continued

Atom No.	S0	S1	S2a	S2b
55	0.0159	0.0600	0.0600	0.0600
56	0.0159	0.0600	0.0600	0.0600
57	-0.0519	-0.1446	-0.1443	-0.1549
58	0.0223	0.1150	0.1150	0.1150
59	-0.0268	-0.1196	-0.1208	-0.1084
60	0.0222	0.1150	0.1150	0.1150

APPENDIX B
ATOMIC CHARGES FOR METHYLTRIBUTYLAMMONIUM CATION($[N_{1444}^{+}]$)

Methyltributylammonium cation($[N_{1444}^{+}]$)

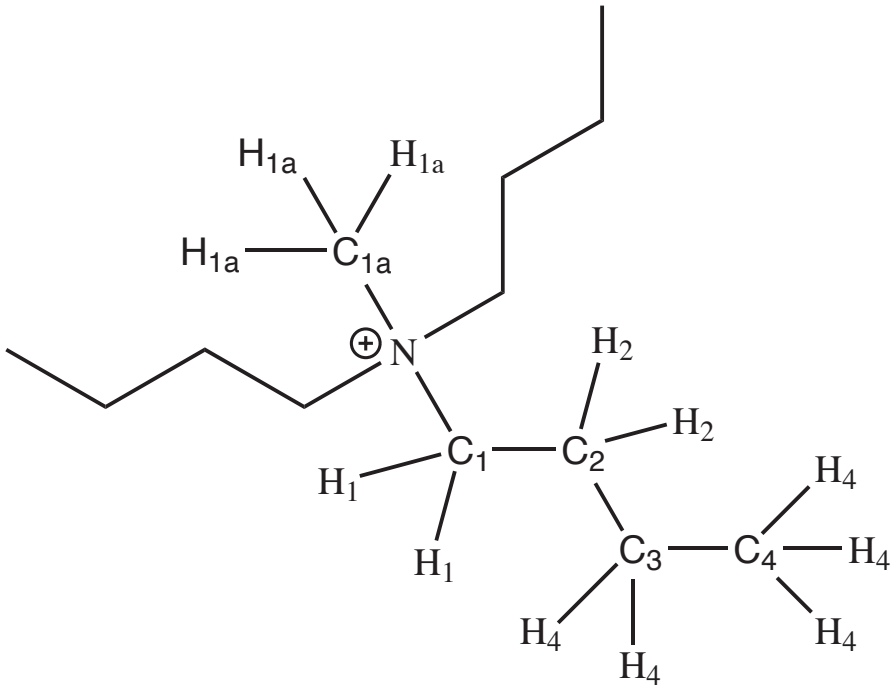

Figure B.1: $[N_{1444}^{+}]$ cation

.

Table B.1: Partial charges for the [N_{1444}^{+}]

Atom	Charge
H1a	0.14820
C1a	-0.30470
H1	0.14890
C1	-0.37010
H2	0.03890
C2	0.03530
H3	0.01400
C3	0.13360
H4	0.10080
C4	-0.36030
N	0.44820

Note: Labels are shown in Figure B.1.

REFERENCES

[1] M. P. Allen and D. J. Tildesley. *Theory of simple liquids*. Oxford University Press Inc. New York, 1st edition, 1987.

[2] Jessica L. Anderson, JaNeille K. Dixon, and Joan F. Brennecke. Solubility of CO2, CH4, C2H6, C2H4, O2, and N2 in 1-Hexyl-3-methylpyridinium Bis(trifluoromethylsulfonyl)imide: Comparison to Other Ionic Liquids. *Acc. Chem. Res.*, 40(11):1208–1216, 2007.

[3] H. V. R. Annapureddy, Hemant K. Kashyap, Pablo M. De Biase, and C. J. Margulis. What is the Origin of the Prepeak in the X-Ray Scattering of Imidazolium Based Room Temperature Ionic Liquids? *J. Phys. Chem. B*, 114:16838–16846, 2010.

[4] H. V. R. Annapureddy and C. J. Margulis. Controlling the Outcome of Electron Transfer Reactions in Ionic Liquids. *J. Phys. Chem. B*, 113(35):12005–12012, 2009.

[5] J. L. Anthony, E. Maginn, and J. F. Brennecke. Solution thermodynamics of imidazolium-based ionic liquids and water. *J. Phys. Chem. B*, 115(44):10942–10949, 2001.

[6] N. W. Ashcroft and N. D. Mermin, editors. *Solid State Physics*. Holt, Rinehart and Winston, New York, 1976.

[7] R. Atkin and G. G. Warr. The Smallest Amphiphiles: Nanostructure in Protic Room-Temperature Ionic Liquids with Short Alkyl Groups. *J. Phys. Chem. B*, 112(14):4164–4166, April 2008.

[8] S. N. Baker, G. A. Baker, Munson C. A., F. Chen, E. J. Bukowski, A. N. Cartwright, and F. V. Bright. Effects of solubilized water on the relaxation dynamics surrounding 6-propionyl-2-(n,n-dimethylamino)naphthalene dissolved in 1-butyl-3-methylimidazolium hexafluorophosphate at 298 k. *Ind. Eng. Chem. Res.*, 42(25):6457–6463, 2003.

[9] H. J. C. Berendsen, J. P. M. Postma, W. F. van Gunsteren, and J. Hermans. *Intermolecular Forces*. Reidel, Dordrecht, 1981.

[10] H. J. C. Berendsen, D. van der Spoel, and R. van Drunen. Gromacs: A message-passing parallel molecular dynamics implementation. *Comp. Phys. Comm.*, 91:43–56, 1995.

[11] B. L. Bhargava and S. Balasubramanian. Refined Potential Model For Atomistic Simulations Of Ionic Liquid [Bmim][PF6]. *J. Chem. Phys.*, 127(11):114510, 2007.

[12] S. R. Billeter, S. P. Webb, T. Iordanov, P. K. Agarwal, and S. Hammes-Schiffer. Hybrid approach for including electronic and nuclear quantum effects in moleucular dynamics simulations of hydrogen transfer reactions in enzymes. *J. Chem. Phys.*, 114:6925, 2001.

[13] A. E. Bradley, C. Hardacre, J. D. Holbrey, S. Johnston, S. E. J. McMath, and M. Nieuwenhuyzen. Small-Angle X-ray Scattering Studies of Liquid Crystalline 1-Alkyl-3-methylimidazolium Salts. *Chem. Mater.*, 14:629–635, 2002.

[14] R. P. Brent. *Algorithms for minimization without derivatives.* Prentice-Hall, 1973.

[15] E. Bychkov, C. J. Benmore, and D. L. Price. Compositional changes of the first sharp diffraction peak in binary selenide glasses. *Phys. Rev. B*, 72:172107, 2005.

[16] L. Cammarata, S. G. Kazarian, P. A. Salter, and T. Welton. Molecular states of water in room temperature ionic liquids. *Phys. Chem. Chem. Phys.*, 3:5192 – 5200, 2001.

[17] J. N. Canongia Lopes and A. A. H. Padua. Molecular force field for ionic liquids iii: Imidazolium, pyridinium, and phosphonium cations; chloride, bromide, and dicyanamide anions. *J. Phys. Chem. B*, 110(39):19586–19592, 2006.

[18] J. N. A. Canongia Lopes and Agilio A. H. Padua. Nanostructural organization in ionic liquids. *J. Phys. Chem. B*, 110(7):3330–3335, 2006.

[19] D.A. Case, T.A. Darden, T.E. Cheatham III, C.L. Simmerling, J. Wang, R.E. Duke, R. Luo, K.M. Merz, D.A. Pearlman, M. Crowley, R.C. Walker, W. Zhang, B. Wang, S. Hayik, A. Roitberg, G. Seabra, K.F. Wong, F. Paesani, X. Wu, S. Brozell, V. Tsui, H. Gohlke, L. Yang, C. Tan, J. Mongan, V. Hornak, G. Cui, P. Beroza, D.H. Mathews, C. Schafmeister, W.S. Ross, and P.A. Kollman. Amber 9. 2006.

[20] E. W. Castner, Jr., J. F. Wishart, and H. Shirota. Intermolecular Dynamics, Interactions, and Solvation in Ionic Liquids. *Acc. Chem. Res.*, 40(11):1217–1227, 2007.

[21] Edward W Castner, Claudio J Margulis, Mark Maroncelli, and James F

Wishart. Ionic liquids: structure and photochemical reactions. *Annu Rev Phys Chem*, 62:85–105, May 2011.

[22] Jr E. W. Castner and J. F. Wishart. Spotlight on ionic liquids. *J. Chem. Phys.*, 132:120901–1–120901–9, 2010.

[23] D. Chakrabarty, A. Chakraborty, D. Seth, P. Hazra, and N. Sarkar. Dynamics of solvation and rotational relaxation of coumarin 153 in 1-butyl-3-methylimidazolium hexafluorophosphate [bmim][pf6]Âwater mixtures. *Chem. Phys. Lett.*, 397:469–474, 2004.

[24] D. Chakrabarty, A. Chakraborty, D. Seth, and N. Sarkar. Effect of water, methanol, and acetonitrile on solvent relaxation and rotational relaxation of coumarin 153 in neat 1-hexyl-3-methylimidazolium hexafluorophosphate. *J. Phys. Chem. A*, 109(9):1764–1769, 2005.

[25] D. Chakrabarty, P. Hazra, A. Chakraborty, D. Seth, and N. Sarkar. Dynamics of solvent relaxation in room temperature ionic liquids. *Chem. Phys. Lett.*, 381:697–704, 2003.

[26] D. Chakrabarty, D. Seth, A. Chakraborty, and N. Sarkar. Dynamics of solvation and rotational relaxation of coumarin 153 in ionic liquid confined nanometer-sized microemulsions. *J. Phys. Chem. B*, 109(12):5753–5758, 2005.

[27] B. Chen and J. I. Siepmann. Microscopic structure and solvation in dry and wet octanol. *J. Phys. Chem. B*, 110(8):3555–3563, 2006.

[28] C. Chiappe. Nanostructural organization of ionic liquids: Theoretical and experimental evidences of the presence of well defined local structures in ionic liquids. *Monatshefte Fur Chemie*, 138(11):1035–1043, 2007.

[29] M. G. Del Popolo and G. A. Voth. On the structure and dynamics of ionic liquids. *J. Phys. Chem. B*, 108:1744–1752, 2004.

[30] A. Demchenko. The red-edge effects: 30 years of exploration. *Luminescence*, 17:19–42, 2002.

[31] R. E. Dinnebier and S. J. L. Billinge, editors. *Powder Diffraction: theory and practice*. Royal Society of Chemistry, Cambridge,UK, 2008.

[32] N. P. Ernsting, M. Asimov, and F. P. SchÂšafer. The electronic origin of the lie* absorptlon of amino coumarins studied in a supersomcally cooled free jet. *Chem. Phys. Lett.*, 91:231, 1982.

[33] K. A. Fletcher and Pandey S. Effect of water on the solvatochromic probe behavior within room-temperature ionic liquid 1-butyl-3-methylimidazolium hexa uorophosphate. *Appl. Spectrosc.*, 56(39):266 Â271, 2002.

[34] N. P. Franks, M. H. Abraham, and W. R. Lieb. Molecular-Organization of Liquid N-Octanol - an X-Ray-Diffraction Analysis. *Journal of Pharmaceutical Sciences*, 82(5):466–470, 1993.

[35] D. Frenkel and B. Smit. *Understanding Molecular Simulation: From Algorithms to Applications*. Academic Press, Inc. Orlando, FL. USA, 2nd edition, 2001.

[36] M. Frisch, G. Trucks, H. Schlegel, G. Scuseria, M. Robb, J. Cheeseman, J. Montgomery, T. Vreven, K. Kudin, J. Burant, J. Millam, S. Iyengar, J. Tomasi, V. Barone, B. Mennucci, M. Cossi, G. Scalmani, N. Rega, G. Petersson, H. Nakatsuji, M. Hada, M. Ehara, K. Toyota, R. Fukuda, J. Hasegawa, M. Ishida, T. Nakajima, Y. Honda, O. Kitao, H. Nakai, M. Klene, X. Li, J. Knox, H. Hratchian, J. Cross, C. Adamo, J. Jaramillo, R. Gomperts, R. Stratmann, O. Yazyev, A. Austin, R. Cammi, C. Pomelli, J. Ochterski, P. Ayala, K. Morokuma, G. Voth, P. Salvador, J. Dannenberg, V. Zakrzewski, S. Dapprich, A. Daniels, M. Strain, O. Farkas, D. Malick, A. Rabuck, K. Raghavachari, J. Foresman, J. Ortiz, Q. Cui, A. Baboul, S. Clifford, J. Cioslowski, B. Stefanov, G. Liu, A. Liashenko, P. Piskorz, I. Komaromi, R. Martin, D. Fox, T. Keith, M. Al-Laham, C. Peng, A. Nanayakkara, M. Challacombe, P. Gill, B. Johnson, W. Chen, M. Wong, C. Gonzalez, and J. Pople. Gaussian 03, revision a.1. *Gaussian, Inc., Pittsburgh PA*, 2003.

[37] D. Fu, X. Sun, J. Pu, and S. Zhao. Effect of water content on the solubility of co2 in the ionic liquid [bmim][pf6]. *J. Chem. Eng. Data*, 51:371, 2006.

[38] K. Fujii, T. Mitsugi, T. Takamuku, T. Yanaguchi, Y. Umebayashi, and S. Ishiguro. Effect of Methylation at the C2 Position of Imidazolium on the Structure of Ionic Liquids Revealed by Large Angle X-ray Scattering Experiments and MD Simulations. *Chem. Lett.*, 38:340–341, 2009.

[39] K. Fujii, S. Seki, S. Fukuda, T. Takamuku, S. Kohara, Y. K., Y. Umebayashi, and S. Ishiguro. Liquid structure and conformation of a low-viscosity ionic liquid, N-methyl-N-propyl-pyrrolidinium bis(fluorosulfonyl) imide studied by high-energy X-ray scattering. *J. Mol. Liq.*, 143:64–69, 2008.

[40] K. Fujii, Y. Soejima, Y.and Kyoshoin, S. Fukuda, R. Kanzaki, Y. Umebayashi, T. Yamaguchi, S. Ishiguro, and T. Takamuku. Liquid Structure of Room-Temperature Ionic Liquid, 1-Ethyl-3-methylimidazolium Bis-(trifluoromethanesulfonyl) Imide. *J. Phys. Chem. B*, 112(14):4329–4336, 2008.

[41] S. Fukuda, M. Takeuchi, K. Fujii, R. Kanzaki, T. Takamuku, K. Chiba, H. Yamamoto, Y. Umebayashi, and S. Ishiguro. Liquid structure of N-butyl-N-methylpyrrolidinium bis(trifluoromethanesulfonyl) amide ionic liquid studied by large angle X-ray scattering and molecular dynamics simulations. *J. Mol. Liq.*, 143:2–7, 2008.

[42] A. M. Funston, T. A. Fadeeva, J. F. Wishart, and E. W. Castner, Jr. Fluorescence Probing of Temperature-Dependent Dynamics and Friction in Ionic Liquid Local Environments. *J. Phys. Chem. B*, 111(18):4963–4977, 2007.

[43] M. C. Gomes, J. N. C. Lopes, and A. A. H. Padua. Thermodynamics and micro heterogeneity of ionic liquids. *Top. Curr. Chem.*, 290:161–183, 2009.

[44] E. Gomez, B. Gonzalez, A. Dominguez, E. Tojo, and J. Tojo. Dynamic viscosities of a series of 1-alkyl-3-methylimidazolium chloride ionic liquids and their binary mixtures with water at several temperatures. *J. Chem. Eng. Data*, 51(2):696–701, 2006.

[45] C. M. Gordon, J. D. Holbrey, A. R. Kennedy, and K. R. Seddon. Ionic liquid crystals: hexafluorophosphate salts. *J. Mater. Chem.*, 8:2627–2636, 1998.

[46] X. Grabuleda, C. Jaime, and P. A. Kollman. Molecular dynamics simulation studies of liquid acetonitrile: New six-site model. *J. Comput. Chem.*, 21(10):901–908, Jan 2000.

[47] F. Hajdu. Tracing the origin of the first sharp diffraction peak (FSDP) of sodium metaphosphate glass and melt. *J. Non-Crystalline Solids*, 277:15–21, 2000.

[48] H. O. Hamaguchi and R. Ozawa. Structure of Ionic Liquids and Ionic Liquid Compounds: Are Ionic Liquids Genuine Liquids in the Conventional Sense? In Stuart A. Rice, editor, *Adv. Chem. Phys., Volume 131*, chapter 3, pages 85–104. John Wiley and Sons, 2005.

[49] C. G. Hanke, N. A. Atamas, and R. M. Lynden-Bell. Solvation of small molecules in imidazolium ionic liquids: a simulation study. *Green Chem.*, 4:107 Â111, 2002.

[50] C. G. Hanke and R. M. Lynden-Bell. A simulation study of water-dialkylimidazolium ionic liquid mixtures. *J. Phys. Chem. B*, 107:10873 Â10878, 2003.

[51] J. P. Hansen and I. R. McDonald. *Theory of simple liquids*, chapter 7, 8, 9. Academic Press, Inc., 3rd edition, 2006.

[52] C. Hardacre, J. D. Holbrey, S. E. J. McMath, D. T. Bowron, and A. K. Soper. Structure Of Molten 1,3-Dimethylimidazolium Chloride Using Neutron Diffraction. *J. Chem. Phys.*, 118(1):273–278, 2003.

[53] C. Hardacre, J. D. Holbrey, C. L. Mullan, M Nieuwenhuyzen, T. G. A. Youngs, and D. T. Bowron. Liquid Structure of the Ionic Liquid, 1-Methyl-4-cyanopyridinium Bis(trifluoromethyl)sulfonylimide Determined from Neutron Scattering and Molecular Dynamics Simulations. *J. Phys. Chem. B*, 112(27):8049–8056, 2008.

[54] C. Hardacre, J. D. Holbrey, C. L. Mullan, T. G. A. Youngs, and D. T. Bowron. Small angle neutron scattering from 1-alkyl-3-methylimidazolium hexafluorophosphate ionic liquids ([cnmim][pf6], n = 4, 6, and 8). *J. Chem. Phys.*, 133:74510–74517, 2010.

[55] C. Hardacre, J. D. Holbrey, M. Nieuwenhuyzen, and T. G. A. Youngs. Structure and Solvation in Ionic Liquids. *Acc. Chem. Res.*, 40(11):1146–1155, 2007.

[56] Berk Hess, Carsten Kutzner, David van der Spoel, and Erik Lindahl. GROMACS 4: Algorithms for highly efficient, load-balanced, and scalable molecular simulation. *J. Chem. Theory Comput.*, 4(3):435–447, 2008.

[57] R. W. Hockney. The potential calculation and some applications. *Methods Comput. Phys.*, 9:136–211, 1970.

[58] J. D. Holbrey, W. M. Reichert, M. Nieuwenhuyzen, S. Johnston, K. R. Seddon, and R. D. Rogers. Crystal polymorphism in 1-butyl-3-methylimidazolium halides: supporting ionic liquid formation by inhibition of crystallization. *Chem. Commun.*, pages 1636–1637, 2003.

[59] J. D. Holbrey and K. R. Seddon. The phase behaviour of 1-alkyl-3-methylimidazolium tetrafluoroborates; ionic liquids and ionic liquid crystals. *J. Chem. Soc., Dalton. Trans.*, pages 2133–2140, 1999.

[60] Z. Hu and C. J. Margulis. Heterogeneity in a room-temperature ionic liquid: Persistent local environments andthe red-edge effect. *Proc. Natl. Acad. Sci. USA*, 103(4):831–836, 2006.

[61] Z. Hu and C. J. Margulis. Room-temperature ionic liquids: Viscosity, slow dynamics and the red edge effect. *Acc. Chem. Res.*, 40(11):1097–1105, 2007.

[62] Z. Hu and C.J. Margulis. A study of the time-resolved fluorescence spectrum and red edge effect of anf in a room-temperature ionic liquid. *J. Phys. Chem. B*, 110(23):11025–11028, 2006.

[63] Z. Hu and C.J. Margulis. On the response of an ionic liquids to external perturbations and the calculation of shear viscosity. *J. Phys. Chem. B*, 111(18):4705–4714, 2007.

[64] J. G. Huddleston, A. E. Visser, W. M. Reichert, H. D. Willauer, G. A. Broker, and R. D. Rogers. Characterization and comparison of hydrophilic and hydrophobic room temperature ionic liquids incorporating the imidazolium cation. *Green Chem.*, 3:156, 2001.

[65] J. K. Hwang and A. Warshel. Microscopic examination of free-energy relationships for electron-transfer in polar-solvents. *J. Am. Chem. Soc.*, 109(3):715–720, Jan 1987.

[66] HyperChem(TM). *Hypercub, Inc.*

[67] S. Jayaraman and E. J. Maginn. Computing The Melting Point And Thermodynamic Stability Of The Orthorhombic And Monoclinic Crystalline Polymorphs Of The Ionic Liquid 1-N-Butyl-3-Methylimidazolium Chloride. *J. Chem. Phys.*, 127(21):214504, 2007.

[68] M. Jergel and P. Mrafko. An X-ray diffraction study of the structural relaxation in the amorphous Ti61Cu16Ni23 and Ti62.5Cu12Ni23Si2.5 alloys. *Journal of Non-Crystalline Solids*, 85(1-2):149 – 161, 1986.

[69] W. Jiang, Y. Wang, and G. A. Voth. Molecular dynamics simulation of nanostructural organization in ionic liquid/water mixtures. *J. Phys. Chem. B*, 111(18):4812–4818, 2007.

[70] H. Jin, X. Li, and M. Maroncelli. Heterogeneous solute dynamics in room temperature ionic liquids. *J. Phys. Chem. B*, 111(48):13473–13478, Jan 2007.

[71] Hui Jin, Xiang Li, and Mark Maroncelli. Heterogeneous solute dynamics in room-temperature ionic liquids. *Journal of Physical Chemistry B*, 114:11370, 2010.

[72] W. L. Jorgensen, D. S. Maxwell, and J. Tirado-Rives. Development and testing of the opls all-atom force field on conformational energetics and properties of organic liquids. *J. Am. Chem. Soc.*, 118(45):11225–11236, 1996.

[73] R. Kanzaki, T. Mitsugi, S. Fukuda, K. Fujii, M. Takeuchi, Y. Soejima, T. Takamuku, T. Yamaguchi, Y. Umebayashi, and S. Ishiguro. Ion-ion interaction in room temperature ionic liquid 1-ethyl-3-methylimidazolium tetrafluoroborate studied by large angle X-ray scattering experiment and molecular dynamics simulations. *J. Mol. Liq.*, 147:77–82, 2009.

[74] R. Karmakar and A. Samanta. Steady-state and time-resolved fluorescence behavior of c153 and prodan in room-temperature ionic liquids. *J. Phys. Chem. A*, 106(28):6670–6675, 2002.

[75] J. Karpiuk. Dual fluorescence from two polar excited states in one molecule. structurally additive photophysics of crystal violet lactone. *J. Phys. Chem. A*, 108(51):11183–11195, Jan 2004.

[76] J Karpiuk, YN Svartsov, and J Nowacki. Photoinduced intramolecular charge transfer to meta position of benzene ring in 6-aminophthalides. *Phys. Chem. Chem. Phys.*, 7:4070–4081, Oct 2005.

[77] D. A. Keen. A comparison of various commonly used correlation functions for describing total scattering. *J Appl Crystallogr*, 34:172–177, Jan 2001.

[78] M. S. Kelkar and E. J. Maginn. Effect of temperature and water content on the shear visocosity of the ionic liquid 1-ethyl-3-methyllimidazolium bis(trifluoromethanesulfony)imide as studied by atomistic simulations. *J. Phys. Chem. B*, 111:4867–4876, 2007.

[79] A. Khara, D. C.and Paul, K. Santhosh, and A. Samanta. Excited state dynamics of 9,9'-bianthryl in room temperature ionic liquids as revealed by picosecond time-resolved fluorescence study. *J. Chem. Sci. (Bangalore, India)*, 121(3):309–315, 2009.

[80] Y. Kimura, M. Fukuda, K. Suda, and M. Terazima. Excited state intramolecular proton transfer reaction of 4â??-N,N-diethylamino-3-hydroxyflavone and solvation dynamics in room temperature ionic liquids studied by optical Kerr gate fluorescence measurement. *J. Phys. Chem. B*, 114:11847, 2010.

[81] G. King and A. Warshel. Investigation of the free-energy functions for electron-transfer reactions. *J. Chem. Phys.*, 93(12):8682–8692, Jan 1990.

[82] T. Koddermann, C. Wertz, A. Heintz, and R. Ludwig. The association of water in ionic liquids: A reliable measure of polarity. *Angew. Chem. Int. Ed.*, 45:3697 Â3702, 2006.

[83] S. Kotni, S. Banerjee, N. Rangaraj, and A. Samanta. Fluorescence response of 4-(N,N'-Dimethylamino)benzonitrile in room temperature ionic liquids: observation of photobleaching under mild excitation condition and multiphoton confocal microscopic study of the fluorescence recovery dynamics. *Journal of Physical Chemistry B*, 114(5):1967–1974, 2010.

[84] P. V. kumar and M. Maroncelli. Polar solvation dynamics of polyatomic solutes:

Simulation studies in acetonitrile and methanol. *J. Chem. Phys.*, 103(8):3038, 1995.

[85] A. S. Larsen, J. D. Holbrey, F. S. Tham, and C. A. Reed. Designing ionic liquids: Imidazolium melts with inert carborane anions. *J. Am. Chem. Soc.*, 122(30):7264–7272, 2000.

[86] E. Lindahl, B. Hess, and D. van der Spoel. Gromacs 3.0: A package for molecular simulation and trajectory analysis. *J. Mol. Mod.*, 7:306–317, 2001.

[87] J. N. C. Lopes, J. Deschamps, and A. A. H. Pádua. Modeling ionic liquids using a systematic all-atom force field. *J. Phys. Chem. B*, 108(6):2038–2047, 2004.

[88] J N C Lopes and A A H Padua. Molecular force field for ionic liquids composed of triflate or bistriflylimide anions. *J. Phys. Chem. B*, 108(43):16893–16898, Jan 2004.

[89] R. M Lynden-Bell. Can marcus theory be applied to redox processes in ionic liquids? a comparative simulation study of dimethylimidazolium liquids and acetonitrile. *J. Phys. Chem. B*, 111(36):10800–10806, Jan 2007.

[90] R. M Lynden-Bell. Does marcus theory apply to redox processes in ionic liquids? a simulation study. *Electrochem. Commun.*, 9(8):1857–1861, Jan 2007.

[91] R. M Lynden-Bell. Redox potentials and screening in ionic liquids: Effects of sizes and shapes of solute ions. *J. Chem. Phys.*, 129(20):204503, Jan 2008.

[92] C. F. Macrae, P. R. Edgington, P. McCabe, E. Pidcock, G. P. Shields, R. Taylor, M. Towler, and Jacco van de Streek. *Mercury*: visualization and analysis of crystal structures. *Journal of Applied Crystallography*, 39(3):453–457, Jun 2006.

[93] P. Mandal, M Sarkar, and A. Samanta. Excitation-wavelength-dependent fluorescence behavior of some dipolar molecules in room-temperature ionic liquids. *J. Phys. Chem. A*, 108(42):9048–9053, 2004.

[94] P. K. Mandal, A. Paul, and A. Samanta. Excitation wavelength dependent fluorescence behavior of the room temperature ionic liquids and dissolved dipolar solutes. *J. Photochem. Photobiol A*, 182:113–120, 2006.

[95] C. J. Margulis. Computational study of imidazolium based ionic solvents with alkyl substituents of different lengths. *Mol. Phys.*, 102(9-10):829–838, 2004.

[96] C. J. Margulis, H. A. Stern, and B. J. Berne. Computer simulation of a "green

chemistry" room-temperature ionic solvent. *J. Phys. Chem. B*, 106(46):12017–12021, 2002.

[97] Q. Mei, C. J. Benmore, S. Sen, R. Sharma, and J. L. Yarger. Intermediate range order in vitreous silica from a partial structure factor analysis. *Phys. Rev. B*, 78:144204, 2008.

[98] S. R. Mente and M. Maroncelli. Computer simulations of the solvatochromism of betaine-30. *J. Phys. Chem. B*, 103(36):7704–7719, 1999.

[99] A. A. H. Pádua, Margarida F. C. Gomes, and J. N. A. C. Lopes. Molecular Solutes in Ionic Liquids: A Structural Perspective. *Acc. Chem. Res.*, 40(11):1087–1096, 2007.

[100] A. Paul, P. K. Mandal, and A. Samanta. On the optical properties of imidazolim ionic liquids. *J. Phys. Chem. B*, 109(18):9148–9153, 2005.

[101] T. Pott and P. Méléard. New insight into the nanostructure of ionic liquids: a small angle X-ray scattering (SAXS) study on liquid tri-alkyl-methyl-ammonium bis(trifluoromethanesulfonyl)amides and their mixtures. *Phys. Chem. Chem. Phys.*, 11(26):5469–5475, 2009.

[102] D. Potter. *Computational Physics*. Wiley, Inc. New York, 1973.

[103] David Long Price. Intermediate-range order in glasses. *Current Opinion in Solid State and Materials Science*, 1(4):572 – 577, 1996.

[104] E. Prince, editor. *International Tables for Crystallography*, volume C. International Union of Crystallography, 2006.

[105] X. Qui, J. W. Thompson, and S. J. L. Billinge. PDFgetX2: a GUI-driven program to obtain the pair distribution function from X-ray powder diffraction data. *J. Appl. Cryst.*, 37:678, 2004.

[106] J. J. M. Ramos, C. A. M. Afonso, and L. C. Branco. Glass transition relaxation and fragility in two room temperature ionic liquids. *J. Therm. Anal. Calorim.*, 71(2):659–666, 2003.

[107] L. P. N. Rebelo, V. Najdanovic-Visak, Z. P. Visak, M. Nunes da Ponte, J. Szydlowski, J. Troncoso C. A. Cerdeiria, L. Roman, J. M. S. S. Esperana, H. J. R. Guedes, and H. J. R. de Sousa. A detailed thermodynamic analysis of [c4mim][bf4] + water as a case study to model ionic liquid aqueous solutions. *Green Chem.*, 6:369, 2004.

[108] J. Ridley and M. Zerner. An intermediate neglect of differential overlap technique for spectroscopy: Pyrrole and the azines. *Theor. Chim. Acta*, 32:111–134, 1973.

[109] Olga Russina, Alessandro Triolo, Lorenzo Gontrani, Ruggero Caminiti, Dong Xiao, Larry G. Hines, Jr., Richard A. Bartsch, Edward L. Quitevis, Natalia Pleckhova, and Kenneth R. Seddon. Morphology and intermolecular dynamics of 1-alkyl-3-methylimidazolium bis(trifluoromethane)sulfonylamide ionic liquids: structural and dynamic evidence of nanoscale segregation. *J. Phys.: Condens. Matter*, 21(42):424121, 2009.

[110] S. Saha and H. Hamaguchi. Effect of water on the molecular structure and arrangement of nitrile-functionalized ionic liquids. *J. Phys. Chem. B*, 110:2777 Â 2781, 2006.

[111] Kalyanasis Sahu, Sean J Kern, and Mark A Berg. Heterogeneous reaction rates in an ionic liquid: Quantitative results from two-dimensional multiple population-period transient spectroscopy. *J Phys Chem A*, Jun 2011.

[112] A. Samanta. Dynamic stokes shift and excitation wavelength dependent fluorescence of dipolar molecules in room temperature ionic liquids. *J. Phys. Chem. B*, 110(28):13704–13716, 2006.

[113] K. Santhosh and A. Sanamta. Modulation of the excited state intramolecular electron transfer reaction and dual fluorescence of crystal violet lactone in room temperature ionic liquids. *J. Phys. Chem. B.*, 114(28), 2010.

[114] N. Sarkar. private communication.

[115] C. Schroeder, T. Rudas, G. Neumayr, W. Gansterer, and O. Steinhauser. Impact Of Anisotropy On The Structure And Dynamics Of Ionic Liquids: A Computational Study Of 1-Butyl-3-Methyl-Imidazolium Trifluoroacetate. *J. Chem. Phys.*, 127(4):44505, 2007.

[116] C. Schroeder, T. Rudas, and O. Steinhauser. Simulation Studies Of Ionic Liquids: Orientational Correlations And Static Dielectric Properties. *J. Chem. Phys.*, 125(24):244506, 2006.

[117] C. Schroeder and O. Steinhauser. The Influence Of Electrostatic Forces On The Structure And Dynamics Of Molecular Ionic Liquids. *J. Chem. Phys.*, 128(22):224503, 2008.

[118] K. R. Seddon, A. Stark, and M. Torres. Influence of chloride, water, and or-

ganic solvents on the physical properties of ionic liquids. *Pure Appl. Chem.*, 72(12):2275–2287, 2000.

[119] Y Shim, MY Choi, and HJ Kim. A Molecular Dynamics Computer Simulation Study Of Room-Temperature Ionic Liquids. I. Equilibrium Solvation Structure And Free Energetics. *J. Chem. Phys.*, 122(4):44510, 2005.

[120] Y. Shim, D. Jeong, S. Manjari, M. Y. Choi, and H. J. Kim. Solvation, solute rotation and vibration relaxation, and electron-transfer reactions in room-temperature ionic liquids. *Acc. Chem. Res.*, 40(11):1130–1137, Mar 2007.

[121] Youngseon Shim and Hyung J Kim. Free energy and dynamics of electron-transfer reactions in a room temperature ionic liquid. *J. Phys. Chem. B*, 111(17):4510–4519, Jan 2007.

[122] S. Soyer Uzun, S. Sen, C. J. Benmore, and B. G. Aitken. A combined neutron and x-ray diffarction study of short- and intermediate-range structural characteristics of ge-as sulfide glasses. *J. Phys.: Condens. Matter*, 20:335105, 2008.

[123] Ian Streeter, R. M Lynden-Bell, and Richard G Compton. Nonlinear relaxation in redox processes in ionic and polar liquids. *J. Phys. Chem. C*, 112(37):14538–14544, Jan 2008.

[124] M Tachiya. Relation between the electron-transfer rate and the free energy change of reaction. *J. Phys. Chem.*, 93:7050–7052, 1989.

[125] M Tachiya. Generalization of the marcus equation for the electron-transfer rate. *J. Phys. Chem.*, 97(22):5911–5916, Jan 1993.

[126] H. Tokuda, K. Hayamizu, K. Ishii, M. A. B. H. Susan, and M. Watanabe. Physicochemical properties and structures of room temperature ionic liquids. 2. variation of alkyl chain length in imidazolium cation. *J. Phys. Chem. B*, 109(13):6103–6110, 2005.

[127] M. P. Tosi, D. L. Price, and M. L. Saboungi. Ordering in metal halide melts. *Annu. Rev. Phys. Chem.*, 44:173–211, 1993.

[128] C. D. Tran, S. H. De Paoli Lacerda, and D. Oliveira. Absorption of water by room-temperature ionic liquids: Effect of anions on concentration and state of water. *Appl. Spectrosc.*, 57(2):152–157, 2003.

[129] A. Triolo, O. Russina, H. Bleif, and E. Di Cola. Nanoscale Segregation in Room Temperature Ionic Liquids? *J. Phys. Chem. B*, 111(18):4641–4644, 2007.

[130] A. Triolo, O. Russina, B. Fazio, R. Triolo, and E. DiCola. Morphology of 1-alkyl-3-methylimidazolium hexafluorophosphate room temperature ionic liquids. *Chem. Phys. Lett.*, 457:362–365, 2008.

[131] Sergio M. Urahata and Mauro C.C. Ribeiro. Structure of ionic liquids of 1-alkyl-3-methylimidazolium cations: A systematic computer simulation study. *J. Chem. Phys.*, 120(4):1855 – 1863, 2004.

[132] K. S. Vahvaselka, R. Serimaa, and M. Torkkeli. Determination of Liquid Structures of the Primary Alcohols Methanol, Ethanol, 1-Propanol, 1-Butanol and 1-Octanol by X-Ray-Scattering. *Journal of Applied Crystallography*, 28:189–195, 1995.

[133] D. van der Spoel, E. Lindahl, B. Hess, G. Groenhof, A. E. Mark, and H. J. C. Berendsen. GROMACS: Fast, flexible, and free. *J. Comput. Chem.*, 26(16):1701–1718, 2005.

[134] D. van der Spoel, E. Lindahl, B. Hess, A. van Buuren, E. Apol, P. Meulenhoff, D. Tieleman, A. Sijbers, K. Feenstra, van Drunen R., and Berendsen H. *Gromacs User Manual version 3.2*. www.gromacs.org, 2004.

[135] P. Walden. Molecular weights and electrical conductivity of several fused salts. *Bull. Acad. Imper. Sci. (St. Petersburg)*, page 1800, 1914.

[136] Y. Wang, W. Jiang, T. Yan, and G. A. Voth. Understanding Ionic Liquids through Atomistic and Coarse-Grained Molecular Dynamics Simulations. *Acc. Chem. Res.*, 40(11):1193–1199, 2007.

[137] Y. Wang, H. R. Li, and S. J. Han. Structure And Conformation Properties Of 1-Alkyl-3-Methylimidazolium Halide Ionic Liquids: A Density-Functional Theory Study. *J. Chem. Phys.*, 123(17), 2005.

[138] Y. Wang, H. R. Li, and S. J. Han. The Chemical Nature Of The C-Circle Plus-H Center Dot Center Dot Center Dot X- (X=Cl Or Br) Interaction In Imidazolium Halide Ionic Liquids. *J. Chem. Phys.*, 124(4), 2006.

[139] A Warshel. Dynamics of reactions in polar-solvents - semi-classical trajectory studies of electron-transfer and proton-transfer reactions. *J. Phys. Chem.*, 86(12):2218–2224, Jan 1982.

[140] A Warshel. *Computer modeling of chemical reactions in enzymes and solutions*. John Wiley and Sons, NewYork, 1991.

[141] J. K. Wilkes. Properties of ionic liquid solvents for catalysis. *J. Mol. Catal. A: Chem.*, 214:11–17, 2004.

[142] J. S. Wilkes. Ionic liquids in perspective: The past with an eye toward the industrial future. In R. D. Rogers and K. R. Seddon, editors, *Ionic liquids–Industrial applications for green chemistry*, volume 818, pages 214–229. American Chemical Society, Washington, DC, 2002.

[143] John S. Wilkes and Michael J. Zaworotko. Air and water stable 1-ethyl-3-methylimidazolium based ionic liquids. *J. Chem. Soc., Chem. Common.*, 13(13):965–7, 1992.

[144] M. Wilson and P. A. Madden. "Prepeaks" and "first sharp diffraction peaks" in computer simulations of strong and fragile ionic liquids. *Phys. Rev. Lett.*, 72(19):3033–3036, 1994.

[145] J Wishart. Importance of ionic liquid solvation dynamics to their applications in advanced devices and systems. *The Journal of Physical Chemistry Letters*, 1(10):1629–1630, 2010.

[146] D. Xiao, J. R. Rajian, S. F. Li, R. A. Bartsch, and E. L. Quitevis. Additivity in the optical Kerr effect spectra of binary ionic liquid mixtures: Implications for nanostructural organization. *J. Phys. Chem. B*, 110:16174–16178, 2006.